

MODELING THE AEROSOLS IN THE ATMOSPHERE OF TITAN

By

JOANNA ELIZABETH THOMAS-OSIP

A DISSERTATION PRESENTED TO THE GRADUATE SCHOOL
OF THE UNIVERSITY OF FLORIDA IN PARTIAL FULFILLMENT
OF THE REQUIREMENTS FOR THE DEGREE OF
DOCTOR OF PHILOSOPHY

UNIVERSITY OF FLORIDA

2001

This is dedicated to all those who encouraged and supported me throughout the lengthy ordeal of graduate school and to those who come after me and have need of the same. Remember Henry Ford's words "Obstacles are those frightful things you see when you take your eyes off your goal."

ACKNOWLEDGMENTS

First and foremost I would like to thank my husband, David Osip, for knowing what I needed, be it quiet support or some combination of nagging and bribing. He believed in me when I had stopped. He has been a great resource when I let him help me and he provides daily inspiration as he strives to be the best astronomer he can be and achieves that with flying colors.

Secondly, I thank my advisor, Bo Gustafson, for allowing me the time and space to figure things out on my own. I would also like to thank all my committee members for their input. I would especially like to thank Ludmilla Kolokolova who was always willing to discuss my work and made many helpful comments and suggestions. She was also often ready with an encouraging word when I came to her for advice. I would also like to thank Yu-Lin Xu for many helpful discussions regarding theoretical light scattering and radiative transfer. In addition, he provided me with very useful calculations from his code for light scattering by aggregates of spheres.

I would also like to thank all my parents for encouraging me to pursue my dreams each in his or her own way. My father, John R. Thomas, has gone back to graduate school and made it a race to see who could get a Ph.D. first. My step-father kept me laughing. My mother loved me and reminded me of this by telling me, "You know Joanna, it doesn't have to be perfect."

Furthermore, I want to thank all my friends for their love and support. Fellow graduate student, Joanna Levine allowed me to stay with her and acted as my chauffeur during my visits back to Gainesville after we had moved away. She always made returning to Gainesville fun and helped improve my confidence by telling me I inspired her. Kirk, Nicole, and Anthony Becker invited me into their home, sometimes unannounced, and provided me an escape from the university when I needed it. Tim Spahr listened to me vent too many times to count and shared many a trip to Beezer's when I needed fries. Fellow graduate student, research group member, and previous office mate, Thomas Waldemarsson asked good questions and showed genuine interest in my work.

Lastly I would like to thank Jim Elliot for becoming my surrogate mentor after we moved to Boston. He provided me with some good advice and the necessary encouragement (in the way of employment) for finishing this dissertation, as well as some space to work and access to a fast computer on which to run my models.

TABLE OF CONTENTS

	page
ACKNOWLEDGMENTS	iii
TABLE OF CONTENTS.....	v
LIST OF TABLES	vii
LIST OF FIGURES	viii
ABSTRACT.....	xii
INTRODUCTION.....	1
Spherical Particle Paradox	5
How Can Analog Light Scattering Help?	9
SINGLE SCATTERING PROPERTIES OF MODELS	13
Electromagnetic Radiation and Polarization.....	13
Stokes Vectors.....	17
Scattering by a Single Particle and a Cloud of Particles.....	18
Scattering Matrix	18
Scattering, Absorption, and Extinction Cross-Sections and Efficiencies	23
Scattering Calculations	25
Rayleigh Scattering.....	25
Mie Theory – Spheres.....	26
Exact Multisphere Scattering Theory	27
Discrete Dipole Approximation.....	27
Effective Medium Theory	28
Laboratory Models and the Rationale Behind Them.....	29
Cubes.....	29
Aggregates.....	31
Single Scattering Measurements	39
Procedures	39
Data Reduction	41
Averaging over orientation.....	41
Calibration	43
Scattering matrix as a function of scattering angle.	44
Color and polarimetric color.....	46
Porosity.....	48
Single Scattering Results from the Laboratory and Theory	49

Scattering Matrices for Cubes	52
Scattering Matrices for Aggregates	56
Single Scattering and Titan	68
POLARIZED RADIATIVE TRANSFER MODELING	76
Basic Definitions and Radiometric Quantities	77
A Model Appropriate for Titan	80
The Vector Transfer Equation	81
The Phase Matrix	83
Fourier Series Analysis in Azimuth Angle	85
Expansion of the scattering matrix.....	87
Doubling and Adding Method.....	88
Reflection and Transmission Matrices.....	89
Initialization.....	94
Reflection From A Surface At The Bottom Of The Atmosphere.....	96
Implementation.....	96
Integration Over a Planetary Disk	98
Testing and Sensitivity Studies	106
Testing Rt3	106
Testing Disk Integration.....	111
Parameter Sensitivity Tests	114
Surface and Semi-Infinite Atmosphere Tests.....	117
Size Distribution Test.....	119
MODEL CALCULATIONS OF TITAN'S ATMOSPHERE	122
Overview of Entire Modeling Procedure	122
Observations.....	124
Single Layer Model Results	126
More Complicated Models.....	144
Possible Applications to Cassini	154
Conclusions	156
Future Work	159
Single Scattering Issues.....	160
Other Types of Models to Consider.....	161
APPENDIX A RADIUS OF GYRATION	162
APPENDIX B EXPANSION OF THE SCATTERING MATRIX	165
Comparison of Legendre Polynomials to Laboratory Data	165
Comparison of Legendre Polynomials to Smoothed Laboratory Data.....	172
APPENDIX C INCLUSION OF THE FULL SCATTERING MATRIX IN RADIATIVE TRANSFER CALCULATIONS	180
LIST OF REFERENCES	183
BIOGRAPHICAL SKETCH	191

LIST OF TABLES

Table	page
1.1 Indices of refraction for Tholin and Tholin ice	8
2.1 Physical characteristics of cube targets.....	30
2.2 Physical characteristics of aggregate targets.....	32
2.3 Multi-sphere aggregate characteristics	38
2.4 List of microwave analog laboratory measurements.	40
2.5 Summary of some single scattering results.	50
2.6 Photopolarimetry best fit H-G function parameters	69
2.7 R_{ss} values for all targets.	74
4.1 Single scattering albedo estimates for all the laboratory targets.....	124
4.2 Observed Geometric albedo of Titan at the photopolarimetry wavelengths.....	125
4.3 Geometric albedos computed for single layer model atmospheres.	132
4.4 Geometric albedos for computed dual layer model atmospheres.....	145
4.5 Geometric albedos for selected single layer combination models.	147
4.6 Summary of selected model results and Titan's observed characteristics.....	157

LIST OF FIGURES

Figure	page
1.1 Pioneer 11 and Voyager 2 polarimetry as a function of phase angle.	6
1.2 Diagram of microwave analog laboratory facility at the University of Florida.	10
2.1 Propagation of an electromagnetic wave and depiction of linear polarization.	15
2.2 The polarization ellipse.	16
2.3 Reciprocal orientation.	21
2.4 Mirror and mirror reciprocal orientations.	23
2.5 Photograph of the four acrylic cubes.	31
2.6 Photograph of the LSA on a Styrofoam support.	33
2.7 Photograph of the BSA on a Styrofoam support.	34
2.8 Photograph of the CYA on a Styrofoam support.	35
2.9 Photograph of the OA.	36
2.10 Photograph of the SA.	37
2.11 Photograph of the CA.	37
2.12 Representation of X1-4 aggregate.	38
2.13 Designation of orientations for a cube.	42
2.14 Single orientation intensity measurements for four different size cubes.	43
2.15 Surface plot of intensity as a function of scattering angle and frequency.	45
2.16 Surface plot of polarization as a function of scattering angle and frequency.	46
2.17 Angular distribution of the F-matrix elements for the 1.5" cube.	54
2.18 Angular distribution of the F-matrix elements for the 0.5" cube.	55
2.19 DDA calculations and microwave laboratory data for 0.5" cube.	56
2.20 Angular distribution of the F-matrix elements for the LSA.	60
2.21 Angular distribution of the F-matrix elements for the CYA.	61
2.22 Angular distribution of the F-matrix elements for the BSA.	62
2.23 Angular distribution of the F-matrix elements for the SA.	63
2.24 Angular distribution of the F-matrix elements for the OA.	64
2.25 Angular distribution of the F-matrix elements for the CA.	65
2.26 Angular distribution of the F-matrix elements for aggregates X1-X4.	66
2.27 Angular distribution of the F-matrix elements for the X1-X4 constituents.	67
2.28 Synthetic phase function and polarization fitting Titan photopolarimetry.	71
4.1 Flow chart of entire modeling process.	123
4.2 0.5" cube model compared to Pioneer 11 and Voyager 2 photopolarimetry.	133
4.3 1.5" cube model compared to Pioneer 11 and Voyager 2 photopolarimetry.	134
4.4 OA model compared to Pioneer 11 and Voyager 2 photopolarimetry.	135
4.5 CYA model compared to Pioneer 11 and Voyager 2 photopolarimetry.	136
4.6 SA model compared to Pioneer 11 and Voyager 2 photopolarimetry.	137
4.7 CA model compared to Pioneer 11 and Voyager 2 photopolarimetry.	138

4.8 LSA model compared to Pioneer 11 and Voyager 2 photopolarimetry.	139
4.9 LSA blue model compared to Pioneer 11 and Voyager 2 photopolarimetry.	140
4.10 LSA red model compared to Pioneer 11 and Voyager 2 photopolarimetry.	141
4.11 X1-X4 models compared to Pioneer 11 and Voyager 2 photopolarimetry.	142
4.12 Single constituent spheres from the X1-X4 aggregates and photopolarimetry.	143
4.13 LSA and X2 combination model compared to photopolarimetry.	149
4.14 Another LSA and X2 combination model compared to photopolarimetry.	150
4.15 Single layer combination of LSA red and X3 compared to photopolarimetry.	151
4.16 Single layer combination of LSA blue and X2 compared to photopolarimetry.	152
4.17 Best fit model atmosphere containing 60% X2/3 constituents and 40% LSA.	153
4.18 DISR prediction based on 60/40 combination model at 500 nm.	155
B.1 Scattering matrix elements for the CYA and the Legendre Series fits.	166
B.2 Scattering matrix elements for the LSA and the Legendre Series fits.	167
B.3 Scattering matrix elements for the CA and the Legendre Series fits.	168
B.4 Scattering matrix elements for the X1 and the Legendre Series fits.	169
B.5 Scattering matrix elements for the 60/40 mix of X2 constituents and LSA blue and the Legendre Series fits.	170
B.6 Scattering matrix elements for the 60/40 mix of X3 constituents and LSA red and the Legendre Series fits.	171
B.7 Example of Legendre series fit for the unsmoothed LSA data in blue waveband.	173
B.8 Scattering matrix elements for the smoothed LSA data in blue waveband.	174
B.9 Scattering matrix elements for the smoothed LSA data in red waveband.	175
B.10 Scattering matrix elements for the smoothed 0.5" cube data.	176
B.11 Scattering matrix elements for the smoothed 1.5" cube data.	177
B.12 Scattering matrix elements for the smoothed OA data.	178
B.13 Scattering matrix elements for the smoothed SA data.	179

Abstract of Dissertation Presented to the Graduate School
of the University of Florida in Partial Fulfillment of the
Requirements for the Degree of Doctor of Philosophy

MODELING THE AEROSOLS IN THE ATMOSPHERE OF TITAN

By

Joanna Elizabeth Thomas-Osip

May 2001

Chairman: Bo Å. S. Gustafson
Major Department: Astronomy

A combination of laboratory experiments, theoretical modeling, and spacecraft *in situ* observations is employed to characterize the aerosols in the atmosphere of Titan. The scattering properties of model aerosols were measured using the Microwave Analog Light Scattering Facility at the University of Florida and complemented with theoretical modeling of single scattering characteristics and radiative transfer in Titan's atmosphere. This study compares these modeling results with photopolarimetric observations made over a range of phase angles by the Pioneer 11 and Voyagers 1 and 2 spacecraft approximately 20 years ago.

Important results of this work include a survey of the scattering properties of different particle shapes necessary to accurately interpret these observations without introducing non-physical assumptions about the particles or requiring additional free parameters to the radiative transfer models. Previous studies use calculation methods

which, due to computing memory and processing time requirements, *a priori* exclude much of the phase space that the microwave analog laboratory is ideal for exploring. The goal of the present work, to directly constrain aerosol physical characteristics, is addressed by studying in a consistent manner how a variety of particle morphologies affect polarization and intensity measurements of Titan's atmosphere.

Single liquid drops are modeled using spheres for which scattering patterns can be easily calculated with Mie theory. Cubes are used as a representation of solids with sharp edges due to fragmentation. More complex particle morphologies are modeled as aggregates that are likely formed by collisions between semi-liquid spheres that stick together instead of merging. Radiative transfer calculations for model atmospheres containing these particles are constrained by direct comparison to *in situ* spacecraft observations. Based on these comparisons, many model morphologies are excluded from further consideration and the most plausible physical particle models suggest a combination of Rayleigh-like monomer particles and aggregates that are larger than those previously investigated provide the best fit to the existing data. Additional laboratory experiments and more refined modeling awaits the results of a new rich observational dataset following the Cassini/Huygens encounter with Titan in 2004.

CHAPTER 1 INTRODUCTION

Titan, the second largest planetary satellite and the only planetary satellite to possess a significant atmosphere, was discovered by Huygens in 1655. Its atmosphere, however, was not detected until 1944 when Kuiper (1944) first observed the methane bands between 0.6 and 1 μm . From these observations the methane pressure was initially estimated to be low and the atmosphere quite tenuous and therefore interest waned until the early 1970's. Further atmospheric studies were prompted when Titan's visual spectrum was found to be similar to Saturn's equatorial belt (McCord *et al.* 1971).

A controversy between a greenhouse model and a temperature inversion model for the thermal structure of Titan's atmosphere raged throughout the rest of Titan's pre-Voyager history. The brightness temperature was measured to be 125K at 10-14 μm (Allen and Murdock 1971) which is significantly higher than the solar equilibrium temperature of 83K for a blackbody radiator at Titan's distance from the Sun. Thus, they hypothesized that a greenhouse effect might be responsible. The creation of a greenhouse effect depends on the presence of materials which absorb in the infrared where the thermal emission from the surface and/or the lower atmosphere is large. Near-infrared and visible spectroscopy (Trafton 1972b; Trafton 1972a) were used to detect a much higher abundance of CH_4 than previously determined by Kuiper and to make a tentative detection of H_2 . These data set the stage for various greenhouse models utilizing

quadrupole and collision induced dipole transitions in H_2 (Sagan 1973) and octopole transitions in CH_4 and collision induced transitions in H_2 and CH_4 (Pollack 1973) as infrared absorbers.

Titan, however, has a low albedo (<0.05) in the ultraviolet (McCord *et al.* 1971; Noland *et al.* 1974). No plausible gases in a cold reducing atmosphere absorb strongly in the UV. Therefore, Khare and Sagan (1973) suggested that logical choices for materials with high UV absorption are solids produced by photochemical and charged particle synthesis in a reducing atmosphere which they termed "tholins." This led to inversion models (Danielson *et al.* 1973) where high altitude haze (instead of greenhouse gas) is responsible for high brightness temperatures. Thermal inversion in this case is similar to that caused by O_3 in the Earth's atmosphere. Small haze particles ($\approx 0.1 \mu\text{m}$) are poor radiators and thus they must lose the energy they absorb from the solar radiation by collisional heating of the gas.

With data from the Pioneer 11 and Voyager 1 and 2 spacecraft missions that observed Titan during the years 1979-1981, it was determined that a combination of both a greenhouse effect and thermal inversion exists with a surface pressure of 1.5 bar at a temperature of 94 K, a tropopause at a temperature of 74 K, and a stratospheric temperature which approaches 174 K as the pressure approaches zero (Lindal *et al.* 1983). But the exact nature of the coupling of the greenhouse effect and the thermal inversion process is unsettled. For example, the existence of CH_4 clouds in the troposphere is still being debated (McKay *et al.* 1989; Toon *et al.* 1992; Griffith *et al.* 1998). The thermal inversion has also been called an anti-greenhouse effect (McKay *et al.* 1991) because as the upper atmosphere becomes more absorbing (due to haze), and

thus warmer itself, the lower atmosphere and surface become cooler due to the reduced energy input as well as the thermal energy that escapes due the transparent nature of the haze in the infrared.. The nature of the aerosol properties is thus a key component to understanding the thermal structure of Titan's atmosphere.

Aerosol properties are also important to predicting the penetration of sunlight into the atmosphere and thus discerning where there may be windows through the haze to view the surface. For example, albedo variations with a period corresponding to Titan's orbital period in near-infrared methane windows have been attributed to surface variations (Griffith 1993; Lemmon *et al.* 1993; Coustenis *et al.* 1995; Lemmon *et al.* 1995). Near infrared imaging (by HST as well as ground-based systems with adaptive optics) in methane windows between 0.9 μm and 2.1 μm are also able to discern surface albedo features (Smith *et al.* 1996; Combes *et al.* 1997; Gibbard *et al.* 1999). Furthermore, near-infrared spectroscopic monitoring has demonstrated transient albedo variations thought to be caused by thin and/or patchy methane clouds in the troposphere (Griffith *et al.* 1998).

Understanding the 10% seasonal variation in Titan's geometric albedo (Lockwood *et al.* 1986) and 25% North-South brightness asymmetry (Sromovsky *et al.* 1981), the orientation of which is also seasonally variable (Caldwell *et al.* 1992), is linked to better characterizing Titan's aerosol properties. Possible explanations for the above observations include time varying aerosol production due to variations in incident solar radiation, time varying indices of refraction due to compositional changes in the gases from which the aerosols are formed, and redistribution of the aerosols as a function of time due to atmospheric circulation (Hutzell *et al.* 1996). In differentiating between

these cases, it is necessary to begin with an appropriate conception of the aerosol properties. The modeling effort in this work is static in nature and therefore temporal and spatial dependencies will not be further discussed. They are mentioned here only in a motivational context.

Until Cassini and its probe, Huygens, arrive at the Saturnian system in 2004, the most useful observational data available to provide information about the aerosols in the atmosphere of Titan are the photopolarimetry and imaging data from the Voyager and Pioneer spacecraft. While there has been a great improvement of the quality of Earth-based observations (HST observations can be included here as well) the single most important feature of the observations obtained via spacecraft are the range of phase angles that allow examination of the angular distribution of light scattered by the atmospheric aerosols. Measurements of the brightness and linear polarization of the integrated disk were obtained by the IPP (imaging photopolarimeter) aboard Pioneer 11 during its encounter with the Saturnian system in September of 1979 (Tomasko and Smith 1982). These observations were performed at a range of phase angles between 21° and 96° using two filters with effective wavelengths of 452 nm and 648 nm. The same type of measurements were also obtained by the Voyager 2 PPS (photopolarimeter experiment) during its flyby in August of 1981 (West *et al.* 1983) except at a larger range of phase angles ($3\text{--}154^\circ$) and different wavelengths (264 nm and 750 nm). High-phase angle ($129\text{--}160^\circ$) images were obtained by both Voyager 1 (in November of 1980) and Voyager 2 using the so-called violet (~ 420 nm) and green (560 nm) filters (Rages *et al.* 1983).

The first interpretations of these data were based on models including only spherical aerosols. This was not only the easiest place to start, but until recently, it was the only practical option because calculation of the scattering from other types of particles was both inexact and computationally expensive to impossible.

Spherical Particle Paradox

Estimation of particle properties from polarization versus phase angle (Tomasko and Smith 1982; West *et al.* 1983) suggests that in order to fit the data with spheres, small particles are needed with radii of approximately $0.1\text{ }\mu\text{m}$ (where the actual radii is a function of optical depth). These polarization data are shown in Figure 1.1. The polarization curves at all four wavelengths are characterized by positive polarization peaking between 40% and 60% near a phase angle of 90° . The suggestion that the particles are small is logical based on the fact that these curves are reminiscent of the polarization from very small particles (termed Rayleigh particles) with its peak at 90° . Rayleigh particles, however, show 100% polarization at their peak. One would expect, however, that due to multiple scattering in the atmosphere that an atmosphere of Rayleigh particles would produce less than 100% polarization.

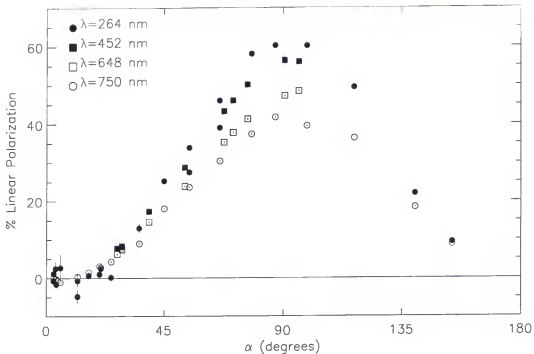


Figure 1.1 Pioneer 11 and Voyager 2 polarimetry as a function of phase angle. Where no error bars are shown, the error is smaller than the symbols (Tomasko and Smith 1982; West *et al.* 1983).

High phase angle images from Voyager 1 and 2 (Rages *et al.* 1983), however, suggest that for spherical particles, larger sizes (with radii of approximately $0.25 \mu\text{m}$) are necessary to produce the steep slope of the forward scattered intensity due to the fact that the diffraction peak gets narrower as particles get larger. Diffraction is not strongly dependent on index of refraction or shape but rather overall size is the determining factor here.

The conclusion drawn from these two pieces of evidence (the polarization and the forward scattering) is that the aerosols must be non-spherical. In 1988 a non-spherical aggregate model was first proposed by Bar-Nun *et al.* (1988) based on photochemical simulations of aerosol production in the atmosphere of Titan. This has since become a

working model for Titan's aerosols (West and Smith 1991; Cabane *et al.* 1993; Lemmon 1994; Rannou *et al.* 1995; Rannou *et al.* 1997).

The observational data available (Pioneer 11, Voyager 1 and 2, and ground based geometric albedo) are not consistently matched using a single particle model. West and Smith (1991) fit the observed polarization by calculating the scattering from an aggregate of eight so-called "monomers" with a radii of 0.06 μm and a real refractive index based on tholins produced in a laboratory simulation of Titan's atmosphere (Khare *et al.* 1984) using a discrete dipole approximation code. The imaginary part of the refractive index is used as a free parameter (a non-physical simplification) and is determined by fitting the geometric albedo. They must also add a second mode of Rayleigh scatterers at small wavelengths to increase the model polarization and make the atmosphere optically thin so that an unspecified surface acts in a depolarizing nature at long wavelengths.

See Table 1.1 for a list of the refractive indices applicable for the Pioneer and Voyager photopolarimeter data. Rannou *et al.* (1995) fit geometric albedo (the fraction of incident light reflected from a planetary object) but they also use the imaginary index of refraction as a free parameter by multiplying the tholin imaginary index by a parameterized constant. The Kramer-Kronig relation below illustrates that the real and imaginary parts of the index of refraction (and thus dielectric function) are dependent on each other and frequency (Reitz *et al.* 1980; Bohren and Huffman 1983).

$$\epsilon'(\omega) = 1 + \frac{2}{\pi} \int_0^{\infty} \frac{\omega' \epsilon''(\omega')}{\omega'^2 - \omega^2} d\omega' \quad (1.1)$$

The frequency is denoted ω , and ϵ' and ϵ'' are the real and imaginary parts of the dielectric function. From this equation we can see the real part at one frequency is

dependent on the imaginary part at all frequencies and vice versa and thus using either part as a free parameter is unphysical. Also, keep in mind that the geometric albedo can be fit very well with spherical aerosols (Toon *et al.* 1992) and so it is not necessarily the best indicator for particle shape.

Table 1.1 Indices of refraction for Tholin and Tholin ice.

Wavelength (nm)	Index for Tholin	Index for Tholin Ice
264	1.68-0.18i	1.63-0.059i
452	1.72-0.057i	1.56-0.0023i
648	1.68-0.013i	1.54-0.0013i
750	1.67-0.0067i	1.54-0.00073i

Note: Wavelengths are those at which photopolarimetry observations were made with the Pioneer 11 and Voyager 2 spacecraft. The indices for tholin were measured by Khare *et al.* (1984). The indices for tholin ice were measured by Khare *et al.* (1993). The indices for the highest three wavelengths have been interpolated from these measurements.

The first study to try to fit the intensity phase function, the polarization, and the geometric albedo (Lemmon 1994) used a model based on West and Smith (1991). Lemmon also used the imaginary index of refraction as an independent parameter and required a combination of particle populations and a surface to fit the observations. In the most recent work on the subject of an aggregate model for Titan's aerosols radial intensity scans from the Voyager 2 high phase angle images were fit using an aggregate of spheres with radii of 0.066 μm (Rannou *et al.* 1997). This fit was obtained by calculating the extinction of an aggregate using a method which the authors developed and call the mean-field approximation of Mie scattering by fractal aggregates of identical spheres (Botet *et al.* 1997).

How Can Analog Light Scattering Help?

Exact solutions and approximations for the scattering from irregular particles can only be used for small particles due to computing time and RAM needed for matrix inversions. So directly measuring the scattering from irregular particles is the only way to get this information. The analog method allows for complete characterization of both the scattering body and its geometry due to the large scale of the targets. In the analog method we scale the entire problem up by a factor of approximately 6500. The principle of electromagnetic similitude allows us to do this because in the formalism of Maxwell's equations the dimensions of particle size enter only as a ratio to the wavelength of the radiation. Refractive index of the material in the w-band must correspond to that of the simulated material in the visual or other waveband of interest.

The microwave facility at the University of Florida (described in detail in Gustafson 1996) is projected on the scattering plane in Figure 1.2. Radiation is transmitted through the first polarization filter and then scatters from a target where the state of polarization can change (thus the need for the second filter). The output and input signals are then compared by a network analyzer to obtain phase information. The range of scattering angles is 0° - 168° and thus its complement, phase angle, has a range of 12° - 180° . A flat wavefront over a 20-25 cm diameter spherical volume is created by a Fresnel lens system. This means that we can measure the scattering from targets with as large a size parameter as 200. The size parameter, usually denoted x , is defined as $2\pi r/\lambda$ for a sphere of radius, r , and is used to take advantage of the principle of electromagnetic similitude mentioned above.

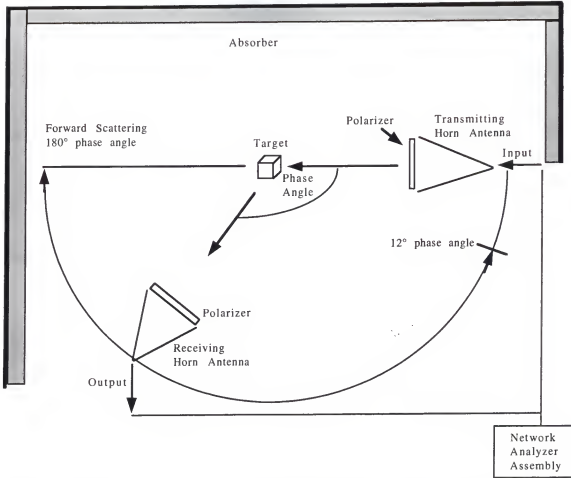


Figure 1.2 Diagram of microwave analog laboratory facility at the University of Florida.

The scattering by a particle can be fully described by measuring the four complex elements, A_{1-4} , of the amplitude scattering matrix, A (van de Hulst 1957; Bohren and Huffman 1983) according to the equation

$$\begin{pmatrix} E_{\parallel} \\ E_{\perp} \end{pmatrix} = \begin{pmatrix} A_2 & A_3 \\ A_4 & A_1 \end{pmatrix} \frac{e^{-ikr+ikz}}{ikr} \begin{pmatrix} E_{\parallel 0} \\ E_{\perp 0} \end{pmatrix} \quad (1.2)$$

where E_{\perp} and E_{\parallel} are scattered components of the electric field parallel and perpendicular to the scattering plane respectively, and $E_{\perp 0}$ and $E_{\parallel 0}$ are the incident components. In our laboratory, these components are determined by measuring the complex amplitudes of the

radiation scattered from the target located centrally between the antennae at the four combinations of parallel and perpendicular incident and scattered radiation. Outside of the laboratory environment, scattered intensities and polarizations from particles are almost always observed from a large population of scatterers, such as a cloud of particles. The observed scattering properties (as measured by the Pioneer and Voyager spacecraft) will be compared with model atmospheres populated with particles in random orientation. Thus the scattering matrix elements are averaged over many particle orientations to simulate such a cloud.

Once one moves away from spherical particles there are a plethora of other shapes to consider and one could go on ad infinitum unless one constrains the problem using some meaningful physical scheme. Single liquid drops can be modeled using spheres for which scattering patterns can be easily calculated with Mie theory. Although these were ruled out above, spheres are useful for comparison purposes because Mie theory provides robust results that can be calculated quickly. We use cubes as a representation of solids with sharp edges that may be expected due to fragmentation. Whereas aggregates can be formed by collisions between viscous semi-liquid spheres that stick together instead of merging (Bar-Nun *et al.* 1988; Scattergood *et al.* 1992; Clarke and Ferris 1997). In this way, the shape of Titan's atmospheric aerosols can be used as a diagnostic for conditions found in the atmosphere.

None of the models to date have solved this problem in a unique way because this is not possible. Therefore it is desirable to explore more of the phase space of possible particle morphologies in order to confirm that the problem is not so underconstrained that any type of model will work. If for example all of the models manage to fit the

observations, this would indicate a serious issue with uniqueness. Previous studies use calculation methods which a priori exclude, due to memory and computing time requirements, much of the phase space that the microwave analog laboratory is ideally suited to explore.

In this work I will present a variety of models chosen for their applicability to Titan's atmosphere based on physical and chemical considerations as well as their practicality and convenience in fabrication. The single scattering characteristics of these models will be discussed in Chapter 2. The method used to make vector radiative transfer calculations and tests and sensitivity studies of this method are presented in Chapter 3. Radiative transfer calculations for model atmospheres containing the model particles will be compared to photopolarimetry obtained by the Pioneer 11 and Voyager 2 spacecraft in Chapter 4. Based on these comparisons, I am able to rule out many models from consideration and suggest the most plausible physical particle models. This type of analysis using single scattering microwave analog measurements as input to radiative transfer calculations and the subsequent comparison of the results with observations is previously uncharted territory.

CHAPTER 2

SINGLE SCATTERING PROPERTIES OF MODELS

In this chapter we explore the particle physical characteristic phase space of morphology, refractive index, and size by comparing the single scattering properties of a variety of models. The properties we are concerned with are the color and polarimetric color and the angular distributions of the intensity and linear polarization. First, we start with the basics necessary for a discussion of the scattering of light including polarization. Second, we review the exact theories and approximations that are used as a comparison to laboratory measurements and to calculate the scattering properties for some parts of the phase space (e.g., where particles are relatively small or spherical). Third, we investigate the characteristics of the models for which microwave analog measurements have been made and the physical rationale behind them. Fourth, we discuss the procedures for collecting data in the laboratory and the data reduction techniques. Fifth, we can compare and contrast the single scattering results for the various models and some comparison theoretical calculations. And finally, these results can be examined in the context of single scattering clues from previous observational studies of Titan.

Electromagnetic Radiation and Polarization

We are interested in the scattering of electromagnetic radiation by particles so we need some background in the propagation of electromagnetic waves. Radiation is produced by an accelerated electric charge and a wave of radiation is produced by an

oscillating electric charge. When an incident wave impinges on any matter its electric field acts on the electric charges in the matter to make them oscillate and thus produces a new scattered electromagnetic wave. This is the essence of the scattering process and describing the nature of this new wave is the problem which all scattering theory and experimentation attempt to solve. The following mathematical description will provide us with a foundation and such background can be found in any text on electromagnetic theory (e.g. Jackson 1975).

The electric field of a monochromatic transverse plane wave travelling through vacuum in the z direction varies with time, t , in the following manner:

$$\mathbf{E}(\mathbf{z}, t) = \text{Re} \{ \mathbf{n} E e^{-i(\mathbf{k} \cdot \mathbf{z} - \omega t)} \} \text{ where } \mathbf{n} E = \mathbf{n}_\perp E_\perp + \mathbf{n}_\parallel E_\parallel \quad (2.1)$$

where \mathbf{k} is the propagation vector and ω is the angular frequency. The propagation vector, \mathbf{k} , is equivalent to $k\mathbf{n}$, the propagation constant or wave number ($k = 2\pi/\lambda$) times a unit vector \mathbf{n} in the propagation direction at wavelength λ . As shown in Figure 2.1, the electric vector can be decomposed into orthogonal components, with complex amplitudes E_\perp and E_\parallel , denoted as perpendicular and parallel to a reference plane respectively. In the discipline of light scattering it is customary to define this reference plane as the scattering plane containing both the incident and scattered propagation vectors, \mathbf{k}_i and \mathbf{k}_s . The scattering angle, Θ , is then defined as the angle between these vectors. In astronomical applications it is common to use the complement of the scattering angle known as the phase angle, α , designated as such because the phase (illuminated portion) of a solar system body varies with phase angle as it moves in its orbit.

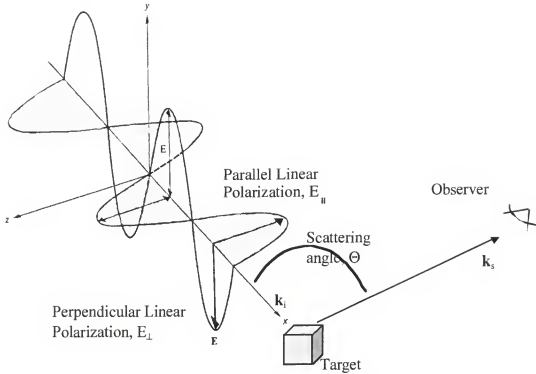


Figure 2.1 Propagation of an electromagnetic wave and depiction of linear polarization.

The scattering process naturally leads to polarization because the equal amounts of perpendicular and parallel linearly polarized light which make up unpolarized incident light from the sun generally interact differently with the scatterer (a simple example of this is dipole radiation as shown in equation (2.16) in the Rayleigh Scattering section below or even the complete perpendicular polarization which occurs due to reflection from a flat dielectric surface at Brewster's angle). The polarization state of a wave describes the time variation of the electric field vector at any given point in space or in other words the pattern of its transverse vibration (vibrations in directions perpendicular to the direction of propagation). Through one complete vibration the endpoint of an electric vector generally traces out an ellipse (shown in Figure 2.2) in a plane

perpendicular to the direction of the wave's propagation. Consider the complex orthogonal components in equation (2.1) with amplitudes denoted a and phase denoted δ .

$$E_{\perp} = a_{\perp} e^{-i\delta_{\perp}} \text{ and } E_{\parallel} = a_{\parallel} e^{-i\delta_{\parallel}} \quad (2.2)$$

If the phases of the two components are equal then the wave is linearly polarized.

Another special case is that of circular polarization in which the components differ in phase by 90° . Generally, however, any other phase difference produces elliptical polarization.

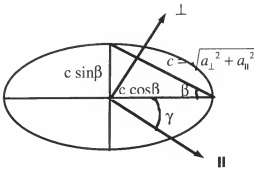


Figure 2.2 The polarization ellipse.

The propagation vector is into the page (a similar figure can be found on the cover of Chandrasekhar (1960)).

There are four geometric or ellipsometric parameters which describe this vibration ellipse: the ellipticity ($|\tan \beta|$), orientation (γ), handedness (sign of β with positive representing right-handed polarization), and intensity ($c = \sqrt{a_{\perp}^2 + a_{\parallel}^2}$, the square of the amplitudes which are the semi-major and semi-minor axes of the ellipse). While these parameters give us a nice picture of the vibration ellipse they are not conducive to measurement. They also only help us describe perfectly polarized light which is not

sufficient for our purposes. A measurable set of four parameters to which the geometric ones are related are the Stokes parameters.

Stokes Vectors

Stokes vectors, denoted \mathbf{I} , are 4-vectors made up of the four Stokes parameters which are a different but equivalent interpretation of the geometric or ellipsometric polarization parameters described in the previous section. The Stokes parameters are defined as:

$$\mathbf{I} = \begin{pmatrix} I \\ Q \\ U \\ V \end{pmatrix} = \begin{pmatrix} \langle E_{\parallel} E_{\parallel}^* + E_{\perp} E_{\perp}^* \rangle \\ \langle E_{\parallel} E_{\parallel}^* - E_{\perp} E_{\perp}^* \rangle \\ \langle E_{\parallel} E_{\perp}^* + E_{\perp} E_{\parallel}^* \rangle \\ i \langle E_{\parallel} E_{\perp}^* - E_{\perp} E_{\parallel}^* \rangle \end{pmatrix} = \begin{pmatrix} a_{\parallel}^2 + a_{\perp}^2 \\ a_{\parallel}^2 - a_{\perp}^2 \\ 2a_{\parallel} a_{\perp} \cos(\delta_{\parallel} - \delta_{\perp}) \\ 2a_{\parallel} a_{\perp} \sin(\delta_{\parallel} - \delta_{\perp}) \end{pmatrix}. \quad (2.3)$$

In reality the electromagnetic waves we deal with are not perfectly monochromatic because they are a superposition of finite wave trains and so ω (in equation (2.1) actually represents some narrow bandwidth, $\Delta\omega$, and the phases and amplitudes are all slowly (with respect to the period of the wave ($1/\Delta\omega$)) varying functions of time. Thus, the parameters are related to time-averaged values of the electric field as shown with the brackets in equation (2.3).

The physical interpretation of these parameters is that I represents total intensity, Q is the difference between the parallel and perpendicularly polarized components, U is the difference between components at angles $+45^\circ$ and -45° with respect to a reference plane (the scattering plane in our world), and V is the difference between left and right circularly polarized components. Unpolarized light gives $Q=U=V=0$ and partially polarized light gives $I > \sqrt{Q^2 + U^2 + V^2} > 0$. Completely polarized light gives

$I = \sqrt{Q^2 + U^2 + V^2}$. Partially polarized light can be thought of as made up of one beam of completely polarized light and one beam of unpolarized light with the degree of polarization specifying how much is contributed by each. The degree of polarization is thus given by $\sqrt{Q^2 + U^2 + V^2}/I$. Furthermore, the degree of linear polarization is $\sqrt{Q^2 + U^2}/I$ and the degree of circular polarization is V/I . When U vanishes due to the choice of coordinate system (such as choosing the incident light to be unpolarized or choosing it to be polarized perpendicular or parallel to the scattering plane as in the microwave analog lab) the degree of linear polarization is given by $-Q/I$.

Scattering by a Single Particle and a Cloud of Particles

This section introduces the basic quantities which are of interest in light scattering studies: the scattering matrix and the optical cross-sections.

Scattering Matrix

The scattering matrix (also known as a Mueller matrix), denoted \mathbf{F} , relates the incident Stokes vector to the scattered Stokes vector according to the following equation:

$$\mathbf{I}_s = \frac{1}{k^2 r^2} \mathbf{F} \mathbf{I}_o \quad (2.4)$$

where k is the wave number and r is the distance from an observer in the far-field to the particle or collection of particles. \mathbf{F} can be derived from the definition of the Stokes parameters in equation (2.3) and the amplitude scattering matrix, shown in equation (1.2), that relates the incident and scattered electric field amplitudes.

According to van de Hulst (1957) the scattering matrix, \mathbf{F} , can be written as a function of the measured scattering amplitude matrix, \mathbf{A} , in the following manner given the real numbers:

$$M_k = A_k A_k^* \quad S_{kj} = S_{jk} = 1/2 (A_j A_k^* + A_k A_j^*) \quad -D_{kj} = D_{jk} = i/2 (A_j A_k^* - A_k A_j^*), \quad (2.5)$$

$$\mathbf{F} = \begin{pmatrix} 1/2 (M_1 + M_2 + M_3 + M_4) & 1/2 (-M_1 + M_2 - M_3 + M_4) & S_{23} + S_{41} & -D_{23} - D_{41} \\ 1/2 (-M_1 + M_2 + M_3 - M_4) & 1/2 (M_1 + M_2 - M_3 - M_4) & S_{23} - S_{41} & -D_{23} + D_{41} \\ S_{24} + S_{31} & S_{24} - S_{31} & S_{21} + S_{34} & -D_{21} + D_{34} \\ D_{24} + D_{31} & D_{24} - D_{31} & D_{21} + D_{34} & S_{21} - S_{34} \end{pmatrix}. \quad (2.6)$$

This form of the scattering matrix is valid for a single asymmetric particle in a single orientation. However, for the purpose of simulating the Titanian atmosphere, we wish to examine the case of a cloud of particles in random orientation. The assumption of independent scattering allows the addition of the scattering matrices of single particles within a cloud to obtain the scattering matrix for the entire cloud.

$$\mathbf{F}_{\text{cloud}} = \frac{1}{N} \sum_i^N \mathbf{F}_i \quad (2.7)$$

Under the condition of independent scattering, the intensities from single scattering events can be added without consideration of their phases because statistically the phase differences will average out (van de Hulst 1957). For illustrative purposes dependent scattering, requires knowledge of the phase relationships between each scattering event. An example of this type of scattering is that which occurs from the constituents of an aggregated particle. In order to completely describe the scattering from such a particle, it is necessary to account for the phase differences between the scattering from each member of the aggregate as is done in Xu's exact theory for multi-sphere aggregates (Xu 1995; Xu 1997; Xu and Wang 1998).

Even without any symmetries in the target or within the particle population we can make some simplifications to the scattering matrix. The details of this argument are nicely laid out in both Bohren and Huffman (1983) and van de Hulst (1957), so only a brief overview follows. First, given the amplitude scattering matrix for any particle in a particular orientation, the amplitude scattering matrix for the same particle in its reciprocal position is easily determined due to the reciprocity theorem for vector waves.

$$\mathbf{A} = \begin{pmatrix} A_2 & A_3 \\ A_4 & A_1 \end{pmatrix} \quad \mathbf{A}_{reciprocal} = \begin{pmatrix} A_2 & -A_4 \\ -A_3 & A_1 \end{pmatrix} \quad (2.8)$$

Every particle, regardless of symmetry, has a reciprocal position. The reciprocal position is obtained by rotation of the original particle such that the scattered and incident directions are exchanged. As shown in Figure 2.3, the original particle is rotated by 180° around the axis perpendicular to the incident direction (x-axis in figure) and then by $180^\circ - \Theta$ around the axis perpendicular to the scattering plane (x-z axis in the figure).

The scattering matrices corresponding to the original and reciprocal amplitude scattering matrices can be found using equation (2.6) and the scattering matrix for the entire ensemble is then merely the sum of these. This leads to the following scattering matrix with ten independent parameters (van de Hulst 1957).

$$\mathbf{F}(\Theta) = \begin{pmatrix} a_1 & b_1 & b_3 & b_5 \\ b_1 & a_2 & b_4 & b_6 \\ -b_3 & -b_4 & a_3 & b_2 \\ b_5 & b_6 & -b_2 & a_4 \end{pmatrix} \quad (2.9)$$

It is valid for the case of a cloud of asymmetric particles in random orientation that necessarily contains particles and their reciprocals. If we now include mirror particles

and their reciprocals in the cloud, the level of symmetry in the scattering matrix is increased.

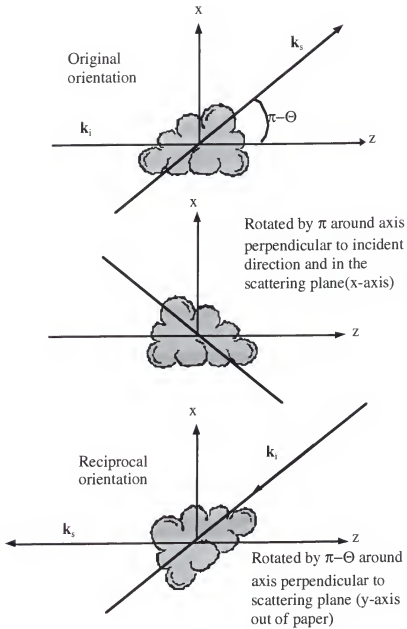


Figure 2.3 Reciprocal orientation

A mirror particle is simply a reflection in the scattering plane. The mirror and mirror reciprocal orientations are depicted in Figure 2.4. The amplitude matrix for the reciprocal of the mirror is then found directly by equation (2.8).

$$\mathbf{A}_{mirror} = \begin{pmatrix} A_2 & -A_3 \\ -A_4 & A_1 \end{pmatrix} \quad \mathbf{A}_{mirror\ reciprocal} = \begin{pmatrix} A_2 & A_4 \\ A_3 & A_1 \end{pmatrix} \quad (2.10)$$

By including all four positions, the number of independent elements in the scattering matrix is decreased to six as shown below (van de Hulst 1957).

$$\mathbf{F}(\Theta) = \begin{pmatrix} a_1 & b_1 & 0 & 0 \\ b_1 & a_2 & 0 & 0 \\ 0 & 0 & a_3 & b_2 \\ 0 & 0 & -b_2 & a_4 \end{pmatrix} \quad (2.11)$$

The preceding matrix is valid for a cloud of particles and their mirror particles in equal numbers in random orientation or for particles with a plane of symmetry in random orientation (van de Hulst 1957). A cloud with this form of the scattering matrix is also known as a macroscopically isotropic and symmetric media (Mishchenko *et al.* 2000).

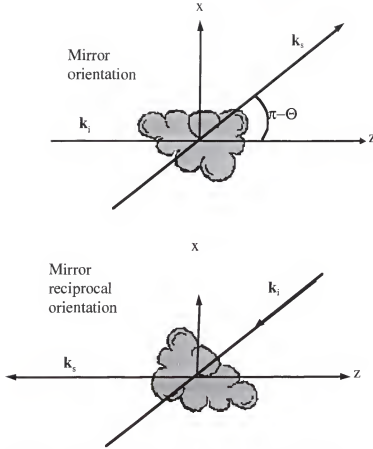


Figure 2.4 Mirror and mirror reciprocal orientations.

Scattering, Absorption, and Extinction Cross-Sections and Efficiencies

The scattering cross-section represents the hypothetical area that an incident beam would need to traverse in order to remove an amount of energy equal to that scattered in all directions by the particle. It can be directly calculated from the top-left corner element of the scattering matrix, F_{11} , by the following equation (van de Hulst 1957):

$$C_{sca} = \frac{2\pi}{k^2} \int_{\pi} F_{11}(\Theta) \sin \Theta d\Theta \quad (2.12)$$

where k is the wave number and Θ is the scattering angle.

The absorption cross-section represents the hypothetical area that an incident beam would need to traverse in order to remove an amount of energy equal to that absorbed within the particle. Absorption here means that the incident radiant energy is transformed into another type of energy (e.g. kinetic). For the purpose of this work we will not be concerned with where this energy goes but simply that it is removed

The extinction cross-section then represents the hypothetical area that an incident beam would need to traverse in order to remove an amount of energy equal to that absorbed and scattered by the particle. Thus it is simply the sum of the scattering and absorption cross-sections,

$$C_{ext} = C_{abs} + C_{sca}. \quad (2.13)$$

The fundamental extinction theorem (van de Hulst 1957) gives the extinction cross-section as:

$$C_{ext} = \frac{4\pi}{k^2} \text{Re}\{A_{\theta=0}\}. \quad (2.14)$$

The efficiencies for scattering, absorption, and extinction are dimensionless quantities which represent the effectiveness with which a particles scatters, absorbs, or removes radiation compared to its geometric cross-section.

$$Q_{sca} = C_{sca}/G \quad Q_{abs} = C_{abs}/G \quad Q_{ext} = C_{ext}/G \quad (2.15)$$

A quantity used in radiative transfer modeling is the single scattering albedo, denoted a . It is the ratio of the scattering to extinction cross-sections or efficiencies.

Scattering Calculations

There are many different methods of calculating the scattering by an arbitrary particle in use today. Choosing one technique over another requires an evaluation of their strengths and weaknesses for the type of particle to be considered. This section is meant to serve only as an introduction and overview of those theories and approximations that are employed in this work.. For a more complete review of a larger variety of methods see (Mishchenko *et al.* 2000).

Rayleigh Scattering

Scattering by all particles, regardless of shape or index of refraction, that are very small compared to the wavelength is commonly termed Rayleigh scattering although, in the strictest sense this approximation is valid only for non-absorbing particles. Thus the validity criterion (also known as the Rayleigh limit) is $|m|x \ll 1$, where x is the size parameter relating the characteristic size of the particle to the wavelength of the radiation. Discussions and derivations of the formulas for the scattering matrix and cross-sections can be found in many light scattering texts (i.e. Bohren and Huffman (1983) and van de Hulst (1957)).

For our purposes it is sufficient to note that an acceptably small particle of any shape can be approximated by a single dipole with a polarizability, α , calculated from electrostatic theory. A dipole is a dielectric bit of matter whose dimensions are much smaller than the wavelength of the incident radiation. Polarizability is a measure of a material's inherent reaction to an electric field due to its molecular and atomic structure. Thus the field scattered from a sufficiently small particle is consistent with dipole

radiation. The case for isotropic polarizability is shown below (in the anisotropic case, α becomes a tensor):

$$\begin{aligned} \mathbf{E}_{\parallel} &= \frac{e^{-ik(r-z)}}{r} \alpha \cos \Theta \mathbf{E}_{\parallel 0} \\ \mathbf{E}_{\perp} &= \frac{e^{-ik(r-z)}}{r} \alpha \mathbf{E}_{\perp 0} \end{aligned} \quad (2.16)$$

Mie Theory – Spheres

Mie theory is an exact method of calculating the scattering of a plane wave of electromagnetic radiation from a homogeneous sphere. Developed in 1908 by Gustav Mie, it is the solution of Maxwell's equations, for the electric and magnetic field vectors, using the boundary conditions appropriate for a sphere. The solution is dependent on the complex refractive index, m , of the material and the size parameter of the sphere, $x = 2\pi r/\lambda$ where r is the radius of the sphere and λ is the wavelength of the radiation. A good description of the solution and its implementation can be found in (van de Hulst 1957; Bohren and Huffman 1983).

Mie theory is still, arguably, the most widely used method to calculate the scattering properties of particles regardless of shape. This may seem somewhat peculiar considering a sphere has many characteristics which make it a poor (and maybe the poorest) approximation to any other shape, notably surface smoothness and a complete lack of edges. Spheres are sufficiently different from any other shape that they should not necessarily be expected to reproduce the scattering by other shapes. For many years, however, Mie theory represented the only viable alternative to building an experimental apparatus and so it was used, independent of suitability.

Exact Multisphere Scattering Theory

This theory, developed by Y.-L. Xu (1995; 1997), is an extension of the Mie solution for one sphere to an aggregate of spheres. The solution of the scattered fields due to each of the constituents is a generalization of Mie theory for one sphere that accounts for the interaction between the spheres (in the sense that scattered radiation from one sphere can be incident upon another). This is done using a system of linear equations to represent the interactions. In this formulation the constituents are spheres but theoretically they could be anything for which a solution could be formed in an expansion in terms of vector spherical wave functions. The total scattered field due to the aggregate is then simply the superposition of scattered fields from all of the constituents. As with almost any theoretical calculation, there is a point at which as the size of the particle gets larger, the computing time or memory makes the calculation impractical. Thus, this method is only used in this work for relatively small aggregates.

Discrete Dipole Approximation

The Discrete Dipole Approximation (DDA) is an implementation (Draine 1988; Draine and Flatau 1994) of Purcell and Pennypacker's (1973) coupled dipole approximation. In this implementation a particle is divided into N dipoles placed in a cubic array. The electric field at any dipole is then just the incident field plus the scattered radiation from all the other dipoles. The scattered field at any point in space due to the entire particle can then be calculated by adding the contributions from each dipole.

The number of dipoles needed for an accurate calculation is based on the criterion that the interdipole separation be small compared to any structural inhomogeneities in the particle and the wavelength, λ , (Draine and Flatau 1997). Draine and Flatau (1994) suggest that this interdipole separation, d , should satisfy the following criterion:

$$|m|kd < 1, \text{ where } m \text{ is the complex refractive index and } k \text{ is the wavenumber } (2\pi/\lambda).$$

Thus, the interdipole separation should be smaller than the wavelength of the radiation inside the particle. This translates into a constraint on N when an effective radius for a sphere of equal volume is defined as $a_{\text{eff}} = (3V/4\pi)^{1/3}$ where $V = Nd^3$ when the dipoles are aligned in a cubic array. This becomes important because the amount of computing memory and time needed for these calculations increases as N increases and thus becomes prohibitive for large sizes and refractive indices. When compared with an exact theory for multiple spheres (discussed above) it is found that the DDA estimates for cross sections are accurate to about 5% when $|m|kd < 0.5$ (Xu and Gustafson 1999) for low refractive indices and small sizes (i.e. $|m|x_{\text{eff}} < 10$, where $x_{\text{eff}} = 2\pi a_{\text{eff}}/\lambda$ is the effective size parameter). At larger sizes and refractive indices the errors become larger and computing times become prohibitive. Thus DDA can be useful for examining the scattering characteristics of non-spherical, small (although larger than the Rayleigh limit) particles that are not highly absorbing.

Effective Medium Theory

Effective medium theories (EMT) are a class of approximations whereby an inhomogeneous particle is represented by a homogeneous particle with an effective or average refractive index. There are many different effective medium theories based on

the type (size and shape) of inhomogeneities and the topology (separated or aggregated) of the medium. The two most commonly used theories are the Maxell-Garnett mixing rule, in which the inhomogeneities are smaller than the Rayleigh limit and are imbedded in a matrix material such that they are isolated, and the Bruggeman mixing rule, in which the inhomogeneities are also smaller than the Rayleigh limit but are arranged randomly along with units of the matrix material in an agglomerated structure. The particulars of the most popular theories as well as a discussion of their validity can be found in Kolokolova and Gustafson (2000). An effective medium theory can be used to determine an approximate refractive index that can be used in a scattering calculation appropriate for the geometry of the inhomogeneous particle.

Laboratory Models and the Rationale Behind Them

Two types of models were measured in the microwave scattering facility. Here I will discuss why these particular models were chosen or built. Shown in Table 2.1 and Table 2.2 is a list of all of the targets measured. Some preliminary results are also presented here for illustrative purposes in discussing target differences. See the Single Scattering Measurements section for an explanation of how these results are obtained.

Cubes

Cubes are used to represent particles with edges and corners due to fragmentation that, for example, might be the result of collisions. They can also be used as an example of a particle with crystalline structure that might be found in ices. The cubes I measured in the laboratory are made of acrylic that has an index of refraction near $1.6-0.003i$. This

is in fact similar to the indices of refraction for tholin ice (as shown in Table 1.1) at UV to blue wavelengths. It is also similar to the index of refraction of silicates in the visual wavelength range and thus the cubes might represent rock dust. I measured cubes of two different sizes at many orientations. The actual target sizes are 0.5" and 1.5" which correspond to sizes of approximately $2\text{ }\mu\text{m}$ and $6\text{ }\mu\text{m}$ at visual wavelengths. I also measured a smaller cube (0.25") and a larger (4") cube at a few specific orientations. These would correspond to sizes of $1\text{ }\mu\text{m}$ and $17\text{ }\mu\text{m}$, respectively. Figure 2.1 shows these targets and Table 2.1 displays their physical characteristics. It should be noted here that corresponding sizes are approximate because there is range of wavelengths measured in the laboratory and thus there is also a range in the corresponding sizes in the visible.

Table 2.1 Physical characteristics of cube targets.

Cubes	Material	Refractive Index	Actual Size (mm)	Equivalent Surface Area Size Parameter Range	Equivalent Volume Size Parameter Range
0.25"	Acrylic	1.605-0.003i	6.415	6.96 – 10.3	6.25 – 9.26
0.5"	Acrylic	1.605-0.003i	12.57	13.6 – 20.2	12.2 – 18.1
1.5"	Acrylic	1.605-0.003i	38.42	41.7 – 61.8	37.4 – 55.5
4"	Acrylic	1.605-0.003i	101.6	110 – 162	98.5 – 146

Note: Range in equivalent size parameters is due to wavelength band measured in the analog laboratory.



Figure 2.5 Photograph of the four acrylic cubes.

Aggregates

I made measurements of six different aggregates, which for lack of a better nomenclature I call the little sphere aggregate (LSA), the big sphere aggregate (BSA), the cylinder aggregate (CYA), the organic aggregate (OA), the compact aggregate (CA), and the string aggregate (SA). These targets are shown in Figure 2.6 through Figure 2.11 and Table 2.2 displays their physical characteristics. They are part of an ongoing systematic survey of light scattering by aggregates in the microwave facility at the University of Florida (Gustafson and Kolokolova 1999). The first three targets were made with the help of Jacques Loesel, an undergraduate engineering student who worked with our group during the summer of 1997. The organic aggregate is my representation of aggregates of the cyanoacetylene-acetylene copolymers which were produced by irradiation of a simulated Titanian atmosphere (Clarke and Ferris 1997). The compact and string aggregates were originally assembled by Gustafson.

Table 2.2 Physical characteristics of aggregate targets.

Aggregate	Material	Refractive index	Constituents			Packing factor
			Actual Size (mm)	Size parameter range	#	
LSA	Polystyrene spheres	1.6-0.03i	$\bar{d}=0.65$, $\sigma \approx 0.35$	[0.51,0.76]	1450 \pm 20	~ 0.2
CYA	Nylon 2:1 cylinders	1.714-0.005i	d=1.25, l=2.5	[0.98,1.45]	1430 \pm 20	~ 0.05
BSA	Nylon spheres	1.714-0.005i	d=1.5	[1.18,1.75]	1425 \pm 20	~ 0.05
SA	Nylon string	1.714-0.005i	d=1.25, l=1660 cm	[0.98,1.45]		<0.05
CA	Nylon cylinders in an absorbing matrix	1.714-0.005i and 1.7-0.018i	d=1.25, l=2.5	[0.98,1.45]	~ 3000	~ 1
OA	Absorbing spheroids	1.7-0.2i	$\bar{d}=4$, $\sigma \approx 2.5$	[3.14,4.65]	88	~ 0.2

Note: \bar{d} represents the mean constituent diameter, and σ is the standard deviation in the constituent diameter. The method of determination of the packing factor is given in the Porosity section later in this chapter.

The LSA is made of 1450 \pm 20 polystyrene spheres with an average diameter of 0.65 \pm 0.35 mm. The spheres were purchased from Bangs Laboratories Inc. and glued together with super-glue. Polystyrene has an index of refraction, $n=1.6-0.03i$, similar to acrylic but slightly more absorbing.

This aggregate has two purposes. First, at the wavelengths of the Pioneer photopolarimetry (0.452 μm and 0.648 μm) polystyrene is a fair approximation of Titan Tholin (see Table 1.1) as determined from chemical simulations (Khare *et al.* 1984) and the size of the constituent spheres at these wavelengths is also close to the size of West

and Smith's (1991) fit to the polarization data. The size parameter, x , of the little spheres is near 0.65 in the laboratory which corresponds to radii of approximately $0.047\text{ }\mu\text{m}$ and $0.067\text{ }\mu\text{m}$ at wavelengths $0.452\text{ }\mu\text{m}$ and $0.648\text{ }\mu\text{m}$, respectively. Thus, this aggregate represents the same type of aggregate which is now the working model for Titan's aerosols except that it has grown and has many more constituents.

The second purpose is really only a side-note to this particular work but it serves as an interesting comparison and suggests that nature finds certain configurations repeatedly. Aggregates of spheres of this size can also represent an aggregate of classic interstellar grains without an organic mantle and is a larger example of a "Bird's-Nest" type of model (Greenberg and Gustafson 1981). A further discussion of the LSA model in this context can be found in our group's publications (Gustafson *et al.* 1998; Gustafson and Kolokolova 1999).

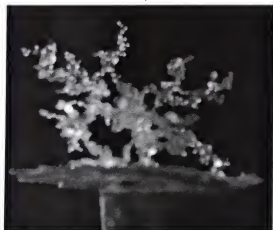


Figure 2.6 Photograph of the LSA on a Styrofoam support.

The BSA is made of 1425 ± 20 spheres of nylon with diameters of 1.58 mm , purchased from McMaster Carr, also assembled with super glue. Nylon has a refractive index of $1.74 - .005i$. This can be used to approximate the index for Tholin in the near IR.

The CYA is similar to the BSA but made of cylinders instead of spheres. The cylinders have a diameter of 1.25 mm, aspect ratio of 1:2 and are also made of nylon. The volume of the BSA constituents is about 10% larger than the CYA constituents. The larger size of these constituents as compared to the LSA would represent an actual size of approximately $0.2\text{ }\mu\text{m}$ in the Titanian atmosphere. Thus, the BSA model represents an aggregate of larger constituents (by a factor of two) than may be expected based on previous studies to exist in Titan's atmosphere. The CYA model is then used to examine how the shape of the constituents in an aggregate affects its scattering properties.

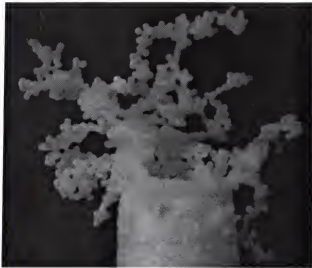


Figure 2.7 Photograph of the BSA on a Styrofoam support.



Figure 2.8 Photograph of the CYA on a Styrofoam support.

The OA was made to have an aggregate with a significantly higher absorption than the rest. The index of refraction of this material is similar to Tholin in the UV. It has approximately 90 spheroids glued together with super-glue. The material was made specially out of plaster, acrylic paint with iron pigment, and a plastic model foam called “Model Magic” to achieve an appropriate index of refraction. The size of the constituents ideally would have been smaller but working with this material to make significantly smaller constituents is nearly impossible without using an entirely different and more elaborate fabrication scheme. The size parameter of the constituents are about three times larger than those of the other aggregates. It is also elongated in one axis whereas the above aggregates are more equidimensional.

This aggregate was modeled after the results of Clarke and Ferris’ (1997) photopolymerization experiments. Previous experiments studying the polymerization of polyacetylene produced spherical particles that have a tendency to stick together as aggregates of spheres. They seem to retain their shape as they aggregate. Clarke and

Ferris however, studied the co-polymerization of cyanoacetylene and acetelyne and produced slightly different aggregates. The individual particles seem to have a larger size distribution and are more irregular in shape although still spheroidal. When they aggregate they seem to make large cauliflower looking equidimensional objects which are connected by smaller chains (see Clarke and Ferris 1997, Figure 13). Although all of the above experiments were conducted at room temperature, a far cry from Titan's stratospheric temperature of 170 K, they provide the best estimates so far from chemical simulations. These aggregates are made of viscous liquids that at lower temperatures might be solid. How this would affect their aggregation (i.e. sticking probability) and the shape of the individual particles is hard to estimate.



Figure 2.9 Photograph of the OA.

The last two aggregates do not have the same morphology as those above. The SA is a long string of nylon (weed-wacker line) wound into tangles. It has about four times the material as the CYA but spread out over a much larger volume and so it has a lower density. It would be very difficult to make such a large model aggregate in the same way as the CYA, BSA, and LSA because it would be too fragile to stay together. The SA represents the largest overall aggregate with the lowest packing factor, the kind of particle one might expect to form in cluster-cluster aggregation. The motivation behind this particle was to test the effect of fluffiness on particle scattering characteristics. The

CA is the other extreme. It consists of approximately 3000 nylon cylinders of the type in the CYA embedded in a matrix of material similar to that of the OA but slightly less absorbing. So this represents the densest aggregate in our set. The effective refractive index (see the Effective Medium Theory section above for an explanation) for the combination of the nylon cylinders and the more absorbing mantle is a good match to Tholin at the red wavelength (648 nm).



Figure 2.10 Photograph of the SA.



Figure 2.11 Photograph of the CA.

For comparison purposes I present some multi-sphere aggregate calculations carried out by Dr. Yu-Lin Xu. This model, significantly smaller than those above and further described in Table 2.3, is made up of 10 spheres with radius $0.06\text{ }\mu\text{m}$. The scattering from this model is calculated at four wavelengths that are chosen to coincide with the Titan photopolarimetry observations. The index of refraction varies with wavelength, as is the case with most materials in the visual, and in fact matches that chosen by West and Smith (1991). Thus, this aggregate resembles very closely those that West and Smith (1991) and Lemmon (1994) claim as their working models.

Table 2.3 Multi-sphere aggregate characteristics

Aggregate	Wavelength (nm)	Size Parameter of constituents	Index of Refraction	Equivalent Volume Size Parameter	Equivalent Surface Area Size Parameter
X1	264	1.43	1.7-0.21	3.0765	4.5157
X2	452	0.834	1.7-0.085	1.7969	2.6375
X3	648	0.582	1.7-0.023	1.2534	1.8397
X4	750	0.503	1.7-0.013	1.0829	1.5895

Note: The scattering characteristics for one aggregate are reported for four wavelengths and denoted X1 through X4.



Figure 2.12 Representation of X1-4 aggregate.

Single Scattering Measurements

The measurements made in the microwave analog laboratory consist of the complex amplitudes, which make up the scattering amplitude matrix, as a function of scattering angle and frequency. The scattering matrix, \mathbf{F} , and thus the angular distributions of intensity, polarization, and color are all derived from this basic information in the following manner.

Procedures

A set of measurements for one target is made up of the complex amplitudes measured as a function of scattering angle for multiple frequencies and orientations at two or four polarization combinations plus the background measurement for the same laboratory configuration. The scattering angle range is 0 - 165° and the resolution varies between 0.1 - 5° (the higher the resolution, the longer the measurement takes). For the measurements reported here the number of discrete frequencies measured is 85. The lab is capable of measuring 501 frequencies, however, this also leads to significantly longer measurement times and larger data files, both of which become prohibitive when measuring multiple orientations. The aggregates all have between 12-36 orientations whereas the cubes need more orientations due to a strong dependence on orientation in the scattering pattern (c.f. Figure 2.14 in the Averaging over orientation section below). The individual orientations are obtained using a motorized rotation table which rotates the target support via computer control. Thus, a certain number of orientations are

measured for each axis of rotation chosen. There are four possible combinations of polarization state considering the incident and scattered beams can both be polarized linearly or perpendicularly (in reference to the scattering plane). Some measurement sets do not include cross-polarization (e.g. the incident beam is linearly polarized and the receiver is measuring perpendicularly polarized radiation or vice versa), meaning the scattering amplitudes A_3 and A_4 are not measured and these are denoted as having only two polarizations. The background measurements are made by repeating the same exact measurements with the target removed and are then vectorially subtracted from the target measurement to produce the scattered signal. In the forward direction ($\theta=0^\circ$), this can be a difficult task because the background contains the direct signal so the desired scattered signal is very small compared to the background. Thus, the errors tend to be largest here.

Table 2.4 List of microwave analog laboratory measurements.

Target	Polarization Combinations	Scattering Angle Resolution (deg)	Orientations
CYA	4	5	36
BSA	4	5	12
LSA	2 and 4	1 and 5	36 and 12
SA	2 and 4	2 and 5	21 and 12
CA	4	5	19
OA	4	1	24
1.5" cube	2	2	126
0.5" cube	2	2	126

Note: These measurements were made between May 1996 and May 1998.

Data Reduction

Data reduction begins with the subtraction of the background as mentioned above. This produces the uncalibrated amplitude scattering matrix. The scattering matrix is calculated from this using equation (2.6). The next step is orientational averaging. Lastly, calibration is needed to produce an applicable scattering matrix. Several important characteristics, namely polarization, color, polarimetric color, and scattering cross-sections, can be extracted from the scattering matrix as a function of scattering angle and frequency.

Averaging over orientation

For a target with no symmetries, measurements are made about some number of axes of rotation. The measurements are then averaged with equal weights. Symmetry in the target can reduce the number of orientations which need to be measured and the measured orientations which represent one or more possible orientations must then be weighted accordingly.

A cube, for example as seen in Figure 2.13, is weighted according to $w = \cos \tau + \sin \tau$, where τ is the tilt angle of an axis through the center of the cube and perpendicular to two faces. The azimuth, angle of rotation about the axis perpendicular to the scattering plane through the center of the target, is evenly weighted assuming measurements are made at uniformly distributed intervals. Thus, measurements need only be made for tilt angles up to 45° .

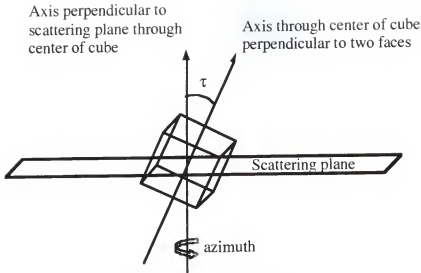


Figure 2.13 Designation of orientations for a cube.

In order to simulate a cloud of cubes it is necessary to measure many orientations and take an average. The number of orientations required is large for larger cubes. The reason for this is evident if one considers a geometrical optics approximation where the specular reflection and the once refracted and reflected components of the scattering dominate. Thus, the angular scattering pattern at each orientation is dominated by these components, shown in Figure 2.14, whereas for a smooth distribution of orientations the angular pattern should not show such peaks which are clearly related to a specific orientation.

Included in the average over orientation are the reciprocal, mirror, and mirror reciprocal positions discussed in the section Scattering Matrix above. The amplitude matrices, and thus the scattering matrices, for these orientations are determined readily from equations (2.8) and (2.10). The format of scattering matrices is then that found in equation (2.11).

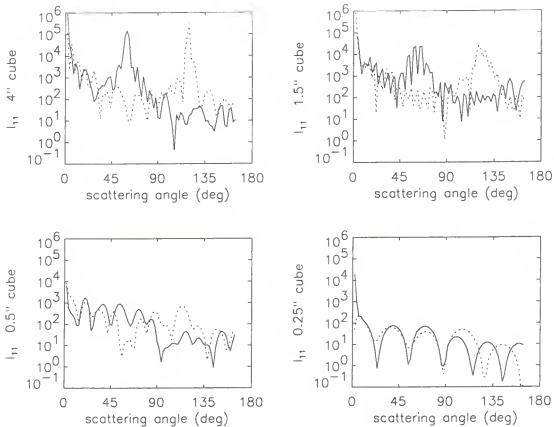


Figure 2.14 Single orientation intensity measurements for four different size cubes. Intensity scattered perpendicular to the scattering plane as a function of scattering angle for four different size cubes (4", 1.5", 0.5", 0.25") at two different orientations denoted as azimuth 30° and 60° plotted with solid and dotted lines, respectively. In these cases the cubes are aligned such that two of their faces are parallel to the scattering plane and two of their faces make angles of either 30° or 60° with a line between the transmitter and receiver.

Calibration

The analog laboratory measures intensity in arbitrary units and thus calibration is required. This calibration is performed by measuring the scattering by a sphere of optical quality BK-7 glass and comparing to Mie calculations for that sphere. This process must be performed carefully at each frequency. Some uncertainty in this calibration can result

from uncertainty in the index of refraction of the glass which is determined by fitting the best Mie curve to the laboratory data.

Scattering matrix as a function of scattering angle.

The scattering matrix is calculated from the measured scattering amplitudes according to equation (2.6). The scattered intensity, given incident Stokes vector of $[1 \ 0 \ 0 \ 0]^T$, is simply F_{11}/k^2r^2 and the degree of linear polarization of the scattered radiation is $-F_{12}/F_{11}$. The other elements in the scattering matrix are useful when considering incident light that is polarized to some degree as would be the case for multiple scattering when the scattered light from one particle is included in the light incident on another (c.f. Appendix C). The deviation of the ratio F_{22}/F_{11} from one is an indication of non-sphericity as is the deviation of F_{33}/F_{11} from F_{44}/F_{11} .

At this point in the reduction, we are confronted with a 4x4 scattering matrix as a function of frequency and scattering angle. Figure 2.15 and Figure 2.16 show examples of how much data is generated for each target. These figures are surface plots of intensity (in units of the scattering matrix) and the degree of linear polarization as a function of scattering angle and laboratory frequency. In order to reduce this amount of data to something more manageable and to compare our data to actual observations, we perform what is essentially an integration across a waveband as would be done if one was observing a source using a filter. This separation into what we will call the red and blue laboratory wavebands is discussed in the next section on color.

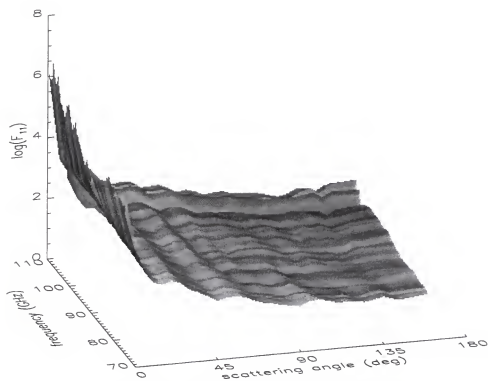


Figure 2.15 Surface plot of intensity as a function of scattering angle and frequency. These data and those in the next figure are for the LSA.

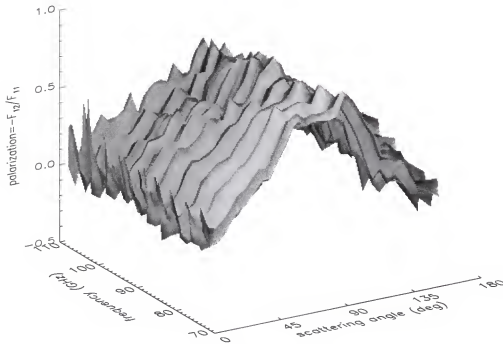


Figure 2.16 Surface plot of polarization as a function of scattering angle and frequency.

Color and polarimetric color

It may be recalled that the measurements made in the microwave analog laboratory at UF are broadband in nature and for the purposes of this thesis were made at 85 distinct frequencies. This allows for the determination of how the scattering properties of a target change with wavelength when the index of refraction of the material is held constant. This is because most materials have constant or nearly constant indices of refraction in the microwave region of the spectrum.

The characteristic of intensity variation with wavelength is known as color because, in the visible part of the spectrum, we identify certain wavelengths with certain

colors. So, for example, if something emits or scatters more radiation at 700 nm than it does at 500 nm, we would say it is red because we associate 700 nm with the color red. In the wavelengths outside the visual range (most of the spectrum) this nomenclature is a misnomer in the sense that these wavelengths have no colors assigned to them. However, since we are making an analogy between the laboratory microwaves and visual wavelengths, we will retain the concept of color as our examination of the variation of the intensity with wavelength.

The blue waveband is defined with laboratory wavelengths in the range $2.7 - 3$ mm which corresponds to a visual waveband with the range 443 - 492 nm and an effective (mid-band) wavelength of 468 nm (when a scale factor of 6100 is used). The red waveband is defined with laboratory wavelengths in the range $3.5 - 4$ mm which corresponds to a visual waveband with the range 573 - 656 nm and an effective wavelength of 615 nm. These bands were chosen so that they would coincide as closely as possible to the filters used in the Pioneer 11 photopolarimeter. The entire laboratory waveband is not wide enough to encompass both of these filters completely (as they are moderately wide band filters). From this it is evident that the laboratory blue band is slightly redder than the blue Pioneer 11 filter and the laboratory red band is slightly bluer than the red Pioneer 11 filter. The wavelengths of the Voyager 2 photopolarimeter filters are separated such that it is impossible to fit them both within the laboratory band.

The scattered color is calculated by summing the (measured intensities) laboratory wavelengths within the two wavebands defined above and then taking their ratio in a manner similar to color indices (e.g. B-V which are astronomical magnitude differences corresponding to flux ratios). This gives color as a function of scattering angle which is

then averaged over the range 5° - 165° to provide a single quantitative measure. Given that intensity is determined from the scattering matrix according to equation (2.4), the expression for color is:

$$B - R = \frac{\sum_{\Theta=5}^{N_\Theta=165} 2.5 \log \left(\frac{\sum_{\lambda=3.5mm}^{\lambda=4mm} F_{11}(\Theta, \lambda) (\lambda / 2\pi)^2}{\sum_{\lambda=2.7mm}^{\lambda=3.5mm} F_{11}(\Theta, \lambda) (\lambda / 2\pi)^2} \right)}{N_\Theta}. \quad (2.17)$$

This quantity is negative if there is more flux at the blue wavelengths than at the red wavelengths. The factor of 2.5 comes from the definition of the astronomical magnitude scale.

Polarimetric color or the wavelength dependence of polarization is another parameter which can be helpful in learning about particles from their scattered light. It is defined as the difference between the polarization in the red and polarization in the blue ($PC = P_R - P_B$) and is also sometimes averaged over scattering angle or a specific range in scattering angles depending on the problem at hand. It is given in percent and a positive value corresponds to more polarization in the red wavelengths. This quantity is also averaged over the same range of scattering angles as the B-R color index.

Porosity

Porosity, defined as the ratio of the volume of voids to the volume containing the mass of a particle, is a volume averaged quantity and is determined from photographs of the targets and some basic image analysis. The porosity, p , is related to the packing factor by $p = 1 - pf$. The packing factor is the ratio of the volume containing the mass of the particle to the volume of the entire particle (material plus voids). To determine the

volume of the entire particle an effective radius, R_{eff} , can be defined as the radius of a homogeneous sphere with equal radius of gyration (c.f. Appendix A). This effective radius is an appropriate size to characterize volume averaged quantities like porosity. If the aggregate is not spherical in overall shape but rather elongated in one axis, then one can use the same reasoning but instead have effective semi-major and semi-minor axes for a spheroid.

The packing factor is determined from the total volume of all of the constituents in the aggregate, NV_c , and volume of an object (sphere or ellipsoid depending on whether the aggregate is equidimensional or not) with equal radius of gyration. For a spherical volume, the following expression is valid:

$$pf = \frac{NV_c}{V_{\text{eff}}} = \frac{NV_c}{\frac{4}{3}\pi R_{\text{eff}}^3} = \frac{NV_c}{\frac{4}{3}\pi \sqrt{\frac{5}{2}} R_g^3}. \quad (2.18)$$

Single Scattering Results from the Laboratory and Theory

This section presents the bulk of the single scattering information extracted from the microwave measurements of the scattering from all the targets. Scattering matrices are presented in the red and blue laboratory wavebands in Figure 2.17 through Figure 2.25. Appendix B shows integrations over the entire laboratory band. The color, polarimetric color, maximum degree of polarization in the two wavebands, and the scattering angles at which these maximums occur are presented in Table 2.5.

Both cubes show a similar blue polarimetric color (more blue than any of the other targets in this study) whereas the large cube has a blue color and the small cube is neutral. The aggregates with the smallest imaginary indices of refraction (those made of

nylon including the BSA, CYA, and SA) also show blue color. Whereas the targets with higher imaginary indices (the OA and CA) have red colors. All of the porous aggregates with the exception of the OA show red polarimetric color. The targets with higher imaginary indices (the OA and CA) show another similar trend in their blue polarimetric color.

Table 2.5 Summary of some single scattering results.

Target	B-R	PC (%)	P _{max} (%)		Θ ° @ P _{max}	
			Blue	Red	Blue	Red
CYA	-0.25	2.0	26	30	60	120
BSA	-0.36	8.1	24	31	40	105
LSA	-0.26	5.3	60	69	90	95
SA	-0.37	25	26	50	50	105
CA	0.24	-6.1	58	34	75	55
OA	0.18	-5.5	33	33	102	71
0.5" cube	0.01	-10	28	9	52	76
1.5" cube	-0.09	-10	66	52	54	50
Colors not independent of refractive index						
X2/X3	-1.51	0.4	99	100	93	91
X2/X3 constituent	-1.52	0.0	100	100	93	91

Note: All results except those for X2 and X3 are calculated from microwave measurements. The X2/X3 results are determined from light scattering calculations made by Yu-Lin Xu where B = 452 nm (X2) and R = 648 nm (X3) instead of the scaled laboratory values of 468 nm and 615 nm.

The positions and values of the polarization maximum for the non-porous particles (the CA and cubes) are similar in that they have intermediate maximum values and positions shifted to scattering angles lower than 90° in the 50-80° range. The aggregates on the other hand show that the maximum polarization increases as the size of the constituent decreases. The position of the maximum varies more as its value

decreases indicating that the curve becomes more broadly peaked (c.f. Figure 2.20 through Figure 2.24).

These results regarding the aggregates are consistent with a systematic survey of color and polarimetric color (Gustafson and Kolokolova 1999) that concludes that increasing the size of the constituents in an aggregate results in redder colors and bluer polarimetric colors. The same conclusion is drawn for increasing the imaginary part of the refractive index. Note that the colors and polarimetric colors in the survey are determined for averages over a narrower range of scattering angles than used in this work ($80\text{-}140^\circ$ instead of $5\text{-}165^\circ$). The smaller range is appropriate for making comparisons to observations of comets.

The systematic survey did not include any really small aggregates like X2 and X3. This aggregate is similar to the LSA in constituent size and refractive index but is significantly smaller in overall size. These colors are not independent of the change in refractive index with wavelength due to the fact that tholin's refractive index was used for the calculations. However, the real part does not change over this wavelength range and the imaginary part decreases with increasing wavelength suggesting that the material alone is brighter at longer wavelengths and should have a red color. However, we can see that due to the small size of the constituents the color of the scattering from these aggregates has a blue color and dominates the color of the material. Note that the color and polarimetric color for the X2/X3 model are very similar to those for the constituents of the X2/X3 model.

Scattering Matrices for Cubes

The larger cube shows a narrower forward scattering peak in the intensity (F_{11} element) due to diffraction. Their polarization signatures are also strikingly different with the larger cube showing significant positive polarization with a peak near 60% at a scattering angle near 50° . In both cases the ratio F_{22}/F_{11} is equal to one for all scattering angles. This is due to the fact that the cross-polarization terms, the complex amplitudes A_3 and A_4 in equation (2.8), were not measured because a cube in random orientation should possess no cross polarization terms in view of the symmetry arguments presented in the Scattering Matrix section earlier in this chapter. Also for this reason, both cubes show that the elements F_{33} and F_{44} are equal. Another significant difference in the scattering patterns of these two cubes is that the pattern for the smaller cube has a more rippled structure. This is due to the fact that the size of this cube (with a size parameter near 13) is firmly in the intermediate size range where interference phenomena take place. In other words it is much larger than something in the Rayleigh regime and yet significantly smaller than could be approximated with geometrical optics. The rippling structure still exists in the single orientations for the larger cube (c.f. Figure 2.14) but since the ripples are closer together they merge into a smoother curve as averages over orientation are performed. The ratio F_{34}/F_{11} also shows a difference between the two cube sizes. The larger cube's curve is mostly flat but the smaller cube has a curve with generally negative values and a minimum at a scattering angle slightly larger than 90° .

For the smaller cube, it is feasible to use the DDA to calculate the scattering characteristics averaged over orientation. This is shown in Figure 2.19. The agreement is good considering that neither the lab results nor the calculations are a perfect

simulation of an average over random orientations and do not use the same orientations to calculate the average. The laboratory data is averaged over 124 orientations whereas I was able to use 630 in the DDA calculations. This accounts for any discrepancies between DDA and laboratory results in both intensity and polarization. The lab measurements (including 85 frequencies) took about 40 days whereas the calculations for a single frequency take approximately 3 days of computing time. Thus to get the same information from the calculations regarding trends in frequency would take close to nine months.

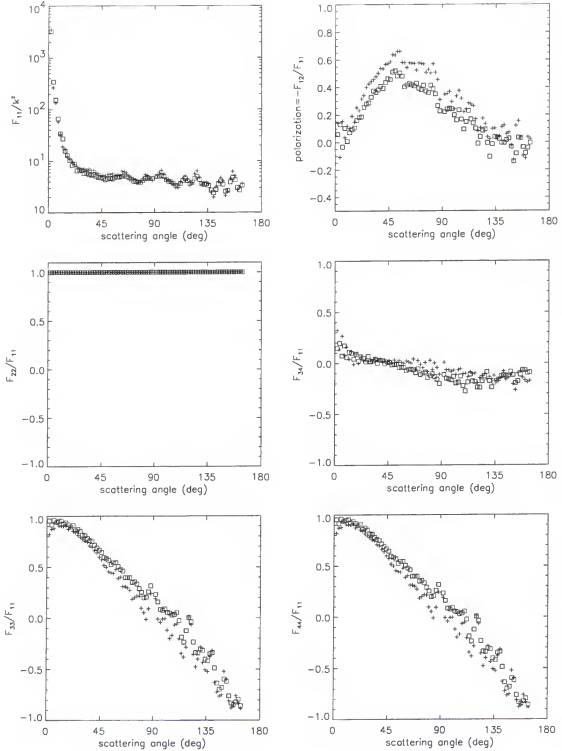


Figure 2.17 Angular distribution of the F-matrix elements for the 1.5'' cube. F_{11}/k^2 (intensity), $-F_{12}/F_{11}$ (polarization), and F_{22} , F_{33} , F_{44} , and F_{34} all normalized by F_{11} are calculated from measured scattering amplitudes. Crosses and squares represent the blue and red wavebands, respectively.

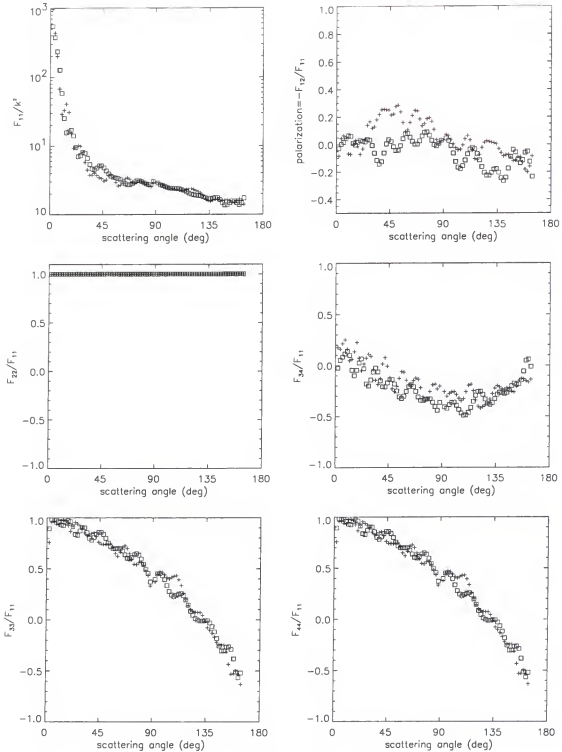


Figure 2.18 Angular distribution of the F-matrix elements for the 0.5'' cube. F_{11}/k^2 (intensity), $-F_{12}/F_{11}$ (polarization), and F_{22} , F_{33} , F_{44} , and F_{34} all normalized by F_{11} are calculated from measured scattering amplitudes for the 0.5'' cube. Crosses and squares represent the blue and red wavebands, respectively.

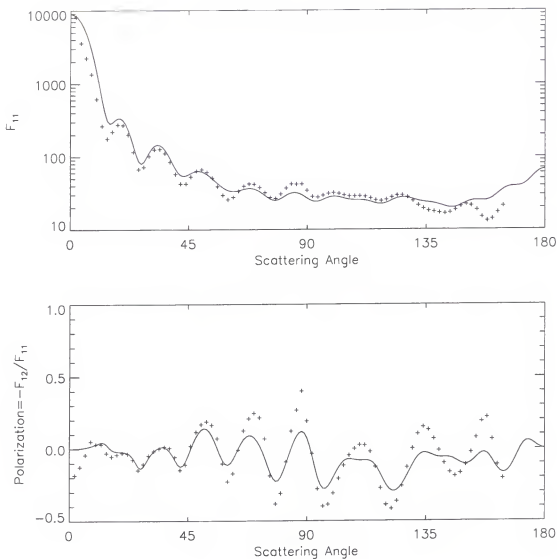


Figure 2.19 DDA calculations and microwave laboratory data for 0.5'' cube. The results are for an average over orientation. The laboratory data is shown with + symbols and the DDA calculations with the solid lines. This data is for a single frequency of 75 GHz.

Scattering Matrices for Aggregates

Comparing the results for the CYA and the BSA (Figure 2.21 and Figure 2.22) shows that the shape of the constituent particles (at least in this size range) is

inconsequential to the scattering patterns produced by the aggregate because these aggregates are otherwise similar (in material and overall number of constituents). The small differences seen between Figure 2.21 and Figure 2.22 are due the fact that data reported for the CYA are averaged over three times as many orientations as the data for the BSA. The most notable difference is seen in the polarization curves. The BSA polarization shows significantly more structure than the CYA curve. If one considers an average over the same number of orientations for the CYA, its polarization curve also shows similar structure. In the radiative transfer studies in chapter 4 we need only consider one of these aggregates. We will use the CYA due to the fact that more orientations were measured for this target.

The LSA has the highest polarization as might be expected due the fact that it has the smallest constituents and it is the only aggregate measured with constituents that have a size parameter below one. The SA shows higher polarization (in the red) than the CYA which is made of the same material except in pieces. The lower density of the SA as compared to the CYA allows more of a polarization signature from the constituents to show through in the aggregates scattering pattern. It only shows through in the red because here the constituents are smaller with respect to the wavelength and are actually near one in size parameter whereas in the blue wavelengths the constituents appear larger and thus have less polarization at 90° scattering angle.

Similar generalizations about the other elements of the scattering matrix can also be drawn from these data, however, a more systematic survey of aggregate types would be useful to confirm such conclusions. The ratios F_{33}/F_{11} and F_{44}/F_{11} all show a trend from positive to negative values with increasing scattering angle. The scattering angle at

which this transition occurs, however, varies based on refractive index and size of the constituents. Small particles transition at 90° scattering angle and show a maximum of one in forward scattering and a minimum on negative one in backscattering. Weakly absorbing larger aggregates with larger constituents transition at higher scattering angles and have a minimum that is significantly larger than negative one (c.f. Figure 2.21 through Figure 2.23 for the CYA, BSA, and SA). In some cases the transition to negative values does not occur and the minimum is in fact positive (e.g. Figure 2.23). More absorbing aggregates (LSA, OA, and CA) do not show the same shift in the transition angle but the minimum does seem to increase with increasing size of the constituents. Color effects can also be seen, most notably in the less absorbing targets (the CYA, BSA, and the SA), in the sense that the red and blue curves are visibly separated.

The ratio F_{22}/F_{11} is identically equal to one when no cross-polarization is present (e.g. the case of a sphere). Thus, it is expected that the ratio F_{22}/F_{11} deviates from one for the aggregates. At forward scattering angles, the ratio is one for all of the targets measured. This is due to the fact that at forward scattering angles, diffraction dominates as the primary scattering phenomena and it is in fact insensitive to polarization. The point at which the ratio begins to deviate from one and the magnitude of the deviation is an indication of how much linear cross-polarization the target introduces in the process of scattering light. This is linked to the refractive index of the material as well as the structure of the aggregate. Notice that the more absorbing targets show a smaller deviation. A physical explanation for this is that the absorbing nature of the target acts to damp out the cross-polarization terms. It is also interesting to recognize that the aggregate X2-X4 is small enough that it does not possess significant cross-polarization

and its ratio is one for all scattering angles. The wavelength for the X1 calculation is small enough (compared to the size of the aggregate) that this aggregate is large enough to show significant cross-polarization.

Most of the aggregates have F_{34}/F_{11} curves that are fairly flat and hover near zero. Notable exceptions to this are the CYA, BSA and SA which show slightly positive blue values and significantly negative red values for this ratio in the forward and intermediate scattering directions (c.f. Figure 2.21 and Figure 2.22). The F_{34} element is an indication of the transformation of circularly polarized radiation to that polarized linearly at $\pm 45^\circ$ to the scattering plane during the scattering process (and vice versa for F_{43} which is equal but opposite to F_{34} for macroscopically isotropic and symmetric media).

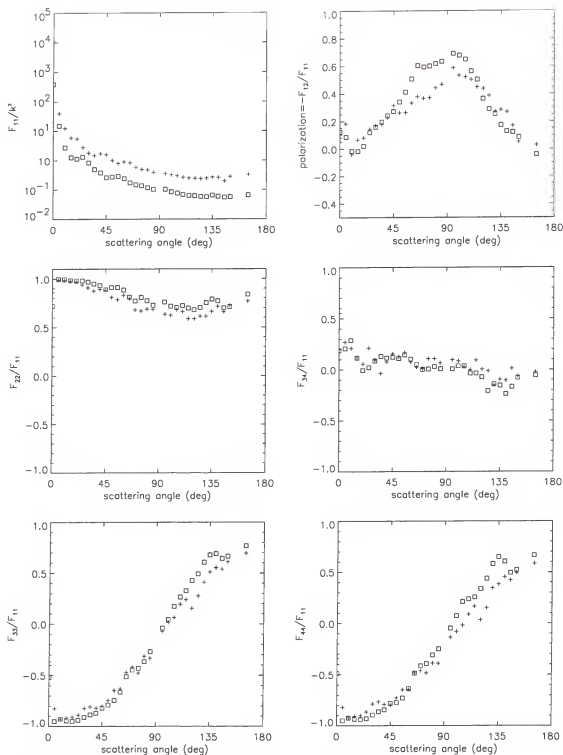


Figure 2.20 Angular distribution of the F-matrix elements for the LSA. F_{11}/k^2 (intensity), $-F_{12}/F_{11}$ (polarization), and F_{22} , F_{33} , F_{44} , and F_{34} all normalized by F_{11} are calculated from measured scattering amplitudes. Crosses and squares represent the blue and red wavebands, respectively.

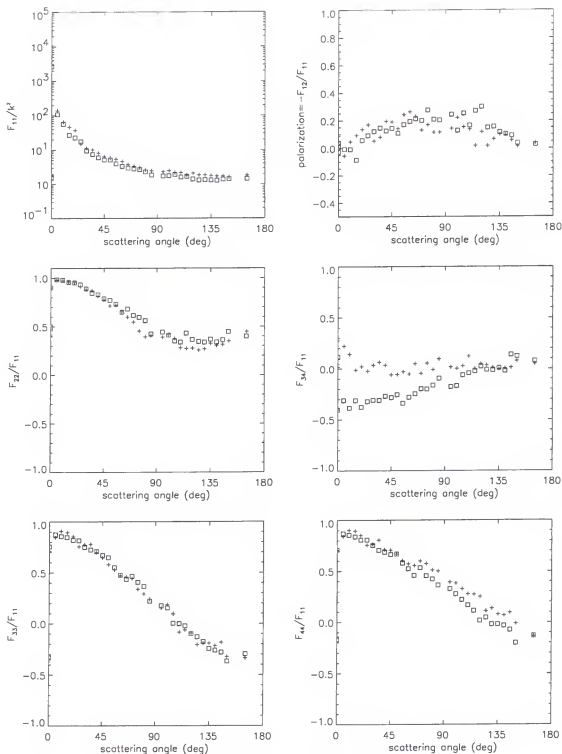


Figure 2.21 Angular distribution of the F-matrix elements for the CYA. F_{11}/k^2 (intensity), $-F_{12}/F_{11}$ (polarization), and F_{22} , F_{33} , F_{44} , and F_{34} , all normalized by F_{11} , are calculated from measured scattering amplitudes. Crosses and squares represent the blue and red wavebands, respectively.

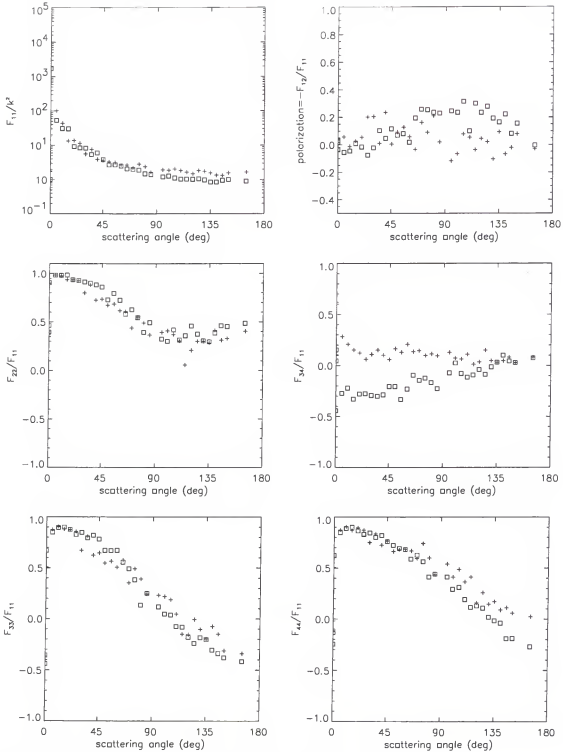


Figure 2.22 Angular distribution of the F-matrix elements for the BSA. F_{11}/k^2 (intensity), $-F_{12}/F_{11}$ (polarization), and F_{22} , F_{33} , F_{44} , and F_{34} , all normalized by F_{11} , are calculated from measured scattering amplitudes. Crosses and squares represent the blue and red wavebands, respectively.

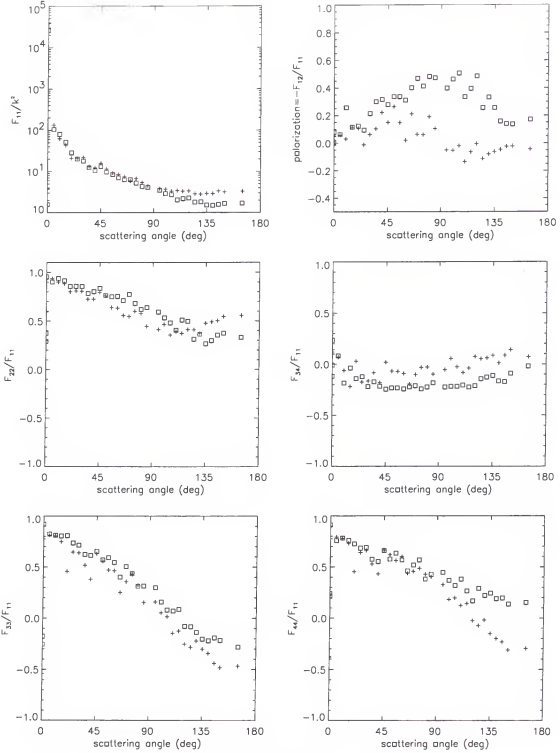


Figure 2.23 Angular distribution of the F-matrix elements for the SA. F_{11}/k^2 (intensity), $-F_{12}/F_{11}$ (polarization), and F_{22} , F_{33} , F_{44} , and F_{34} , all normalized by F_{11} , are calculated from measured scattering amplitudes. Crosses and squares represent the blue and red wavebands, respectively.

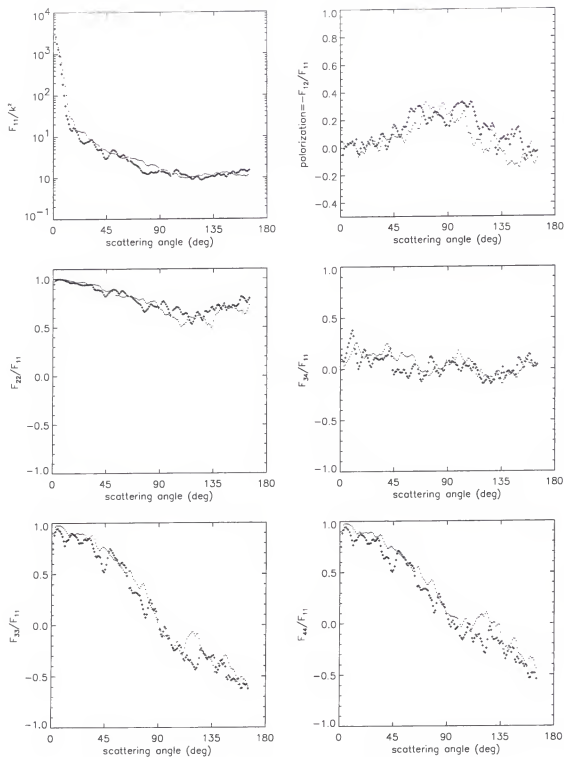


Figure 2.24 Angular distribution of the F-matrix elements for the OA. F_{11}/k^2 (intensity), $-F_{12}/F_{11}$ (polarization), and F_{22} , F_{33} , F_{44} , and F_{34} , all normalized by F_{11} , are calculated from measured scattering amplitudes. Crosses and dots represent the blue and red wavebands, respectively.

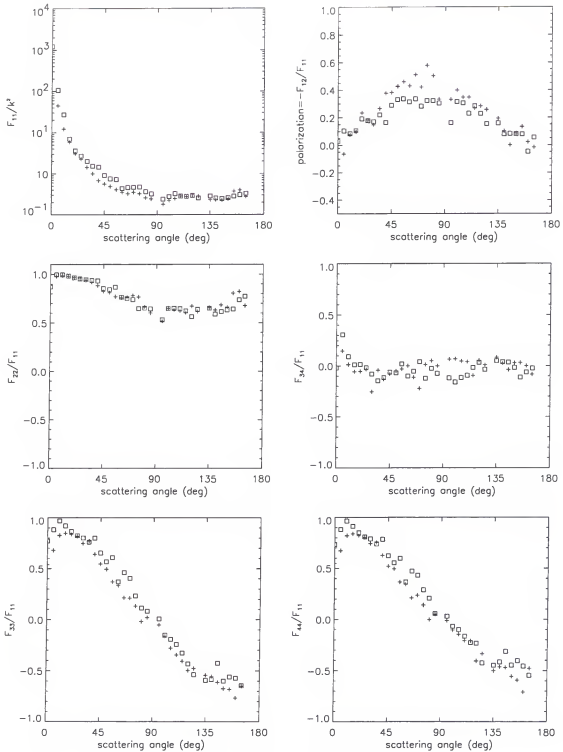


Figure 2.25 Angular distribution of the F-matrix elements for the CA. F_{11}/k^2 (intensity), $-F_{12}/F_{11}$ (polarization), and F_{22} , F_{33} , F_{44} , and F_{34} , all normalized by F_{11} , are calculated from measured scattering amplitudes. Crosses and squares represent the blue and red wavebands, respectively.

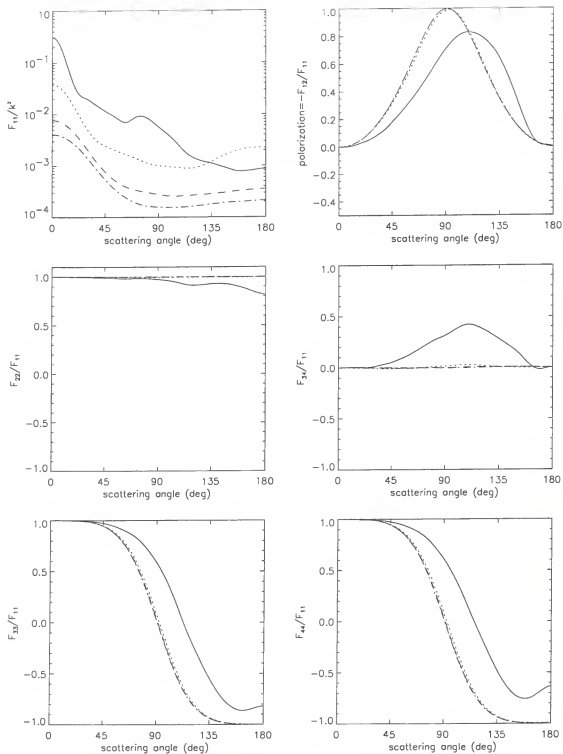


Figure 2.26 Angular distribution of the F-matrix elements for aggregates X1-X4. F_{11}/k^2 (intensity), $-F_{12}/F_{11}$ (polarization), and F_{22} , F_{33} , F_{44} , and F_{34} , all normalized by F_{11} , calculated by Yu-Lin Xu. Solid line, dotted line, dashed line, and dash-dot line, are the wavelengths 264 nm, 452 nm, 648 nm, and 750 nm, and thus the aggregates X1, X2, X3, and X4 respectively.

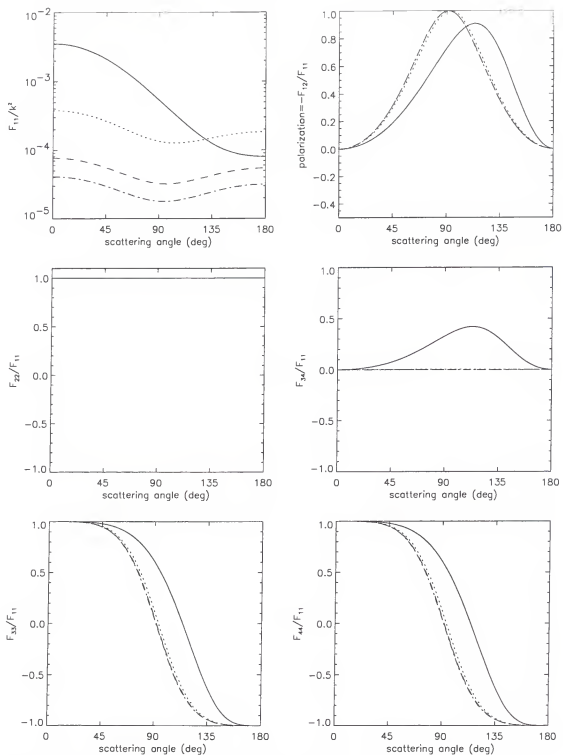


Figure 2.27 Angular distribution of the F-matrix elements for the X1-X4 constituents. F_{11}/k^2 (intensity), $-F_{12}/F_{11}$ (polarization), and F_{22} , F_{33} , F_{44} , and F_{34} , all normalized by F_{11} , calculated using Mie theory. Solid line, dotted line, dashed line, and dash-dot line, are the wavelengths 264 nm, 452 nm, 648 nm, and 750 nm, and thus the constituents from aggregates X1, X2, X3, and X4 respectively.

Single Scattering and Titan

Several methods have been used by various authors in order to gain some insight to the single scattering characteristics of Titan's aerosols directly from observational data. Tomasko and Smith (1982) and West *et al.* (1983) developed constraints on the single scattering intensity, polarization, and single scattering albedo by comparing the observations with radiative transfer calculations using synthetic phase matrices. They made some simplifying assumptions to reduce the number of phase matrix elements used in the multiple scattering calculations. First they note that for particles that are small with respect to wavelength, the element b_2 in equation (2.11) is very small and can be neglected. And if circular polarization is unimportant, a_4 can also be neglected. Secondly, for spheres a_3 is nearly equal to a_1 and a_2 which are equal to each other. Thus, the 6 independent elements in equation (2.11) are reduced to two, a_1 and b_1 . The values of these elements used for input to the radiative transfer models are parameterized by a double Henyey-Greenstein function (hereafter abbreviated by H-G) in the case of a_1 and then b_1 is determined by allowing the polarization ($-b_1/a_1$) to be given by the Rayleigh scattering value times a constant, C .

A double H-G function, equation (2.19), is given by two single H-G functions, equation (2.20), and a parameter, f , which represents the relative weights given to the individual H-G functions.

$$a_1(g_1, g_2, f, \theta) = fHG(g_1, \theta) + (1 - f)HG(g_2, \theta) \quad (2.19)$$

$$HG(g, \theta) = \frac{1 - g^2}{(1 + g^2 - 2g \cos \theta)^{3/2}} \quad (2.20)$$

Thus, given a_1 from equation (2.19), b_1 is then determined by Rayleigh scattering.

$$\frac{-b_1}{a_1} = C \frac{1 - \cos^2 \theta}{1 + \cos^2 \theta} \quad (2.21)$$

The values for the three parameters, g_1 , g_2 , and f , which best matched the Pioneer 11 and Voyager 2 photopolarimetry are given in Table 2.6 along with the Rayleigh scattering multiplicative constant, C . These functions are also shown in Figure 2.28 in order to compare them with the single scattering characteristics of the targets measured in the lab and calculated. Note that $HG(g, \theta)/k^2$, where k is the wavenumber, is plotted to be consistent with single scattering results presented above.

Table 2.6 Photopolarimetry best fit H-G function parameters

wavelength (nm)	g_1	g_2	f	a	C
264	0.70	-0.35	0.933	0.52	0.75
452	0.70	-0.35	0.933	0.791	0.93
648	0.60	-0.60	0.90	0.915	0.95
750	0.60	-0.60	0.90	0.85	0.78

Note: a is the single scattering albedo and C is the Rayleigh scattering multiplicative constant.

Given that the synthetic H-G phase function and polarization in Figure 2.28 provide reasonable fits to the spacecraft Photopolarimetry (c.f. Figure 1.1), one would expect that the actual particles in the Titanian atmosphere should have phase functions and polarization which match those in Figure 2.28. Of the targets discussed in previous sections, only the X1-X4 calculations and the LSA measurements come close to matching the polarization. Based on this comparison we might expect that these two models have the best chance of matching the Titan photopolarimetry when radiative

transfer is considered. The X1-X4 models have too much polarization at 90° scattering angle and the LSA does not have enough to match the polarization in Figure 2.28. The single scattering polarimetric color does not show a single trend with wavelength. It appears that two different sets of Rayleigh scattering multiplicative constants are determined; one set with lower values for the Voyager 2 (264 and 750 nm) data and another set with higher values for the Pioneer 11 (452 and 648 nm) data. This may be an indication of an inconsistency within the data sets. If one considers the Pioneer 11 and Voyager 2 data separately then polarimetric color is qualitatively red. For reasons which will be discussed shortly, I do not believe that the H-G phase function presented here is even a reasonable representation for the Titanian aerosols so it is not useful to discuss how any of the targets match it.

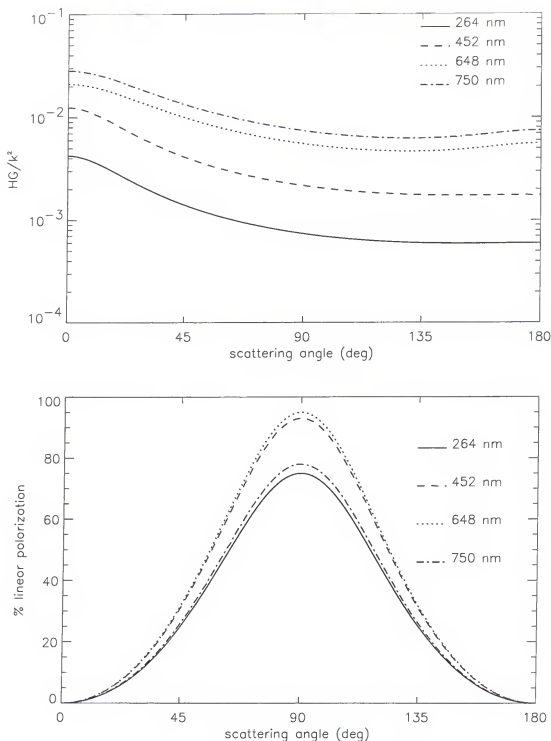


Figure 2.28 Synthetic phase function and polarization fitting Titan photopolarimetry. Best fit H-G functions, a_1 , and constants times the Rayleigh polarization function, $-b_1/a_1$, as found for Pioneer 11 (Tomasko and Smith 1982) and Voyager 2 (West *et al.* 1983).

High phase angle images of Titan were taken by both of the Voyager 1 and Voyager 2 spacecraft using the violet (420 nm) and green (560 nm) filters. The Voyager 1 violet images were analyzed to produce values for the ratio of intensities at two different phase angles ($\alpha=160^\circ$ and $\alpha=129^\circ$ corresponding to $\Theta=20^\circ$ and $\Theta=51^\circ$), denoted as R_{ms} because multiple scattering must be accounted for in understanding this ratio (Rages *et al.* 1983). Because the images contain Titan's resolved disk rather than photometry which produces single disk integrated values for the brightness of the entire disk, Rages *et al.* (1983) choose to represent each image with the maximum value of the reflected intensity along a radial scan perpendicular to the limb towards the center of the disk. They claim that the shape of the intensity curve interior to the maximum of the scan is independent of the single scattering properties of the scatterers and instead dependent on the atmosphere's departure from plane parallel geometry.

They found $R_{ms} = 5.2 \pm 0.7$ which would obviously exclude a purely Rayleigh atmosphere with $R_{ms} = 1.5$ as can be determined from a figure similar to Figure 3.10. Using a synthetic phase function similar to that in equation (2.19) but using a Rayleigh phase function in place of the second H-G function, they fit the observed R_{ms} , geometric albedo, and absolute intensity in order to determine the value of the ratio for the single scattering phase function, R_{ss} . They found $R_{ss} = 7.2 \pm 1.0$ for single scattering albedo, $a = 0.71$. This can then be compared to the experimentally determined R_{ss} (Table 2.7) for all the targets and R_{ss} for Rayleigh scattering which is 1.35. Rages *et al.* (1983) found that for small particles (those with volume equivalent size parameters less than approximately three) R_{ss} increases from a minimum at the Rayleigh limit. Below this volume equivalent size parameter of three, R_{ss} does not appear to depend strongly on the

shape or index of refraction of the particle and it can be fairly well approximated by diffraction alone (see Figure 3 in Rages *et al.* 1983). But beyond this region, R_{ss} appears to oscillate and depend on both the shape and the index of refraction. This is confirmed for larger particles (their study did not include any particles with equivalent volume size parameters larger than seven) by the values in Table 2.7. The physical reason for this is that the diffraction peak is broader for smaller particles than for larger particles so that it extends out into the region between scattering angles 20° and 50° . But as the particles become larger and are in what is called the resonance region, ripples in the scattering pattern from interference phenomena cause oscillations in R_{ss} .

The H-G synthetic phase functions shown above in Figure 2.28 do not have the appropriate forward scattering properties needed to match the high phase angle images. The R_{ss} values for these cases are 2.22 in the blue and 1.85 in the red. These are significantly too low, a fact that was not considered by either West *et al.* (1983) or Tomasko and Smith (1982) who originally proposed these synthetic phase functions.

This analysis does have a few problems and thus should only be used as a guide in choosing models which might be appropriate for Titan. Their estimate of R_{ss} is dependent on its relationship to the single scattering albedo which in turn is dependent on the geometric albedo. The value they used for the geometric albedo may have been overestimated at the wavelength of 420 nm at which they were working (Lemmon 1994). Also R_{ss} is not determined with a model using true spherical geometry but rather using a correction (based on a single comparison to the case of exponential extinction in a spherical atmosphere) to the plane parallel case. Due to long slant optical paths at large phase angles, their analysis only applies to the top few tenths of optical depth. This

explains why I will not be showing comparisons between R_{ms} and radiative transfer model results. As discussed in the next chapter, the plane parallel approximation used in the radiative transfer calculations is not valid at high phase angles especially when the aerosols are highly forward scattering in nature (Kattawar *et al.* 1971).

Table 2.7 R_{ss} values for all targets.

Target	Red R_{ss}		Blue R_{ss}	
CYA	4.5		6.4	
BSA	3.4		4.2	
LSA	4.0		6.0	
SA	3.1		1.9	
CA	4.7		6.4	
OA	3.7		2.7	
1.5" cube	1.8		1.8	
0.5" cube	3.7		2.4	
	750 nm	648 nm	452 nm	264 nm
X1-X4	6.4	7.2	5.9	3.3
X1-X4 constituents	1.4	1.4	1.5	1.7

Finally, other pieces of evidence not considered explicitly by other studies of Titan's aerosols are color and polarimetric color. Titan shows blue polarimetric color and red color. According to Table 2.5, the targets which also show these qualitative trends are the OA and the CA (those with fairly large imaginary indices of refraction). However, multiple scattering effects can make the color characteristics of an atmosphere different from the particle single scattering color characteristics. This issue will be explored more in Chapter 4. For example., X1-X4 show red polarimetric single scattering color and blue single scattering color (which is opposite to Titan's overall trend). When this is compared with the multiple scattering results in Chapter 4 (Figure 4.11 for polarimetric color and Table 4.3 for color), we can see that this type of particle

produces blue polarimetric multiple scattering color if the UV wavelength is disregarded and red multiple scattering color which in fact does qualitatively match Titan.

Having examined the single scattering properties of the targets in this study in the context of what we know about the single scattering properties of Titan's aerosols, we are now ready to pursue radiative transfer calculations for atmospheres made up of these targets. Next we will discuss the development of the radiative transfer model used to provide the results in Chapter 4.

CHAPTER 3

POLARIZED RADIATIVE TRANSFER MODELING

In order to compare microwave laboratory results with observations of Titan it is necessary to simulate model atmospheres made up of particles with scattering properties known from microwave measurements using radiative transfer theory. The radiation received by a spacecraft observing Titan is a combination of radiation that has been redistributed by the atmosphere in a few different ways. The solar radiation incident on the atmosphere of Titan is subject to absorption and scattering processes inside the atmosphere before it makes its way to the detectors of the spacecraft. The mathematical representation of these processes is called the radiative transfer equation and it is essentially a sum of the sources and sinks for radiation inside the atmosphere.

There are many resources, with emphasis on many different disciplines (astronomy, atmospheric science, and neutron transport to name a few), which derive a variety of different solutions to the radiative transfer problem (Chandrasekhar 1960; Hansen and Travis 1974; Irvine 1975; Sobolev 1975; Liou 1980; van de Hulst 1980; Hovenier and van der Mee 1983; Lenoble 1985; Liou 1992). There are many inconsistencies in notation among these references. So I will outline the problem I wish to solve and its solution while attempting to use a consistent set of notations chosen on the basis of their conformity to the conventions in the above works as well as their ability

to be compatible with the notation used previously in discussions of the physics of single scattering by particles.

This chapter begins with some basic definitions and assumptions needed to derive the radiative transfer equation. Next we discuss the method of solution to this equation chosen for this work. Then a method for integration over the planetary disk is developed. Finally, the implementation is tested and sensitivity studies are performed.

Basic Definitions and Radiometric Quantities

The quantity we will be most concerned with in this chapter is intensity in the form of the Stokes vector and so a definition and clarification is in order. It is customarily referred to as confined within a pencil of radiation as shown in Figure 3.1. The quantity called monochromatic specific intensity by astronomers, also known by international convention as spectral radiance (Illuminating Engineering Society of North America 1996), is the energy transported across an element of area ($d\sigma$), enclosed within an element of solid angle ($d\Omega$) oriented at an angle (η) with respect to the outward normal to the element of area, within a time interval (dt) and a wavelength interval ($d\lambda$).

$$I_{\lambda} = \frac{dE_{\lambda}}{\cos \eta d\sigma d\Omega dt d\lambda} \quad (3.1)$$

It has units of energy per unit area per unit solid angle per unit time per unit wavelength interval. Based on this, we can define the net flux (a monochromatic quantity), also called irradiance or illuminance (when speaking about incident flux) and luminous exitance (when speaking about emergent flux), as the radiant energy per unit time and

wavelength interval flowing in all directions or the integral of the intensity over all solid angles. It has units of energy per unit area per unit time per unit wavelength interval.

$$F_{\lambda} = \int_{\Omega} I_{\lambda} \cos \eta d\Omega \quad (3.2)$$

From this point, I will drop the wavelength designation and the monochromatic modifier for simplicity of notation but it is nonetheless implied throughout.

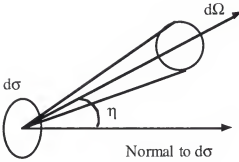


Figure 3.1 Pencil of Radiation

For a complete treatment of radiation in a situation involving scattering as seen in Chapter 2, it is necessary to include the state of polarization and consider the vectorial nature of electromagnetic radiation. Stokes parameters are a convenient representation of polarized light. From this point on we will use vector notation (bold text representing vectors or matrices) to represent Stokes vectors as, $\mathbf{I}^T = (I \quad Q \quad U \quad V)$. The quantities we are most interested in are I, Q, and U dealing only with linear polarization. Circular polarization has been found to be small in other planetary atmospheres (e.g. on the order of 0.1% for Saturn (Smith and Wolstencroft 1983)) but has not been measured for Titan.

Now, it is necessary to specify the coordinate system in which we will be working (see Figure 3.2). The directions of incidence and emergence are designated by their

zenith and azimuth angles. There exist two systems for the definition of these angles which apply to different situations that are often confusingly employed interchangeably. When considering internal radiation (system I), the zenith angle, θ' , is measured from the downward normal and its cosine is denoted as, u , so that u is positive for downwelling radiation and negative for upwelling radiation. For radiation outside an atmosphere or slab (system II), it is customary to use the outward normal as the zenith angle reference direction. In this case, its cosine is denoted as μ and it is always positive. In some references, most notably Chandrasekhar (1960) who uses the symbol μ independent of internal or external radiation, the convention in system I is reversed, using the outward normal as the reference. Note that small case θ is used for zenith angle throughout as compared to upper case Θ which represents scattering angle. The azimuth angle, ϕ , is measured counterclockwise when looking down into the atmosphere. For brevity, each direction will be denoted as Ω which represents an ordered pair of zenith and azimuth directions.

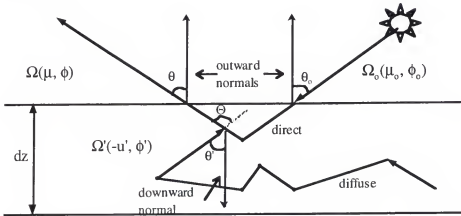


Figure 3.2 Local plane parallel coordinate system

A Model Appropriate for Titan

In the "Standard Problem", isotropic radiation impinges on a plane parallel homogeneous atmosphere, which may contain isotropic embedded sources, and polarization is neglected (van de Hulst 1980). A plane parallel atmosphere is a good approximation to a spherical atmosphere if the thickness is much smaller than the radius of curvature of the planet (Irvine 1975). To this Standard Problem we need to add two complications and make two simplifications in order to have a model appropriate for use with Titan. First, we need to include polarization so we need intensity represented as vector (the Stokes vector) and the phase function which describes the angular distribution of scattered light represented as the 4×4 phase matrix. Next, we need to consider a non-homogenous atmosphere with scattering properties that vary with depth. Also we will simplify the incident intensity to unidirectional incidence (e.g. solar incidence from direction Ω_0) and we do not need any embedded sources. This would only be necessary if one wanted to consider thermal wavelengths in the atmosphere of Titan.

Aside from the premise above, it is necessary to explicitly state some basic assumptions in order for the above expressions to be valid. The atmospheric properties of each plane parallel layer do not vary horizontally. There is no time dependence and no communication between different wavelengths (e.g. fluorescence). The incident beam is an infinite plane wave like that made in the far-field from a point source according to Huygen's principle. And lastly, particles must scatter light independently (as defined in Chapter 2 in the section Scattering Matrix). Now that we have spelled out the conditions and definitions under which we are working, we are ready to develop the transfer equation.

The Vector Transfer Equation

Consider that an atmosphere is illuminated from the top by the solar flux, πF_0 normal to itself (meaning that we are describing the energy crossing a unit area perpendicular to the direction of propagation in a unit time). The mathematical description of the removal of intensity by extinction (absorption and scattering) due to the atmosphere can be written as follows:

$$dI(z, \Omega) = -\sigma_e I(z, \Omega) dz / \cos \theta \quad (3.3)$$

where, σ_e is the mean extinction cross-section of a sample of N particles per unit volume, dz is the thickness, and θ is the zenith angle. We can simplify equation (3.3) by employing the concept of normal optical depth, τ , and assigning $u = \cos \theta$.

$$\tau = \int_z^{\infty} \sigma_e N dz, \quad d\tau = -\sigma_e N dz \quad (3.4)$$

Thus, we have

$$dI(\tau, \Omega) = I(\tau, \Omega) d\tau / u \quad (3.5)$$

Now we must consider the addition to the beam by multiple scattering into our direction of consideration, $d\Omega$, from all other directions $d\Omega'$. This can be written as

$$dI(\tau, \Omega) = -\frac{\sigma_s N}{4\pi} \frac{d\tau}{u} \int_{\Omega} I(\tau, \Omega') \mathbf{P}(\tau, \Omega') d\Omega' \quad (3.6)$$

where σ_s is the scattering cross section of a sample of N particles per unit volume, and \mathbf{P} is called the phase matrix which is related to the scattering matrix, \mathbf{F} , through a rotation that is discussed in detail later. The choice of nomenclature here is unfortunate because the phase matrix has nothing to do with the phase of the radiation waves involved. Its use derives from the term phase function describing how scalar intensity varies with phase

angle (the complement to the scattering angle). The phase matrix is dimensionless and represents the angular distribution of scattered light so the integral above accounts for all the possible scattering directions within 4π solid angle. This leads to the following normalization condition

$$\frac{1}{4\pi} \int_{4\pi} \mathbf{P}_{i,l} d\Omega = 1 \quad (3.7)$$

The third and final term needed for the transfer equation comes from the single scattering of the direct solar incident beam.

$$d\mathbf{I}(\tau, \Omega) = -\mathbf{F}(\tau) \frac{\mathbf{P}(\Omega, \Omega_o) \sigma_s d\tau}{4\pi u}, \text{ where } \mathbf{F}(\tau) = \pi \mathbf{F}_o \exp\left(\frac{\tau}{\mu_o}\right) \quad (3.8)$$

The sinks and sources in equations (3.3), (3.6), and (3.8) can be combined to give the vector integro-differential transfer equation.

$$u \frac{d\mathbf{I}(\tau, \Omega)}{d\tau} = \mathbf{I}(\tau, \Omega) - \mathbf{J}(\tau, \Omega), \text{ where} \quad (3.9)$$

$$\mathbf{J}(\tau, \Omega) = \frac{a}{4\pi} \left[\int_{\Omega} \mathbf{I}(\tau, \Omega') \mathbf{P}(\tau, \Omega; \Omega') d\Omega' + \pi \mathbf{F}_o \mathbf{P}(\tau, \Omega; \Omega_o) e^{-\tau/\mu_o} \right]$$

\mathbf{J} is called the source function and is the sum of the direct and diffuse sources of radiation. The second term includes the sink due to extinction. The single scattering albedo, a , is the ratio of the single scattering cross-section to the extinction cross-section, $a = \sigma_s / \sigma_e$, and represents the fraction of extinction caused by scattering as opposed to absorption. Before we discuss the method of solution for this equation in the section entitled Doubling and Adding Method we need to develop the concept of the phase matrix.

The Phase Matrix

The phase matrix, \mathbf{P} , is related to the scattering matrix through a set of two rotations. Remember that the scattering matrix is a function of scattering angle, Θ . The phase matrix, as seen above, is a function of direction in the atmosphere, $\Omega(u, \phi)$. Using spherical geometry, we can express the scattering angle in terms of the zenith and azimuth angles of the incident and scattered beams (c.f. Figure 3.3) in the following way

$$\cos \Theta = \cos \theta \cos \theta' + \sin \theta \sin \theta' \cos(\phi' - \phi) = uu' + \sqrt{1-u^2} \sqrt{1-u'^2} \cos(\phi' - \phi). \quad (3.10)$$

Intensities, represented by Stokes vectors, are always taken with respect to a reference plane. The rotation matrix for an arbitrary Stokes vector, $\mathbf{L}(i)$, derives from the rotation of the parallel component of the electric field denoted by, θ' , through an arbitrary angle, i , which is positive for counterclockwise rotation when looking in the direction of propagation. In Figure 3.3, the incident reference plane contains P_1ON , the reference plane for the scattered radiation contains P_2ON , and the scattering plane contains P_1OP_2 . Thus, the intensity vector, \mathbf{I} , must be rotated through angle $\pi - i_1$ into the scattering plane and then again by $-i_2$. The rotation can be written as pre and post multiplication of the scattering matrix, $\mathbf{F}(\Theta)$, by a rotation matrix.

$$\mathbf{P}(u, \phi; u', \phi') = \mathbf{L}(-i_2) \mathbf{F}(\Theta) \mathbf{L}(\pi - i_1), \text{ where } \mathbf{L}(i) = \begin{pmatrix} 1 & 0 & 0 & 0 \\ 0 & \cos 2i & \sin 2i & 0 \\ 0 & -\sin 2i & \cos 2i & 0 \\ 0 & 0 & 0 & 1 \end{pmatrix} \quad (3.11)$$

In some references (e.g. Liou 1980), the direction of the parallel component of the electric field, θ' , is reversed leading to the following rotation $\mathbf{L}(\pi - i_2) \mathbf{F}(\Theta) \mathbf{L}(-i_1)$. However, $\mathbf{L}(\pi - i)$ is equivalent to $\mathbf{L}(i)$ based on the trigonometric angle addition rule, so the end

$$\mathbf{P}(u, u', \phi' - \phi) = \begin{pmatrix} a_1 & b_1 C_1 & b_1 S_1 & 0 \\ b_1 C_2 & a_2 C_1 C_2 - a_3 S_1 S_2 & a_2 S_1 C_2 + a_3 C_1 S_2 & b_2 S_2 \\ -b_1 S_2 & -a_2 C_1 S_2 - a_3 S_1 C_2 & -a_2 S_1 S_2 + a_3 C_1 C_2 & b_2 C_2 \\ 0 & b_2 S_1 & -b_2 C_1 & a_4 \end{pmatrix}. \quad (3.13)$$

where, $C_1 = \cos 2i_1$, $C_2 = \cos 2i_2$, $S_1 = \sin 2i_1$, and $S_2 = \sin 2i_2$

Note that some authors use **Z** or **M** for this matrix (often they cannot use **P** because they have already used it for the above **F** matrix), but it seems that **P** for phase matrix is logical.

Fourier Series Analysis in Azimuth Angle

Putting **P** back into the transfer equation (3.9) at this point leads to the intractable obstacle of its integration over zenith angle and azimuth angle. If, however, we investigate the four elements in the top left corner and the bottom right corner of equation (3.13), we can see by inspection that all of these are even functions of the azimuth difference, $\phi' - \phi$. Discovering this by inspection does not, however, mean that it is necessarily obvious so I will elucidate the argument briefly. Referring to equation (3.10), we can demonstrate that $\cos \Theta$ is an even function (such that $f(x) = f(-x)$) of $\phi' - \phi$ by examining the case where θ and θ' are held constant. In this case, $\cos \Theta$ is then only a function of $\cos(\phi' - \phi)$ and is obviously an even function since the cosine function is even. By similar reasoning given that $\cos \Theta$ is even and examination of equation (3.12), both $\cos i_1$ and $\cos i_2$ are even and C_1 and C_2 are, therefore even as well. Θ is also even based on the fact that $\Theta = \arccos(\text{constant} \cdot \cos(\phi - \phi'))$ is an even function. Lastly, all of the elements of the scattering matrix, **F**, are even because they are functions only of Θ which is even. An analogous argument shows that the elements in the top right corner and bottom left corner are odd functions of $\phi' - \phi$.

The facts above allow us to express the phase matrix as a Fourier series,

$$\mathbf{P}(u, u', \phi' - \phi) = \mathbf{P}_0^c(u, u') + 2 \sum_{j=1}^{\infty} \left[\mathbf{P}_j^c(u, u') \cos j(\phi' - \phi) + \mathbf{P}_j^s(u, u') \sin j(\phi' - \phi) \right]. \quad (3.14)$$

The c and s superscripts refer to the even and odd sub-matrices defined above. The practicalities of the calculation of the Fourier coefficients will be discussed later in the Implementation section below. The intensity, \mathbf{I} , can also be expanded in the same manner if we make the restriction that the incident, and thus all other intensities, are symmetric with respect to the reference ϕ_0 plane. This restriction is not absolutely necessary but without it the simplification of using either sines or cosines for each component will not work (a combination would be needed). For an isotropic field this is obviously not a hard restriction to make. A unidirectional beam in the reference plane, as one would find for solar incidence, is by definition symmetric because it is zero everywhere outside it. Such a Fourier expansion gives:

$$\mathbf{I}(\tau, \Omega) = \mathbf{I}(\tau, u, \phi) = \mathbf{I}_0^c + 2 \sum_{j=0}^{\infty} \left[\mathbf{I}_j^c(\tau, u) \cos j(\phi - \phi_0) + \mathbf{I}_j^s(\tau, u) \sin j(\phi - \phi_0) \right]. \quad (3.15)$$

This means that each Fourier azimuth term can be calculated separately and then summed after the transfer calculations are completed to account for the integration over azimuth angle. For example, the cosine Fourier azimuth mode (with $m > 0$) looks like this:

$$u \frac{d\mathbf{I}_m^c(\tau, u)}{d\tau} = \mathbf{I}_m^c(\tau, u) - \frac{a}{4\pi} \left[\int_{-1}^1 \mathbf{I}_m^c(\tau, u') \mathbf{P}_m^c(\tau, u; u') du' + \pi \mathbf{F}_o^c \mathbf{P}_m^c(\tau, u; \mu_o) e^{-\tau/\mu_o} \right]. \quad (3.16)$$

For illustrative purposes, we examine the form of the phase matrix when \mathbf{F} is in the form of equation (2.9). \mathbf{P} then has the following form instead of that found in equation (3.13):

$$\begin{pmatrix} a_1 & b_1 C_1 - b_3 S_1 & b_3 C_1 - b_1 S_1 & b_5 \\ b_1 C_2 - b_3 S_2 & a_2 C_1 C_2 - a_3 S_1 S_2 - b_4 (C_1 S_2 - S_1 C_2) & a_2 C_1 S_2 + a_3 S_1 C_2 + b_4 (C_1 C_2 - S_1 S_2) & b_6 C_2 + b_2 S_2 \\ b_1 S_2 - b_3 C_2 & -a_2 C_1 S_2 - a_3 S_1 C_2 - b_4 (C_1 C_2 - S_1 S_2) & a_3 C_1 C_2 - a_2 S_1 S_2 - b_4 (C_1 S_2 + S_1 C_2) & b_2 C_2 - b_6 S_2 \\ b_3 & b_2 S_1 + b_6 C_1 & b_6 S_1 - b_2 C_1 & a_4 \end{pmatrix}. \quad (3.17)$$

The Fourier decomposition of this phase matrix is, as yet, unsolved due to the combinations of odd and even functions within the 2x2 sub-matrices in the four corners. Thus, radiative transfer solutions employing Fourier decomposition are not yet able to handle problems with more complicated scattering matrices like that one would find for specifically oriented or aligned particles.

Expansion of the scattering matrix

We need to work out one more detail in order to computationally manage the rotation of the local scattering matrix with respect to the planes of reference and thus express the phase matrix as a Fourier series in azimuth. A problem comes in when we consider that fact that we have measured $\mathbf{F}(\Theta)$ at a discrete set of scattering angles which are almost certainly not (based on equation (3.10)) the same angles which one would need to calculate $\mathbf{P}(u, u', \phi' - \phi)$ for a given set of zenith and azimuth angles. An additional complication comes from our need to express the phase matrix as a Fourier series. The details of this transition will be discussed in the Implementation section.

It has been shown that the scattering matrix can be expanded in series form and that this is a solution to the above problems. There are at least two different bases for such an expansion, the Legendre polynomials and the generalized spherical functions (Gel'fand *et al.* 1963), both of which are orthonormal sets of functions. In fact, the Legendre polynomials are a special case of the generalized spherical functions. The Legendre polynomials have commonly been used to expand the scalar phase function by

many authors (e.g. Chandrasekhar 1960; Sobolev 1975; Lenoble 1985) but it seems that the generalized spherical functions have become popular for the expansion of the phase matrix elements because it is more efficient (Kuscer and Ribaric 1959) and implicitly accounts for the rotation with respect to the reference plane for the Stokes vectors (de Haan *et al.* 1987). Further details and the expansions of the measured scattering matrices are presented in Appendix B.

Doubling and Adding Method

The solution of the transport equation is the subject of many, many publications using a variety of methods. For the sake of brevity and simplicity, I will present only the method of solution chosen for this work, the doubling and adding method. The basic principle behind this method is that the reflection and transmission from two adjacent layers can be calculated by accounting for successive reflections back and forth between the layers if the functions for transmission and reflection are known for each of the layers independently. It was first developed by Stokes (1862) in describing the reflection and transmission of a stack of glass plates and applied to the problem of polarized radiative transfer in planetary atmospheres in 1971 (Hansen ; Hovenier). The doubling method is a special case of the more general adding method in which a finite homogeneous layer is built up from an infinitesimally thin layer by the combination of identical layers until the desired optical depth is reached. In the case of an inhomogeneous atmosphere, divided up into homogeneous sub-layers, the doubling principle is used to find the reflection and transmission properties of each layer and then the adding method (which takes into account the fact the reflection and transmission properties of an inhomogeneous layer are

dependent on the direction of the incoming light) is used to find the characteristics of the entire atmosphere in a succession of additions for each layer.

Reflection and Transmission Matrices

The reflection and transmission properties of each layer are defined by the reflection and transmission matrices. In the discussion of non-polarized radiative transfer they are usually referred to as the reflection and transmission functions. The reflected (I_r) and transmitted (I_t) intensities are related to the reflection and transmission matrices in the following ways:

$$\begin{aligned} I_r(\mu, \phi) &= \frac{1}{\pi} \int_0^{2\pi} \int_0^1 \mathbf{R}(\mu, \mu', \phi' - \phi) \mathbf{I}_o(\mu_o, \phi_o) \mu' d\mu' d\phi' \\ I_t(\mu, \phi) &= \frac{1}{\pi} \int_0^{2\pi} \int_0^1 \mathbf{T}(\mu, \mu', \phi' - \phi) \mathbf{I}_o(\mu_o, \phi_o) \mu' d\mu' d\phi' \end{aligned} \quad (3.18)$$

Inserting the incident radiation, which may be written in the form

$$\mathbf{I}_o(\mu_o, \phi_o) = \delta(\mu' - \mu_o) \delta(\phi' - \phi_o) \pi \mathbf{F}_o, \quad (3.19)$$

into equation (3.18) we can now write the reflected and transmitted intensities as

$$\begin{aligned} I_r(\mu, \phi) &= \mathbf{R}(\mu, \mu_o, \phi - \phi_o) \mu_o \mathbf{F}_o / \pi \\ I_t(\mu, \phi) &= \mathbf{T}(\mu, \mu_o, \phi - \phi_o) \mu_o \mathbf{F}_o / \pi \end{aligned} \quad (3.20)$$

The reflection and transmission of the combination of two layers, and thus eventually the entire atmosphere, are each determined by an infinite series representing the light which has traveled back and forth between the layers as seen in Figure 3.4. The reflection and total transmission (including both the direct and diffuse radiation) functions are \mathbf{R}_1 and \mathbf{T}'_1 for the first layer, and \mathbf{R}_2 and \mathbf{T}'_2 for the second layer. The

symbol T' is used to differentiate between diffuse transmission, already labeled T , and the total transmission which includes the direct component as well.

$$T' = T + e^{-\tau'/\mu'} \quad (3.21)$$

When the transmission in equation (3.21) is associated with the incident beam, τ' is the optical depth of the first layer, τ_1 , and μ' is the incident direction μ_0 . Otherwise, when it is associated with the emergent beam, τ' is the optical depth of the second layer, τ_2 , and μ' is the emergent direction μ . As mentioned above, the reflection and transmission matrices of inhomogeneous layers depend of the direction of incident radiation. This distinction is made using asterisks so that, for example, R_1 is the reflection from layer one in the upward direction and R^*_1 is the reflection downward. The reflection and transmission at the boundary between the layers is represented by U (up) and D' (down), respectively. In the equations below and in Figure 3.4 describing the reflection and transmission of the combined layer, the operator precedence is like that for matrix multiplication and the chronological order of events is thus right to left.

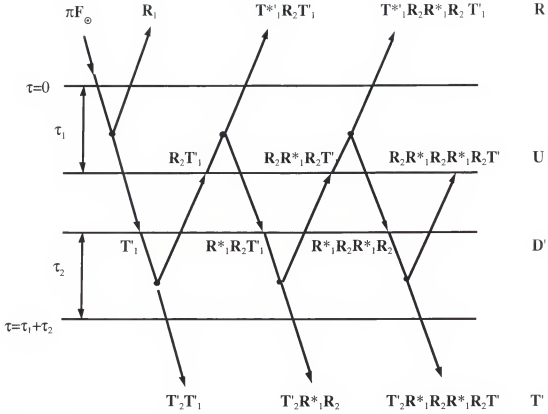


Figure 3.4 Demonstration of adding method.
The layers are separated only for illustrative purposes.

The infinite sums for reflection and transmission of the double layer can be written by considering each path in Figure 3.4. This is often called the interaction principle.

$$\begin{aligned} R &= R_1 + T'^*_1 R_2 T'_1 + T'^*_1 R_2 R^*_1 R_2 T'_1 + T'^*_1 R_2 R^*_1 R_2 R^*_1 R_2 T'_1 + \dots \\ T' &= T'_2 T'_1 + T'_1 R^*_1 R_2 T'_2 + T'_2 R^*_1 R_2 R^*_1 R_2 T'_1 + \dots \end{aligned} \quad (3.22)$$

These can be factored such that

$$\begin{aligned} R &= R_1 + T'^*_1 R_2 \left[1 + R^*_1 R_2 + (R^*_1 R_2)^2 + \dots \right] T'_1 \\ T' &= T'_2 \left[1 + R^*_1 R_2 + (R^*_1 R_2)^2 + \dots \right] T'_1 \end{aligned} \quad (3.23)$$

The series can now be replaced with a single inverse function because of the fact that they are infinite geometric series. If we let c and x be real numbers, with $x \neq 1$, a finite geometric series can be expressed as

$$c + cx + cx^2 + \dots + cx^{n-1} = \frac{c(1-x^n)}{1-x}. \quad (3.24)$$

And if we take the limit as $n \rightarrow \infty$, then the series can be replaced with

$$\frac{c}{1-x}.$$

This means that equation (3.23) becomes

$$\begin{aligned} \mathbf{R} &= \mathbf{R}_1 + \mathbf{T}'_1 \mathbf{R}_2 [\mathbf{1} - \mathbf{R}'_1 \mathbf{R}_2]^{-1} \mathbf{T}'_1 \\ \mathbf{T}' &= \mathbf{T}'_2 [\mathbf{1} - \mathbf{R}'_1 \mathbf{R}_2]^{-1} \mathbf{T}'_1 \end{aligned} \quad (3.25)$$

Similarly, we can find expressions for \mathbf{U} and \mathbf{D}' .

$$\begin{aligned} \mathbf{U} &= \mathbf{R}_2 \mathbf{T}'_1 + \mathbf{R}_2 \mathbf{R}'_1 \mathbf{R}_2 \mathbf{T}'_1 + \mathbf{R}_2 \mathbf{R}'_1 \mathbf{R}_2 \mathbf{R}'_1 \mathbf{R}_2 \mathbf{T}'_1 + \dots = \mathbf{R}_2 [\mathbf{1} - \mathbf{R}'_1 \mathbf{R}_2]^{-1} \mathbf{T}'_1 \\ \mathbf{D}' &= \mathbf{T}'_1 + \mathbf{R}'_1 \mathbf{R}_2 \mathbf{T}'_1 + \mathbf{R}'_1 \mathbf{R}_2 \mathbf{R}'_1 \mathbf{R}_2 \mathbf{T}'_1 + \dots = [\mathbf{1} - \mathbf{R}'_1 \mathbf{R}_2]^{-1} \mathbf{T}'_1 \end{aligned} \quad (3.26)$$

Remember that each of the products above represent integrations over solid angle to take into account the scattering from all directions. Thus the following is a standard recipe to reduce the number of matrix multiplications and integrations for the addition of two layers. The interaction equations (3.25) and (3.26) are simplified by eliminating \mathbf{U} and \mathbf{D}' from this system of equations. First, let us define $\mathbf{S} = \mathbf{R}'_1 \mathbf{R}_2 (\mathbf{1} - \mathbf{R}'_1 \mathbf{R}_2)^{-1}$. By adding one to each side, in the form of

$$\left(\frac{\mathbf{1} - \mathbf{R}'_1 \mathbf{R}_2}{\mathbf{1} - \mathbf{R}'_1 \mathbf{R}_2} \right)$$

on the right, we obtain

$$1 + S = (1 - R^* {}_1 R_2)^{-1}. \quad (3.27)$$

Now by making some substitutions within equations (3.25) and (3.26) we can see that

$$R = R_1 + T^* {}_1 U, \quad T' = T'_2 D', \quad \text{and} \quad U = R_2 D'. \quad (3.28)$$

Combining equations (3.25), (3.26), (3.27), and (3.28) we obtain the following expressions which separately show the direct and diffuse components of the transmission matrices.

$$\begin{aligned} D' &= [1 - R_1 R_2]^{-1} T'_1 = (1 + S)(T_1 + e^{-\tau_1/\mu_o}) = T_1 + S T_1 + S e^{-\tau_1/\mu_o} + e^{-\tau_1/\mu_o} \\ T' &= T'_2 D' = (T_2 + e^{-\tau_2/\mu}) (D + e^{-\tau_1/\mu_o}) \\ &= e^{-\tau_1/\mu_o} T_2 + e^{-\tau_2/\mu} D + T_2 D + \exp \left[- \left(\frac{\tau_1}{\mu_o} + \frac{\tau_2}{\mu} \right) \right] \delta(\mu - \mu_o) \end{aligned} \quad (3.29)$$

The dirac delta function in the equation for T' , represents that fact that the direct transmission only occurs in the incident direction. In order to compute the integrations over solid angle, it is necessary to separate out the direct components from equations (3.29) due to the delta function. This simply means computing the final term separately. Therefore, the recipe for the diffuse reflection and transmission matrices is as follows:

$$\begin{aligned} Q &= R^* {}_1 R_2 \\ S &= Q(1 - Q)^{-1} \\ D &= T_1 + S T_1 + S e^{-\tau_1/\mu_o} \\ U &= R_2 D' = R_2 D + R_2 e^{-\tau_1/\mu_o} \\ R &= R_1 + T^* {}_1 U = R_1 + (T^* {}_1 + e^{-\tau_1/\mu_o}) U = R_1 + T^* {}_1 U + e^{-\tau_1/\mu_o} U \\ T &= e^{-\tau_1/\mu_o} T_2 + e^{-\tau_2/\mu} D + T_2 D \end{aligned} \quad (3.30)$$

The direct transmission of the combined layer is simply given by total transmission minus the diffuse transmission

$$\mathbf{T}^+ \cdot \mathbf{T} = \exp \left[- \left(\frac{\tau_1}{\mu_o} + \frac{\tau_2}{\mu} \right) \right] \delta(\mu - \mu_o) = \exp \left[- (\tau_1 + \tau_2) / \mu_o \right] \quad (3.31)$$

Initialization

The above process becomes useful only if we know \mathbf{R} and \mathbf{T} for the initial layer.

There are two types of solutions to this problem. One in which some other method of solution, like successive orders, which is accurate for thin layers is used to find \mathbf{R} and \mathbf{T} .

Using two methods can lead to many complications in their implementation together.

The other method, used in this implementation, is to choose an initial layer thickness small enough to assume that single scattering is a good assumption and simply set \mathbf{R} and \mathbf{T} to their single scattering values.

Thus, if we consider a thin, homogeneous layer and assume that the single scattering approximation is valid for this layer then the source function, \mathbf{J} , can be written as

$$\mathbf{J}(\tau, \mu, \phi) = \frac{a}{4\pi} \mathbf{F}_o \mathbf{P}(\mu, \mu_o, \phi - \phi_o) e^{-\tau/\mu_o}. \quad (3.32)$$

Given that there is no diffuse radiation at top or bottom of atmosphere, the boundary conditions are

$$\mathbf{I}_{in, top}(\mu, \phi) = 0 \quad \text{and} \quad \mathbf{I}_{in, bottom}(\mu, \phi) = 0. \quad (3.33)$$

Using these boundary conditions and the source function in equation (3.32) in the transfer equation (3.9) gives the reflected and transmitted intensities for a layer of optical thickness $\Delta\tau$,

$$\begin{aligned}
\mathbf{I}_r &= \mathbf{I}(0, \mu, \phi) = \frac{a\mu_o F_o}{4(\mu + \mu_o)} \mathbf{P}(\mu, \mu_o, \phi - \phi_o) \left\{ 1 - \exp \left[-\Delta\tau \left(\frac{1}{\mu} + \frac{1}{\mu_o} \right) \right] \right\} \\
\mathbf{I}_t &= \mathbf{I}(\Delta\tau, \mu, \phi) = \begin{cases} \frac{a\mu_o F_o}{4(\mu - \mu_o)} \mathbf{P}(\mu, \mu_o, \phi - \phi_o) \exp \left[-\Delta\tau \left(\frac{1}{\mu} - \frac{1}{\mu_o} \right) \right], & \mu \neq \mu_o \\ \frac{a\Delta\tau F_o}{4\mu_o} \mathbf{P}(\mu, \mu_o, \phi - \phi_o) e^{-\Delta\tau/\mu_o}, & \mu = \mu_o \end{cases} \quad (3.34)
\end{aligned}$$

Knowing how the reflection and transmission matrices are related to the diffusely reflected and transmitted intensity, equation (3.20), we can now see that the reflection and transmission matrices for a layer of optical depth, $\Delta\tau$, are given by

$$\begin{aligned}
\mathbf{R}(\mu, \phi; \mu_o, \phi_o) &= \frac{a}{4(\mu + \mu_o)} \mathbf{P}(\mu, \mu_o, \phi - \phi_o) \left\{ 1 - \exp \left[-\Delta\tau \left(\frac{1}{\mu} + \frac{1}{\mu_o} \right) \right] \right\} \\
\mathbf{T}(\mu, \phi; \mu_o, \phi_o) &= \begin{cases} \frac{a}{4(\mu - \mu_o)} \mathbf{P}(\mu, \mu_o, \phi - \phi_o) \exp \left[-\Delta\tau \left(\frac{1}{\mu} - \frac{1}{\mu_o} \right) \right], & \mu \neq \mu_o \\ \frac{a\Delta\tau}{4\mu_o^2} \mathbf{P}(\mu, \mu_o, \phi - \phi_o) e^{-\Delta\tau/\mu_o}, & \mu = \mu_o \end{cases} \quad (3.35)
\end{aligned}$$

If $\Delta\tau$ is very small then these expressions simplify to

$$\begin{aligned}
\mathbf{R}(\mu, \phi; \mu_o, \phi_o) &= \frac{a\Delta\tau}{4\mu\mu_o} \mathbf{P}(\mu, \mu_o, \phi - \phi_o) \\
\mathbf{T}(\mu, \phi; \mu_o, \phi_o) &= \frac{a\Delta\tau}{4\mu\mu_o} \mathbf{P}(\mu, \mu_o, \phi - \phi_o) \quad (3.36)
\end{aligned}$$

The actual numerical value to use for $\Delta\tau$ will be discussed in the Implementation section.

Thus, given the knowledge of the phase matrix, the single scattering albedo, the initial optical depth, and the adding recipe we are ready to calculate the reflection and transmission from the entire atmosphere.

Reflection From A Surface At The Bottom Of The Atmosphere

The treatment of a surface at the bottom of the atmosphere is quite simple in this method because with its reflection matrix it becomes just another layer to add at the bottom, albeit the last layer. If we consider l layers, then the surface layer can be denoted with $l+1$. So \mathbf{R}^*_{l+1} becomes the reflection function of the surface and the rest of the formulation is the same except that transmission is disallowed at the surface ($\mathbf{T}_{l+1}=0$). The most commonly used formulation for the reflection matrix of a surface comes from Lambertian reflection characterized by a ground albedo, A_g . The ground albedo is the ratio of the surface reflection to the reflection from a Lambertian (ideal white) surface. The reflected radiation is unpolarized, has a brightness distribution that doesn't change with zenith angle, and is proportional to the intensity striking the surface. The reflection matrix for such a surface is given by

$$\mathbf{R}(\Omega, \Omega') = \begin{pmatrix} A_g & 0 & 0 & 0 \\ 0 & 0 & 0 & 0 \\ 0 & 0 & 0 & 0 \\ 0 & 0 & 0 & 0 \end{pmatrix}. \quad (3.37)$$

Implementation

In this section I will describe the practical details of the radiative transfer calculations based on the above theoretical developments. The implementation of the doubling and adding method used in this study is that of Frank Evans' publicly available FORTRAN code called `rt3` on his web site <http://nit.colorado.edu>. It is described and tested in Evans and Stephens (1991). Further comparisons with another implementation

of the doubling and adding method (Wauben *et al.* 1994) and another solution method, discrete ordinates (Haferman 1995), have shown this method to be accurate.

There are two basic parts into which the implementation of the doubling and adding method can be divided. First it is necessary to convert the single scattering information in the scattering matrix into a form which can then be used as input for the second part, the doubling and adding algorithm. The first part includes the rotation of the phase matrix (cf. equation (3.11)) and its expansion into a Fourier series of the form seen in equation (3.14). Instead of using generalized spherical functions for the expansion (and implicit rotation) of the scattering matrix (Kuscer and Ribaric 1959; de Haan *et al.* 1987), Evans chose to use an FFT on the phase matrix as a function of the zenith and azimuth angles to determine the cosine and sine modes $\mathbf{P}_j^c(u, u')$ and $\mathbf{P}_j^s(u, u')$. The phase matrix as a function of zenith and azimuth angles is obtained by summing the Legendre series representation of the scattering matrix. The zenith angles are selected to satisfy the Legendre-Gauss quadrature scheme whereas the azimuth angles, the number of which is dependent of the number of terms in the Legendre series, are distributed uniformly. The details of the Legendre series representation of the scattering matrix can be found in Appendix B.

Given the azimuth Fourier modes for the phase matrix, we can now initialize an infinitesimal layer and perform the second part, doubling and adding. According to the doubling and adding algorithm described in equation (3.30), this infinitesimal layer is then *doubled* until the desired layer thickness is achieved. The reflection and transmission matrices for each layer in the atmosphere is calculated in this manner and they are then *added* together to determine the reflection and transmission matrices for the

entire atmosphere. The Stokes vectors of the radiation reflected from the atmosphere are then directly available.

Integration Over a Planetary Disk

The term planetary disk is used here to generally refer to any solar system object with a visible disk. There is one last complication to the modeling effort. The Pioneer and Voyager photopolarimetry observations of Titan are disk integrated quantities. In the few cases where they are not, for example when all of Titan does not fit in the field of view of the instrument (Tomasko and Smith 1982), this is still the quantity calculated and reported. It is, therefore, necessary to effectively perform one more set of integrations. The most direct way to conceive of performing this integration is to take the Stokes vectors output from a radiative transfer formulation (functions of zenith and azimuth angle on the planet) and integrate over the visible disk. This was first done by Horak (Horak 1950).

Suppose we are viewing a planet from a variety of phase angles, α (remember that this is the complement of the scattering angle). The distances between the observer (which for generality could be either the Earth or spacecraft) and the Sun, and the observer and the planet are labeled, Δ and r_s , respectively, as shown in Figure 3.5. R is the radius of the planet.

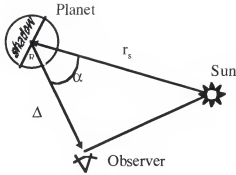


Figure 3.5 Geometry of planetary observations.

Planetary and satellite photopolarimetry observations have traditionally been reported using the notation $p \cdot \Phi(\alpha)$ (Tomasko 1976), where p is the geometric albedo and $\Phi(\alpha)$ is called the phase law or sometimes even the phase function. This can obviously cause some confusion because in light scattering terminology the phase function is a common term for the scalar version of the phase matrix. I will show that this phase law, while similar to the phase function, does have some important differences. But first some basic definitions. The geometric albedo is a ratio of the flux received from a planet to that one would receive from a Lambertian disk with the same radius placed at the same distance from the observer normal to the direction from planet to observer.

$$p = \frac{F_p(\alpha = 0)}{F_{LD}(\alpha = 0)} \quad (3.38)$$

A Lambertian disk perfectly reflects an amount of light which depends only on the incident direction and can thus be described by

$$\mathbf{I}_{LD} = \mu_o \mathbf{F}_o \quad (3.39)$$

given incident intensity as in equation (3.19). The phase law is defined as the ratio of the flux from the planet as a function of phase angle α to that at $\alpha=0^\circ$.

$$\Phi(\alpha) = \frac{F_p(\alpha)}{F_p(\alpha=0)} \quad (3.40)$$

In other words, it is the reflected flux normalized to the backscattered flux and we can thus see that it is different from the phase function used in light scattering terminology that is subject to the normalization condition in equation (3.7). When equations (3.38) and (3.40) are combined, we get an expression for the geometric albedo times the phase law.

$$p \cdot \Phi(\alpha) = \frac{F_p(\alpha)}{F_{LD}(\alpha=0)} \quad (3.41)$$

$F_p(\alpha)$

In order to put the radiative transfer results, Stokes vectors as a function of zenith and azimuth angle, into a form which we can use to compare with spacecraft observations, we need expressions for $F_p(\alpha)$ and $F_{LD}(\alpha=0)$. The intensity of a Lambertian disk at $\alpha=0^\circ$ is simply based on equation (3.39) at an incident zenith angle of 0° ($\mu_0=1$). So the flux arriving at the observer from this disk is the intensity integrated over the solid angle subtended by the disk as seen from the observer. As shown in Figure 3.6, the differential annulus of area, dA , subtends a solid angle $d\Omega = dA/\Delta^2$ which can be written in the following form:

$$d\Omega = \frac{dA}{\Delta^2} = \frac{2\pi r dr}{\Delta^2} = \frac{2\pi R \sin \theta \cdot R \cos \theta d\theta}{\Delta^2} = \frac{2\pi R^2 \cos \theta d(\cos \theta)}{\Delta^2} = \frac{2\pi R^2 \mu d\mu}{\Delta^2}. \quad (3.42)$$

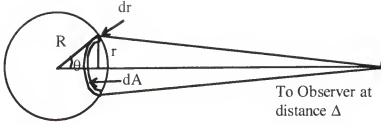


Figure 3.6 The differential solid angle subtended by a disk as seen by an observer.
 $d\Omega = dA/\Delta^2$

Using equation (3.2) we can get an expression for the flux.

$$\mathbf{F}_{LD}(\alpha = 0) = \int_{disk} \mathbf{I}_{LD} d\Omega = \frac{2\pi R^2}{\Delta^2} \int_0^1 \mathbf{F}_o \mu d\mu = \frac{\pi R^2 \mathbf{F}_o}{\Delta^2} \quad (3.43)$$

Note that $\mathbf{F}_{LD}(\alpha = 0)$ is a Stokes vector, albeit with Q, U, and V equal to zero (a Lambertian surface by definition reflects unpolarized light).

Now we need to use a similar argument to get an expression for the flux from the planet, $\mathbf{F}_p(\alpha)$, although the geometry of the problem is slightly more complicated because we need to concern ourselves with how much of the disk is visible as a function of phase angle. We start with the Stokes vectors of the intensity at the top of the atmosphere in the local coordinate system depicted in Figure 3.2 and Figure 3.3, $\mathbf{I}(\mu, \mu_o, \phi - \phi_o)$, which is calculated in the previous sections. But now we need to define a new planetocentric coordinate system in order to integrate over the surface of the visible crescent or gibbous planet. As shown in Figure 3.7 we will use μ , the cosine of the zenith angle θ , and χ as our planetary coordinates. χ is the complement to i_2 , one of the rotation angles in Figure 3.3 (de Rooij 1985). This choice will show its merits when we perform the disk integration.

In order to obtain the Stokes vector of the reflected radiation with respect to the plane containing the planet, Sun, and observer, denoted \mathbf{I}_{ps0} , (one could consider this to be the planetary scattering plane if we imagine the planet as one large scatterer), we need to rotate it through the angle χ (counterclockwise when looking in the direction of propagation, \mathbf{k}). This is done using the rotation matrix defined in equation (3.11) so that

$$\mathbf{I}_{ps0}(\mu, \mu_o, \phi - \phi_o) = \mathbf{L}(\chi) \mathbf{I}(\mu, \mu_o, \phi - \phi_o). \quad (3.44)$$

In order to obtain the flux at the observer from the visible crescent we need to integrate the intensity over the solid angle that it subtends, $d\Omega = dA/\Delta^2$. This can, in effect, be thought of as integrating along circles around the sub-observer point on the planet. An element of area on the disk, dA , is given by

$$dA = (R \sin \theta)(R d\theta) d\chi = R^2 d\mu d\chi. \quad (3.45)$$

Therefore the flux of the planet, as seen by an observer at distance Δ , is

$$\mathbf{F}_p(\alpha) = \int_{VC} \mathbf{I}_{ps0} d\Omega = \frac{R^2}{\Delta^2} \int_0^1 \int_{-\chi_1(\mu, \alpha)}^{\chi_1(\mu, \alpha)} \mathbf{I}_{ps0}(\mu, \mu_o, \phi - \phi_o) \mu d\chi d\mu \quad (3.46)$$

where χ_1 is the value of χ at the terminator. And finally, we arrive at an expression for

$$\mathbf{p} \cdot \boldsymbol{\phi}(\alpha) = \frac{\Phi_p(\alpha)}{\Phi_{LD}(\alpha = 0)} = \frac{\int_0^1 \int_{-f(\mu, \alpha)}^{f(\mu, \alpha)} \mathbf{I}_{ps0}(\mu, \mu_o, \phi - \phi_o) \mu d\chi d\mu}{\pi \mathbf{F}_o}. \quad (3.47)$$

Note that in this representation, $\mathbf{p} \cdot \boldsymbol{\phi}(\alpha)$ is a stokes vector.

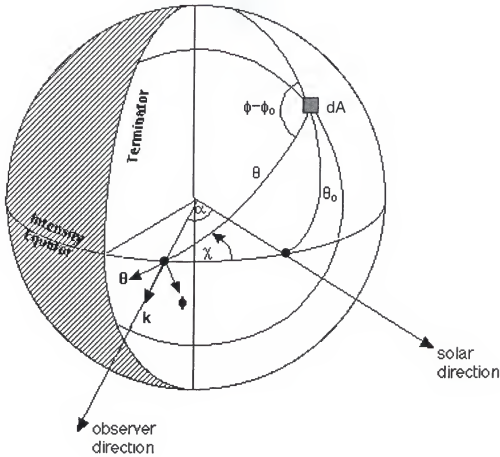


Figure 3.7 Planetocentric coordinate system.

The variables in the integrand and integration limits of equation (3.47), μ_o , $\phi - \phi_o$, and $\chi_t(\mu, \alpha)$, can be expressed in term of the integration variables, μ and χ , and the phase angle, α , by employing spherical trigonometry. Applying the cosine rule for the spherical triangle between the sub-observer point, the sub-solar point, and the differential area, dA , in Figure 3.7 results in

$$\mu_o = \mu \cos \alpha + \sqrt{1 - \mu^2} \sin \alpha \cos \chi. \quad (3.48)$$

Applying it again, but this time to the complement to $\phi - \phi_o$, we obtain

$$\cos(\phi - \phi_o) = \frac{\mu\mu_o - \cos\alpha}{\sqrt{(1-\mu^2)(1-\mu_o^2)}}. \quad (3.49)$$

In order to get an expression for $\chi_t(\mu, \alpha)$, we can use equation (3.48) with the fact that, by definition, $\mu_o=0$ at the terminator (located at 90° from the direction to the Sun). Thus

$$0 = \mu \cos \alpha + \sqrt{1 - \mu^2} \sin \alpha \cos[\chi_t(\mu, \alpha)], \quad (3.50)$$

giving,

$$\chi_t(\mu, \alpha) = \arccos\left(\frac{-\mu}{\sqrt{1 - \mu^2} \tan \alpha}\right). \quad (3.51)$$

The basic chain of events in the evaluation of equation (3.47) begins with the Fourier series in intensity, $\mathbf{I}_m(\mu, \mu_o)$, as defined in equation (3.15). Because the numerical integration of equation (3.47) is performed using Gauss-Legendre quadrature, the intensity must be interpolated at the values of μ_o , calculated by equation (3.48). As long as the mesh chosen for the μ quadrature in rt3 is sufficient, then there is no need to interpolate in the μ direction. $\mathbf{I}_m(\mu, \mu_o)\mu$ is a smoother function than $\mathbf{I}_m(\mu, \mu_o)$ and so it yields more accurate interpolation results (de Rooij 1985). Now that we have $\mathbf{I}_m(\mu, \mu_o)\mu$ at the points (μ, μ_o) over which we need to integrate, the Fourier series can be summed according to equation (3.15) for the azimuth differences calculated in equation (3.49) to give $\mathbf{I}(\mu, \mu_o, \phi - \phi_o)\mu$. The last thing left to do before integration is to rotate the Stokes vector by χ .

We can simplify the integration by recognizing the fact that the coordinates for points on the southern hemisphere are equal (μ and μ_o) or equal but opposite in sign (χ and $\phi - \phi_o$) to those in the northern hemisphere. The Stokes vector then obeys (Hovenier 1969) the following symmetry relation

$$\mathbf{I}(\mu, \mu_o, \phi - \phi_o) = \mathbf{D}\mathbf{I}(\mu, \mu_o, -(\phi - \phi_o)) \text{ where } \mathbf{D} = \begin{pmatrix} 1 & 0 & 0 & 0 \\ 0 & 1 & 0 & 0 \\ 0 & 0 & -1 & 0 \\ 0 & 0 & 0 & -1 \end{pmatrix}. \quad (3.52)$$

The integration can, thus, be separated into parts for the northern and southern hemisphere and only one part need be calculated numerically as the other can be obtained analytically from the first part.

$$\begin{aligned} \mathbf{p} \cdot \boldsymbol{\phi}(\alpha) &= \mathbf{p} \cdot \boldsymbol{\phi}(\alpha)_N + \mathbf{p} \cdot \boldsymbol{\phi}(\alpha)_S = \mathbf{p} \cdot \boldsymbol{\phi}(\alpha)_N + \mathbf{D}\mathbf{p} \cdot \boldsymbol{\phi}(\alpha)_N \text{ where} \\ \mathbf{p} \cdot \boldsymbol{\phi}(\alpha)_N &= \frac{\int_0^1 \int_0^{f(\mu, \alpha)} \mathbf{I}_{ps0}(\mu, \mu_o, \phi - \phi_o) \mu d\chi d\mu}{\pi \mathbf{F}_o} \end{aligned} \quad (3.53)$$

There are at least five other existing methods to do the disk integration (Horak 1950; Sobolev 1975; van de Hulst 1980; de Rooij 1985), all of which have their merits and problems. I chose the above system to capitalize on the need for interpolation in only one integration variable which should be faster and more accurate than interpolating in both integration variables. It seems that most observers use Horak's method so I will give it a brief overview. He chooses a coordinate system using the co-latitude and longitude angles defined from the intensity equator and the direction to the observer (or sub-Earth point as the observations he was concerned with were, at that time, only made from the Earth), respectively as reference directions. He then uses a transformation of variables in order to employ a Chebyshev quadrature scheme for the transformed co-latitude coordinate integration and a Gauss-Legendre quadrature scheme for the longitude coordinate integration. This method, while simplifying the integration, requires more interpolation and thus is clearly more time intensive and less accurate.

Testing and Sensitivity Studies

All of the FORTRAN radiative transfer computing was done on a 500 MHz DEC Alpha operating under Digital Unix. The disk integration is then performed separately using a code titled Diskint I developed in IDL and run under MacOS.

Testing Rt3

In testing the rt3 code, I first ran an example case for which results came with the code distribution. Evans (1991) calls it the “Mie test case” and makes comparisons to what is called the L=13 problem for which results have been published using several different methods of solution to the transfer equation (Garcia and Siewert 1986; Garcia and Siewert 1989). The basic characteristics of the problem are an atmosphere, with optical thickness $\tau=1$, populated with a gamma size distribution of spheres with index of refraction $n=1.44$ and a single scattering albedo $a=0.99$. Note that this is an artificial choice for the single scattering albedo because if the index of refraction does not have an imaginary part, then there is no absorption and the single scattering albedo should equal one. The gamma distribution has an effective radius, $r_{\text{eff}}=0.2 \mu\text{m}$, and an effective variance, $v_{\text{eff}}=0.07$. The surface is represented with a Lambertian ground albedo $A_g=0.1$. The incident radiation has a wavelength of $\lambda=0.951 \mu\text{m}$, a zenith angle such that $\mu_0=0.2$, and is unpolarized so that $\mathbf{F}_o = (1 \ 0 \ 0 \ 0)^T$. My results for I and Q are all exactly the same as those that Evans reports but U and V have absolute errors not larger than 10^{-12} although 10^{-15} is more usual. This only tells me that the code works the same for me as it did for Evans.

In order to make sure that the code works well compared to other radiative transfer models that exist in the literature I ran a test case based on an atmosphere of spheroidal particles. I chose this case for two reasons. The first being that it was one of the only types of models available for comparison that was not based on spheres. And since spheres have a more simplified scattering matrix than even the form found in equation (2.11), I felt it was important to find a model that had a phase matrix in the form of equation (2.11). The other reason is that the models I chose for comparison were intended to be used as benchmark results (Wauben and Hovenier 1992) (hereafter denoted as W&H) and for this reason the papers contained all the necessary information to reproduce their results. The radiative transfer calculations with which I am comparing my *rt3* results were calculated using another implementation of the doubling and adding method and the F_N method. The F_N method was developed for use in neutron transport theory (Siewert and Benoist 1979) and is related to the spherical harmonics method. In the discrete ordinate method the integral of intensity as a function of zenith angle is replaced by a sum of n discrete values at n zenith angles (sometimes called n streams). Whereas in the spherical harmonics method the intensity is expanded in spherical harmonics. For the azimuthally symmetric case, the two methods are identical.

The model is based on an atmosphere containing randomly oriented oblate spheroids with an aspect ratio $a/b=1.999987$, a size parameter (π times the length of the major axis divided by the wavelength) $x=3.0$, and a refractive index $m=1.55-0.01i$. An oblate spheroid is generated by rotating an ellipse about its minor axis whereas a prolate spheroid is generated by rotating an ellipse around its major axis. Oblate spheroids can range in shape from a disk to a sphere and prolate spheroids range in shape from a needle

to a sphere. The single scattering results which were used as input to the radiative transfer model were calculated by Kuik *et al.* (1992) using the T-matrix method and an analytical method developed by R. W. Schaefer. We will, thus, call this Kuik model 2.

The phase matrix is presented in the form of generalized spherical function expansion coefficients. So in order to use them for input to rt3 it was necessary to calculate the scattering matrix elements, and then find the Legendre expansion coefficients for this scattering matrix. I was able to test this procedure using the generalized spherical function coefficients published for the $L=13$ case above and comparing the Legendre series coefficients I calculated with those published by Evans. The basic characteristics of this model are a perfectly absorbing surface, $A_g=0$, an optical thickness, $\tau=1$, an incident zenith angle specified by $\mu_0=0.6$, and an incident flux of $F_o = (1 \ 0 \ 0 \ 0)^T$. The agreement I get between rt3 output and the published results is good.

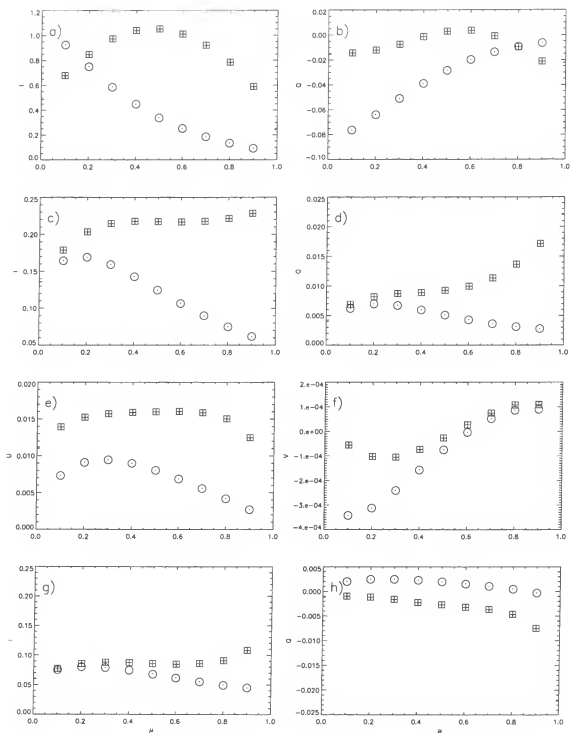


Figure 3.8 Comparison of rt3 and W&H Stokes parameters results for Kuik model 2. The symbols $+$ and \times represent W&H results at $\tau=0$ (top of the atmosphere) and $\tau=1$ (bottom), respectively. The symbols \circ and \bullet represent rt3 output at $\tau=0$ and $\tau=1$ respectively. Parts a) and b) are $\phi=0^\circ$, c), d), e) and f) are $\phi=90^\circ$ and g) and h) are $\phi=180^\circ$, where ϕ is the outgoing zenith angle.

W&H results were tabulated at intervals of 0.1 in μ so the rt3 results must be interpolated in order to make direct comparisons because rt3 uses Gaussian quadrature to determine the actual μ values at which intensities are calculated. Note that since W&H also use Gaussian quadrature it is therefore implied (but never explicitly stated) that their values are also interpolated. This interpolation is not the ideal situation but it seems to be standard among reported results and more likely than not it is the largest source of error in these comparisons. Table 3.1 shows the absolute and fractional differences between W&H results and interpolated rt3 output. The fractional difference is the absolute difference divided by the maximum value of the quantity in question. This is done for each azimuth angle and for transmission and reflection ($\tau=0$ or $\tau=1$) separately and then the averages and maximums for all of the values can be determined. The absolute differences reported by W&H for their results as compared to the F_N method of Garcia and Siewert range from 10^{-4} to 10^{-6} for I, 10^{-5} to 10^{-7} for Q, 10^{-6} to 10^{-7} for U, and 10^{-8} to 10^{-9} for V. These numbers are based on inspection of their tables and their statement that the values in their tables agree with those of the F_N method to within ± 1 in the last digit reported.

Table 3.1 Differences between rt3 output and W&H results for Kuik model 2.

	I	Q	U	V
Absolute Differences				
average	9.17E-05	3.53E-06	3.22E-06	1.74E-07
maximum	4.63E-04	1.45E-05	9.95E-06	6.41E-07
Fractional Differences				
average	3.00E-04	2.84E-04	2.98E-04	9.45E-04
maximum	8.53E-04	1.50E-03	1.05E-03	2.86E-03

Pioneer 11 disk integrated photometry has a relative error near 3%, affecting the shape of the curve, and an error in the absolute calibration of approximately 10% (one sigma) uncertainty. Polarization uncertainties are much smaller, normally less than 1%, although the instrumental depolarization corrections used were based on pre-flight calibration because after launch it was not possible to observe a highly polarized source for calibration purposes (Tomasko and Smith 1982). Uncertainties in the polarization measured by the Voyager 2 spacecraft were also mostly less than 1%. It is believed that there was a hysteresis effect caused by filter cycling and that this systematically increased the polarization measure by 0.82%. The characterization of this hysteresis effect is, however, incomplete in that its relationship to an increasing count rate is poorly understood. This leaves the possibility for further systematic errors to exist in the data. The Voyager 2 intensities show irregular behavior at small and large phase angles. The cause for this is not understood although possible contributors are thought to include the hysteresis effect, temporal drift in instrument sensitivity, and/or changing sensitivity across the detector field of view (West *et al.* 1983). All of this suggests that the above errors in Table 3.1 are certainly well below that needed to compare model results to the observed photopolarimetry.

Testing Disk Integration

The disk integration code has also been tested successfully. The first case used to test intensity only is one for which an exact expression exists, that of Lambertian reflection. The expression for intensity reflected from such a disk is found by using

equation (2.1) in equation (2.6) and was first derived by Schoenberg (1929; de Rooij 1985).

$$p \cdot \phi(\alpha) = \frac{8}{3\pi} [\sin \alpha + (\pi - \alpha) \cos \alpha] \quad (3.54)$$

Figure 3.9 displays how well the Diskint results match the analytical expression in equation (2.11).

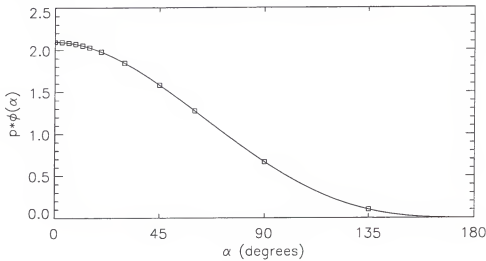


Figure 3.9 Analytical (line) and Diskint results (squares) for the Lambertian test case.

The second case considered, for which comparison calculations have been published (Kattawar and Adams 1971), is Rayleigh scattering. They published results for several optical depths and ground albedos. I chose two test cases with $A=0.8$ and $A=0$ because the radiative transfer results (intensity as a function of zenith and azimuth angles on the disk) were also published for this case (Coulson 1960) and so the entire process could be tested with consistency. The other characteristics for this atmosphere are $\tau=1.0$ and single scattering albedo, $a=1.0$. Figure 3.10 shows these comparisons.

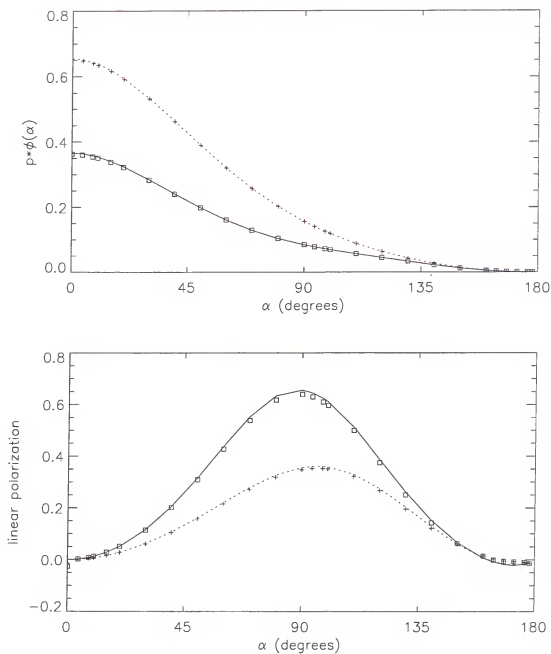


Figure 3.10 Diskint results for two Rayleigh scattering test cases, $A=0.8$ and $A=0$. Kattawar and Adams' (1971) results are represented with lines, solid for $A=0$ and dashed for $A=0.8$. Diskint results are represented with symbols, squares for $A=0$ and crosses for $A=0.8$.

Parameter Sensitivity Tests

In order to understand how the three major input parameters, the number of quadrature angles, the number of azimuth modes, and the initial optical depth, affect the accuracy of the results, I ran the Kuik model 2 test case while varying these input parameters. First I considered the number of quadrature angles by starting with 28. The number of Legendre terms for Kuik model 2 case is the same as for Evan's test case, L13, and he showed results for two cases, $N_m=14$ and $N_m=28$ for which the Kuik model 2 results show similar absolute and fractional differences.

There are two things to consider here, one is that the computing time is proportional to the cube of the number of angles so it is important not to use more angles than necessary. But it is also important to use enough angles so as not to truncate the Legendre series representing the phase matrix. Essentially, the reason for this amounts to a conservation of energy argument. One can think of this in terms of bookkeeping in that it is important that the integrals over scattering angle properly account for the radiation scattered in all directions so that we do not lose track of any energy. Another way to look at this is that if there are not enough division points then some amount of artificial absorption is introduced.

If we look at how the $rt3$ output changed as the number of Gaussian division points is increased, we expect to find that at some point the results will converge to some steady state values. This didn't happen. I started with the Kuik model 2 results above for 28 quadrature angles and I increased the number of angles in increments of two to 64 and the maximum absolute difference steadily decreased to 1.2×10^{-5} . But if we go back and consider what our requirements are in the way of accuracy, as mentioned in the previous

section, we can see that the changes in the maximum absolute differences are negligible for the case we wish to study. If we investigate the other two parameters, the number of azimuth modes and the initial optical depth in the same manner, the resulting changes in the maximum absolute differences are even smaller.

Now consider the dependence of accuracy of the radiative transfer results on errors in extinction cross section and scattering cross section (i.e. single scattering albedo). In order to account for possible experimental errors in the extinction and scattering cross-sections, I tested the sensitivity of the overall results (rt3+diskint) to single scattering albedo. I ran Kuik's model 2 for varied single scattering albedos, decreasing it by 5% for each run. This is an unphysical test because there is no physical parameter (index of refraction, size, shape, etc...) that corresponds directly to single scattering albedo, although more absorbing materials give rise to lower single scattering albedos. But since what I really want to explore is how experimental errors in extinction and scattering cross-sections affect the model results, it is a fair test of this because the single scattering albedo is the parameter used to encompass both experimental cross-sections.

The results are shown in Figure 3.11. The maximum in the intensity curves steadily decreases with decreasing single scattering albedo and the shape of the curve also suffers an increased damping. Polarization shows the opposite effect. The maximum polarization increases with single scattering albedo and the variation across phase angle increases. This shows that for each case I would like to run, I will get a family or range of solutions the width of which will depend on how well determined the extinction and scattering cross sections are.

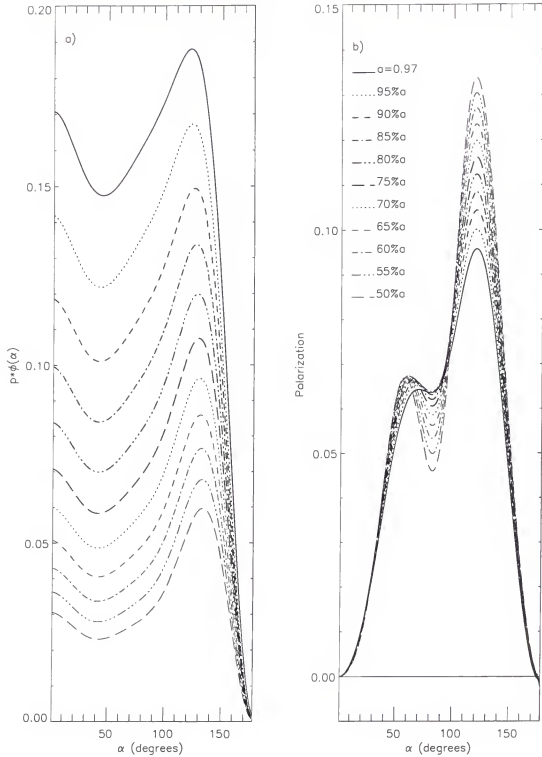


Figure 3.11 Single scattering albedo sensitivity test. The solid line is the nominal case using the single scattering albedo calculated by Kuik. The dashed lines represent cases for which the single scattering albedo has been decreased by the specified percentage.

Surface and Semi-Infinite Atmosphere Tests

These tests are related and self-consistent. It is intuitive that an atmosphere with a large enough optical depth is indifferent to any surface below. First the optical depth which approximates a semi-infinite atmosphere is determined by increasing the optical depth until the results do not change further. For a single scattering albedo of one (the extreme case), an optical depth of 800 or larger produces the same result and can be considered semi-infinite. At a single scattering albedo of 0.5 an optical depth of 100 is sufficient. Next, the results of a test showing that including a surface albedo, A , is inconsequential to the overall result for a semi-infinite atmosphere can be seen in Figure 3.12. In order to test the conditions that I will be using to simulate Titan's atmosphere, I have used a particle from Chapter 2 to populate the atmosphere rather than one of the test particles used above.

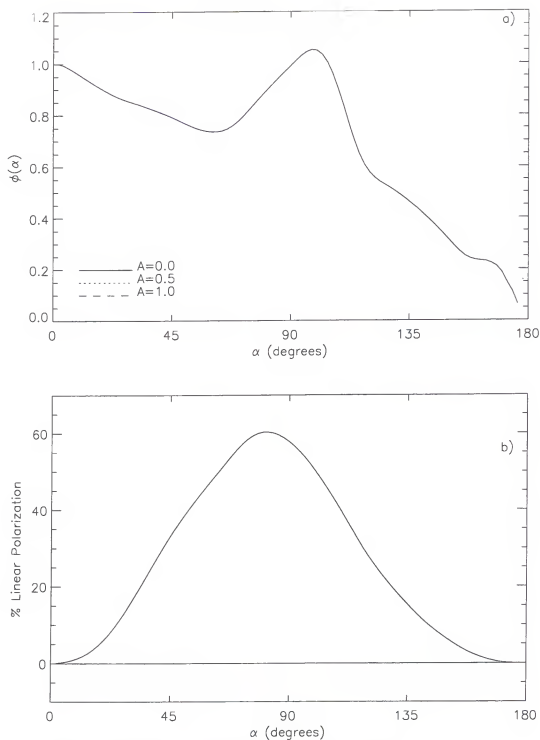


Figure 3.12 Surface albedo test using the X1 aggregate at 264 nm.

Size Distribution Test

Remembering that the single scattering data measured in the laboratory is measured at 85 discrete frequencies, it is possible to explore the concept of using the laboratory waveband to simulate a size distribution. In Chapter 2 we discussed a scheme for integration across a waveband to simulate observations through a filter. The method for simulating a size distribution is the same in principle. The frequency distribution can simply be converted to a size parameter distribution and any set of weights can then be convolved with the data. This results in a single scattering matrix applicable to a size distribution of identical particles (except for size) at the wavelength corresponding to the effective size parameter for the particular distributions chosen.

The one drawback to using the laboratory waveband to simulate a size distribution is that it is unrealistically narrow for most natural size distributions (for examples see Deirmendjian 1969). This is, however, an expedient way to run models for all of the particles in Chapter 2. Then for models which show promise the radiative transfer can be run for the two color models which takes twice the computing time and preparation since each wavelength requires a separate radiative transfer model run.

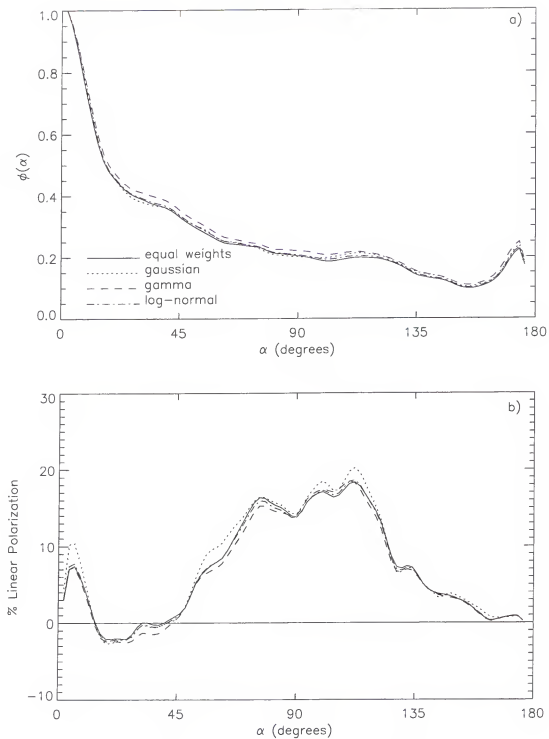


Figure 3.13 OA radiative transfer model results for four size distributions. a) phase law and b) polarization results for equal weighted, Gaussian, gamma, and log-normal distributions.

Four types of distributions were tested: equal weights (i.e. a step-function where all frequencies or sizes have equal weight), Gaussian, log-normal, and a standard gamma distribution (after Hansen and Travis (1974)). The difference between the results for these different distributions is negligible (see Figure 3.13) so the equal weights version was chosen for all subsequent models for simplicity. The Gaussian distribution shows the largest deviation from the others due to the fact that it is the narrowest distribution but even this difference is insignificant, especially when the differences between the various targets are considered.

We now have all the tools necessary to make model calculations of Titan's atmosphere in order to compare with the spacecraft observations. This is the topic of the next chapter.

CHAPTER 4

MODEL CALCULATIONS OF TITAN'S ATMOSPHERE

This chapter represents the culmination of the experimental and theoretical modeling efforts of the previous chapters. So we will naturally begin with an overview of the entire modeling process employed to produce the following results. Next we will review the pertinent observational constraints. The results for simple, single layer atmospheric models populated with each type of particle discussed in chapter 2 are presented first. Also considered are two layer models containing different particle populations in each layer as well as single layer dual population models. Furthermore, I have included examples of predictions for Cassini/Huygens. From these results conclusions are drawn and suggestions for future work are elucidated.

Overview of Entire Modeling Procedure

The flow chart in Figure 4.1 outlines the steps taken to use single scattering measurements in combination with radiative transfer modeling to obtain quantities that can be compared with astronomical observations. Most of the details of these individual operations have been discussed previously. Fitting the various scattering matrices with Legendre polynomials is illustrated in Appendix B.

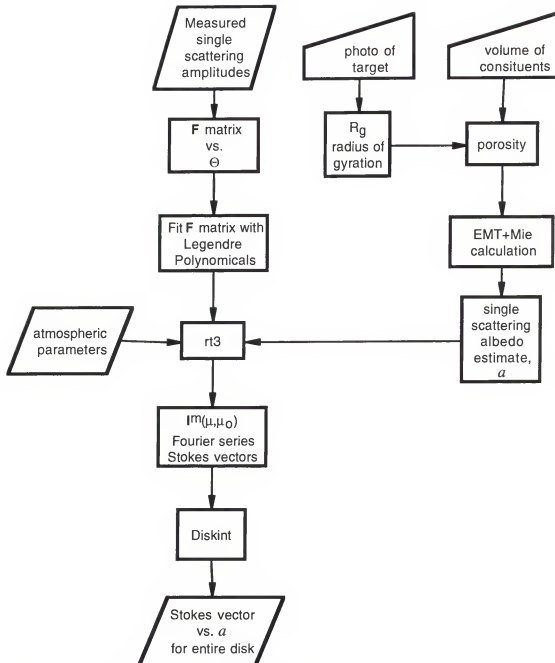


Figure 4.1 Flow chart of entire modeling process.

The single scattering albedos in Table 4.1 are determined by the method shown in Figure 4.1. The porosity is determined from photographs as discussed in Chapter 2. This is then used in an Effective Medium Theory calculation to determine an effective

refractive index. The single scattering albedo estimates in Table 4.1 are then found using Mie theory for an equal volume sphere with that refractive index. The error inherent in this estimation method requires the following radiative transfer results to have a range of possible results as discussed in Chapter 3.

Table 4.1 Single scattering albedo estimates for all the laboratory targets

Target	a
CYA	0.99
LSA	0.86
SA	0.99
CA	0.60
OA	0.54
1.5" cube	0.81
0.5" cube	0.91
LSA red	0.89
LSA blue	0.83

Note: The value for the 0.5" cube is calculated using the DDA. The value for the 1.5" cube is calculated from an equal volume sphere. The values for the aggregates are found using the method described in the text and they are integrations over the entire laboratory waveband in the same manner as the scattering matrices except the two LSA values at the bottom in which the laboratory spectrum has been split into red and blue intervals.

Observations

Remembering that our overall goal is to compare our combination of laboratory single scattering measurements and theoretical multiple scattering calculations to observations of Titan, a brief overview of the available observational data is in order. The outstanding features in the Pioneer and Voyager polarimetry are the blue polarimetric color and the polarization peak near phase angle 90° for all four wavelengths (c.f. Figure 1.1). There is a steady decrease in the maximum polarization with increasing wavelength.

Another important characteristic to note is whether there is negative polarization at small phase angles also known as the polarization opposition effect (Kolokolova and Zaitsev 1999). This effect most commonly arises from atmosphereless bodies with regoliths but has also been seen for Saturn's ring particles (Mishchenko 1993) and would indicate the possible presence of small regolithic (as in irregular rock and ice type particles) particles. The Pioneer data does not contain any phase angles smaller than 20° . The Voyager 2 polarization data in combination with ground-based polarization measurements made for phase angles between 0° and 6° (Zellner 1973) indicate that it is possible that the polarization at small wavelengths (264 nm and 360 nm) may be polarized negatively but if so it is only to a very small degree.

Table 4.2 Observed Geometric albedo of Titan at the photopolarimetry wavelengths.

Wavelength (nm)	Geometric albedo
264	0.031
452	0.093
648	0.222
750	0.246

Note: The data at the shortest wavelength is from the IUE (International Ultraviolet Explorer) spacecraft (Courtin *et al.* 1991). The values at the other wavelengths are from ground-based data (Neff *et al.* 1984). In all cases, these values have been corrected due to the fact that the size of the visible disk of Titan changes with wavelength (Toon *et al.* 1992; Lemmon 1994) because the level in the atmosphere at which the optical depth becomes sufficiently large to create a visible limb changes with wavelength. It is also important to remember that Titan's geometric albedo varies by as much as 10 % with season (Lockwood *et al.* 1986).

Furthermore, Titan has a red color as seen from the geometric albedo (see Table 4.2). However, the shape of the phase law is independent of wavelength at intermediate phase angles. As discussed in Chapter 3, planetary photometry results are generally

presented using the quantity $p \cdot \phi(\alpha)$ which represents the geometric albedo times the phase law (flux normalized to the backscattering flux). This however confuses the issues of color (the relative positions of the phase laws at different wavelengths) and shape of the phase law. Therefore, I have removed the geometric albedo from the photometry presented by West and Smith (1983) and Tomasko *et al.* (1982) in order to compare the phase laws directly with the calculations. This also allows a separate comparison of the geometric albedos found for the models to that measured for Titan.

Single Layer Model Results

The results for semi-infinite plane parallel atmospheres populated with equally weighted size distributions of all of the targets in this study are presented in this section. This allows us to rule out those targets that are poor matches to the observational data and further concentrate on those that provide more promise. To that end the LSA model shows enough promise to study its color characteristics by considering the red and blue laboratory wavebands separately. These results are found at end of this section.

The small cube shows the worst match of all the targets to the polarization (see Figure 4.2). The shape of the phase law for the 1.5" cube model matches the Pioneer photometry quite well but the polarization peak is not nearly large enough to match the observations in addition to being shifted to larger phase angles (see Figure 4.3). From these models we can conclude that cubic particles of these sizes are not going to be found in the atmosphere of Titan and that this type of modeling effort can distinguish between a plausible model and one that can be excluded.

The OA can also be excluded from our plausible list due to a polarization maximum that is a factor of two to three too low and approximately 20% excess intensity at the phase angles near 90° (see Figure 4.4). The CYA is also clearly a poor representation of Titan's aerosols. It is severely lacking in polarization although the modeled phase law matches the observations to within 10% (c.f. Figure 4.5). The single scattering properties of the BSA are so similar to those of the CYA that it is not necessary to calculate the radiative transfer solution for the BSA. The polarization, as shown in Figure 4.6 for the SA model is also clearly too low and we can also rule out this type of aggregate. The polarization peak for the CA (as seen in Figure 4.7) is a factor of 1.3 to 2 too low and shifted too far in the high phase angle direction. The phase law is also a very poor fit (although some of the structure in the curve may be unrealistic due to averaging over too few orientations in the microwave laboratory) and so we can also rule out this type of target as a possibility for Titan's atmospheric aerosols.

Of all of the targets measured in the microwave laboratory for this study, the LSA shows (in Figure 4.8) the most promise for helping us understand the Titanian aerosols. The slope of the phase law seems to match the observations (which do not change much with wavelength) better as the single scattering albedo is increased. Interpreting the polarization plot is a bit trickier because now we see that the spacecraft observations do change with wavelength. First we can see that the models with lower single scattering albedos come very close to matching the observations (with the exception of phase angles near 100°) at the two longer spacecraft wavelengths of 648 nm and 750 nm. However, we should remember that the refractive index for the LSA (c.f. Table 2.2) is in between that for Titanian tholin (c.f. Table 1.1) at blue (452 nm) and red (648 nm) wavelengths. A

physical explanation for larger single scattering albedos producing worse fits to the phase law, is that as more scattering occurs, the large forward scattering peak in these large aggregates gets spread out to larger scattering angles (spread from $\alpha=180$ backwards towards lower phase angles) raising the curve above the observational data.

In order to understand the effect of color produced by scattering (removed from color due to refractive index) on the multiple scattering results, the same model was run as above but the scattering matrix was replaced with that integrated over a narrower waveband. Two models were run, one for the red laboratory waveband and one for the blue laboratory waveband. The results can be seen in Figure 4.9 and Figure 4.. As the single scattering albedo gets larger in both cases, the phase law fit improves. The opposite trend appears for polarization in that as the single scattering albedo decreases, the fit would seem to improve. The trend with albedo is the same as for the single color case discussed above. The polarization for the blue case is not large enough to even match the lowest polarization in the near IR wavelengths. Polarization in the red gets up to 60% which makes it a better fit, however, the LSA model polarization at red wavelengths is larger than at blue ones which is opposite to the Titan observations.

The last single layer case to consider is that of the aggregates labeled X1-X4 for which single scattering calculations were provided to me by Y.-L. Xu. This model is almost identical to that used by others to fit the photopolarimetry. The details of these fits are not as important as the simple fact that this type of aggregate was used in combination either with other particles or a surface (in other words parameters beyond the type of particles about which we are attempting to learn). If you use enough parameters an elephant can easily be made to look like a rhinoceros. Therefore, the goal

here is to compare this type of aggregate with my other targets under the same conditions; in other words, a semi-infinite atmosphere populated with one type of particle that does not include non-physical assumptions. This is important before we consider any modifications to either the type of particles with which we want to populate the model or structure of the atmosphere or the inclusion of a surface.

Thus, Figure 4.11 shows that this aggregate is not necessarily an outstanding candidate in these conditions and that it is obviously important to consider what other elements might need to be included to improve the fit. The phase law for the X3 model provides a reasonable fit to the observed phase law at 648 nm. The polarization maximum for the X1 model is a good match to that for the observed polarization maximum at 264 nm. The model peak is, however, shifted a bit to lower phase angles than the observed peak due mostly to the fact that the single scattering polarization curve is also shifted towards lower phase angles (higher scattering angles, e.g. Figure 2.26). This might imply that the size of the constituents in this aggregate are larger than those producing the observations since the polarization of an aggregate will closely resemble that of its constituents (Gustafson and Kolokolova 1999) and as small spheres approach a size parameter of one from below the polarization peak shifts towards higher phase angles rather than lower ones. The polarimetric color for X2-X4 (disregarding this model in the UV) has the same qualitative trend as Titan. The model polarizations at the other three wavelengths are significantly too large. At this point it is not possible to claim that these particles provide a complete explanation for Titan's photopolarimetry.

In order to get a better understanding of the effect that aggregation has on the resulting photopolarimetry characteristics, the same models were performed for single

constituent spheres from the X1-X4 aggregates. The results of these models are seen in Figure 4.12. The most significant differences between the results from the aggregates and the single constituents are the increase in polarization maximums compared to the aggregate results, the decrease in forward scattering as seen at large phase angles, and the increase in the phase law at intermediate phase angles at 452 nm. The decrease in forward scattering is easily explained due to the fact that forward scattering is dependent on the size of the particle and the aggregates are on the order of 10 times larger than the single constituents since they are aggregates of 10 spheres. Generally, however, these two sets of results are very similar and show that small aggregates alone are not really enough to improve the fits nor are they really all that different from a model of the same material but separated into a cloud of spheres. What we are finding here is that aggregates of small particles are necessary to produce large positive polarization maximum near 90° phase angle. This confirms, not only earlier theoretical modeling efforts but also our predictions based on the single scattering information from these targets.

The geometric albedos calculated in the models discussed above are presented in Table 4.3. Comparing these results to those observed for Titan (in Table 4.2) we again notice that the models with larger imaginary indices are more appropriate for Titan as they have lower geometric albedos. Most of these targets, even at the lower limit to the single scattering albedo (and thus the geometric albedo) seem to be too bright suggesting that the imaginary parts of their indices of refractions are not large enough.

Finally, we can discuss trends in the modeling results due to varying particle parameters. Generally, the parameter that most affects the geometric albedo results is the

imaginary part of the refractive index (Toon *et al.* 1992). As the material in the X1-4 aggregate becomes less absorbing, for example, the geometric albedo gets larger. However the number of constituents in an aggregate is here also to be shown to be important in determining the geometric albedo. Comparing the X1-4 constituents with aggregates of them shows that increasing the number of constituents decreases the resulting geometric albedo. In addition, comparing the X3 aggregate (at 648 nm) to the LSA where its index of refraction is similar to that of LSA we can see a further decrease in the geometric albedo as the number of constituents as increased dramatically. While the number of constituents for aggregates of small spheres does affect the geometric albedo, the porosity of aggregates of larger constituents and larger numbers of constituents does not appear to affect it. This is demonstrated by comparing the CYA and the SA which differ in porosity and overall size but not in refractive index or constituent size. The geometric albedo resulting from both of these models are almost identical.

Table 4.3 Geometric albedos computed for single layer model atmospheres.

Target	Geometric albedo range			
0.5" cube	0.64			
1.5" cube	0.61			
CYA	0.60 - 1.45			
SA	0.59 - 1.43			
CA	0.12 - 0.18			
OA	0.06 - 0.12			
LSA	0.20 - 0.42			
LSA blue	0.29 - 0.64			
LSA red	0.31 - 1.15			
	750 nm	648 nm	452 nm	264 nm
X1-X4	0.50	0.41	0.39	0.08
X1-X4 constituents	0.59	0.52	0.34	0.08

Note: The range in computed geometric albedos is due to the uncertainty in the single scattering albedos determined for the laboratory targets. The lower limits for the single scattering albedos produce the lower limits for the geometric albedos in this table.

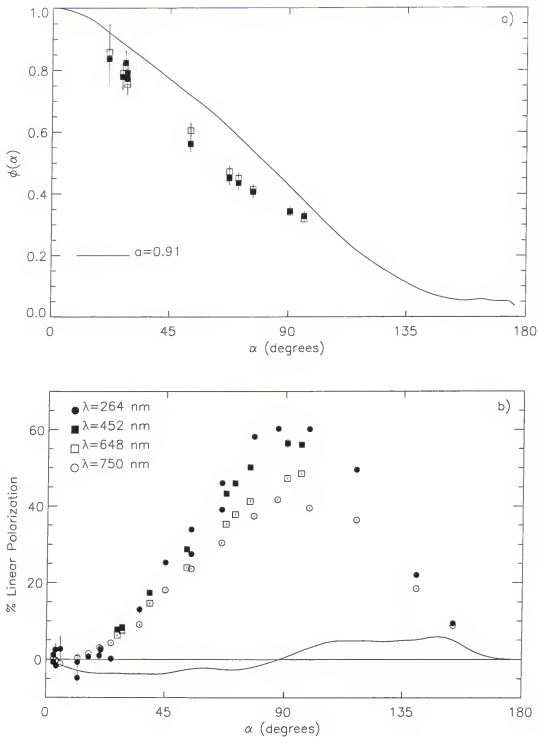


Figure 4.2 0.5'' cube model compared to Pioneer 11 and Voyager 2 photopolarimetry. (a) phase law and (b) polarization versus phase angle for model (line) compared to photopolarimetry (symbols). Where no error bars are shown for the photopolarimetry, the error is smaller than the symbols.

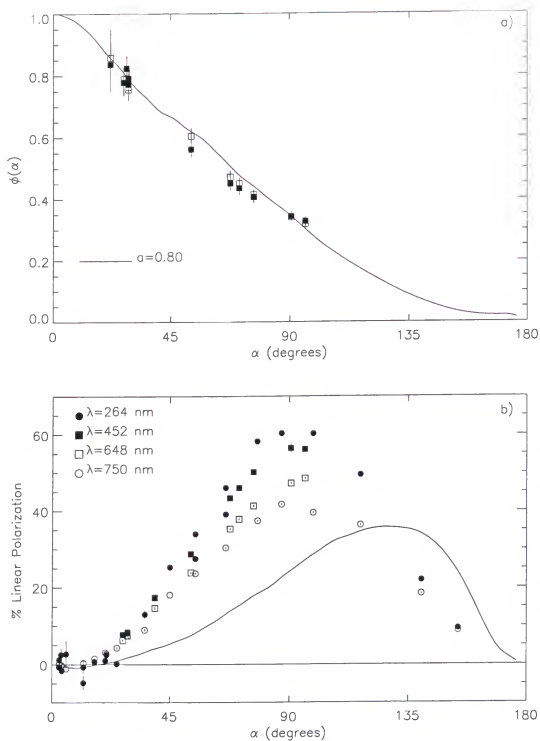


Figure 4.3 1.5'' cube model compared to Pioneer 11 and Voyager 2 photopolarimetry. (a) phase law and (b) polarization versus phase angle for model (line) compared to photopolarimetry (symbols). Where no error bars are shown for the photopolarimetry, the error is smaller than the symbols.

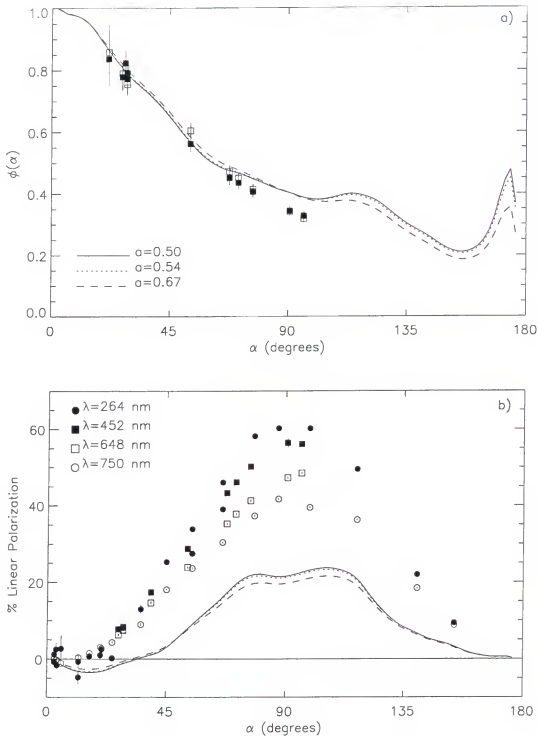


Figure 4.4 OA model compared to Pioneer 11 and Voyager 2 photopolarimetry. (a) phase law and (b) polarization versus phase angle for three single scattering albedos (lines) compared to photopolarimetry (symbols). Where no error bars are shown for the photopolarimetry, the error is smaller than the symbols.

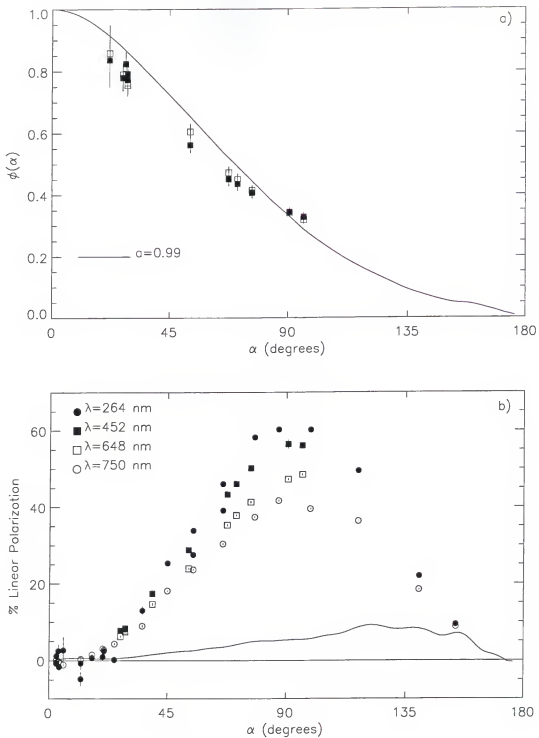


Figure 4.5 CYA model compared to Pioneer 11 and Voyager 2 photopolarimetry. (a) phase law and (b) polarization versus phase angle for CYA model (line) compared to photopolarimetry (symbols). Where no error bars are shown for the photopolarimetry, the error is smaller than the symbols.

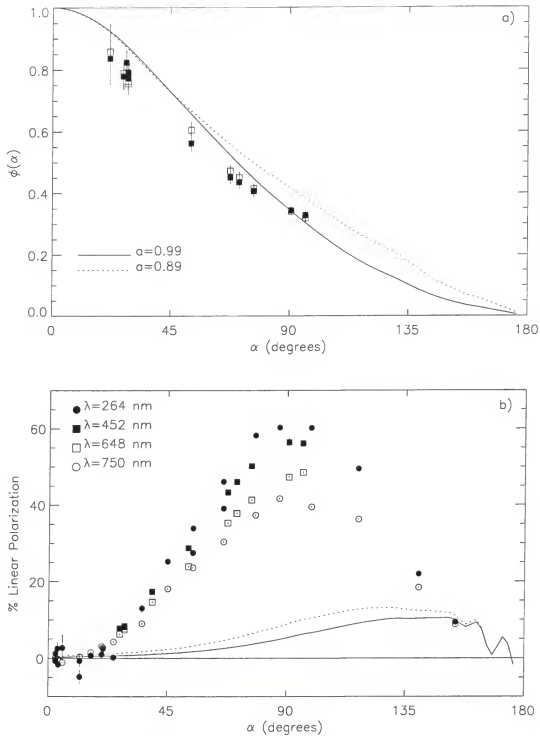


Figure 4.6 SA model compared to Pioneer 11 and Voyager 2 photopolarimetry. (a) phase law and (b) polarization versus phase angle for two single scattering albedos (lines) compared to photopolarimetry (symbols). Where no error bars are shown for the photopolarimetry, the error is smaller than the symbols.

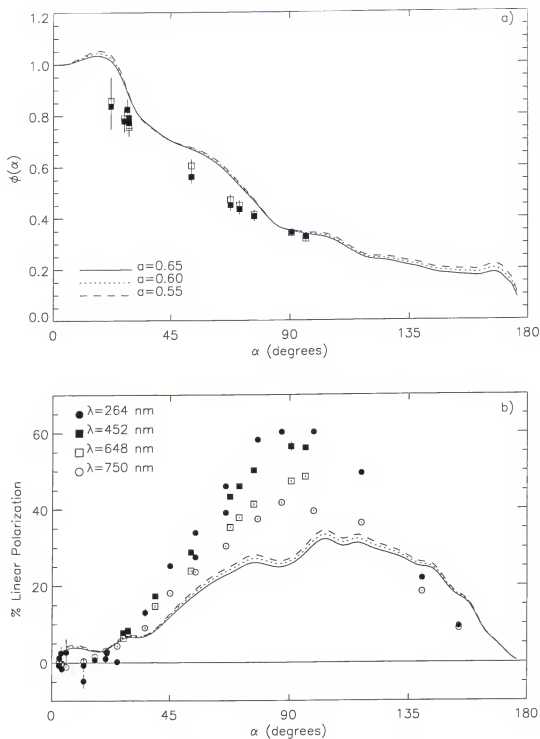


Figure 4.7 CA model compared to Pioneer 11 and Voyager 2 photopolarimetry. (a) phase law and (b) polarization versus phase angle for three single scattering albedos (lines) compared to photopolarimetry (symbols). Where no error bars are shown for the photopolarimetry, the error is smaller than the symbols.

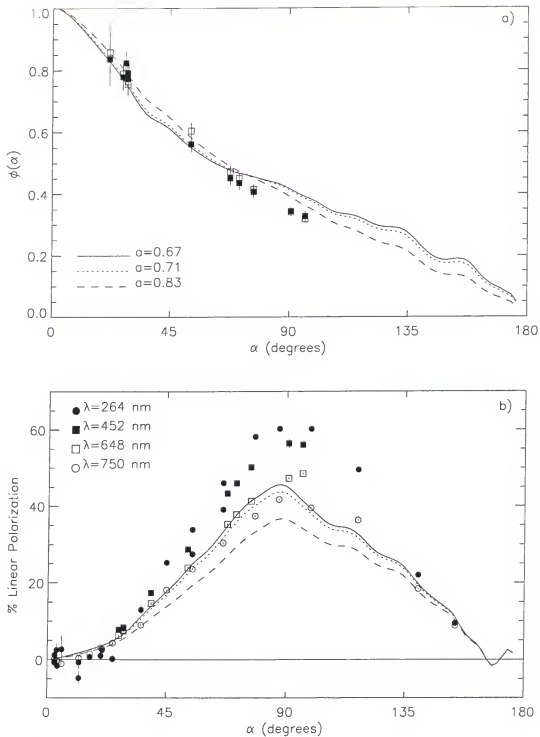


Figure 4.8 LSA model compared to Pioneer 11 and Voyager 2 photopolarimetry. (a) phase law and (b) polarization versus phase angle for three single scattering albedos (lines) compared to photopolarimetry (symbols). Where no error bars are shown for the photopolarimetry, the error is smaller than the symbols.

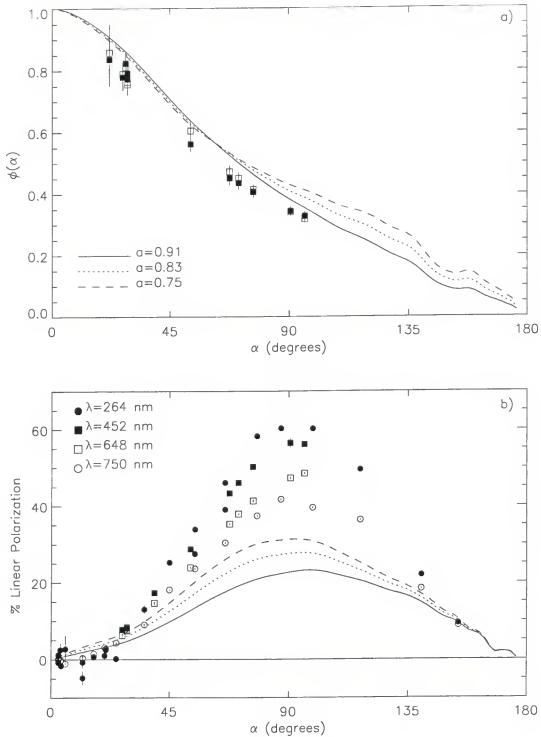


Figure 4.9 LSA blue model compared to Pioneer 11 and Voyager 2 photopolarimetry. (a) phase law and (b) polarization versus phase angle for three single scattering albedos (lines) compared to photopolarimetry (symbols). Where no error bars are shown for the photopolarimetry, the error is smaller than the symbols.

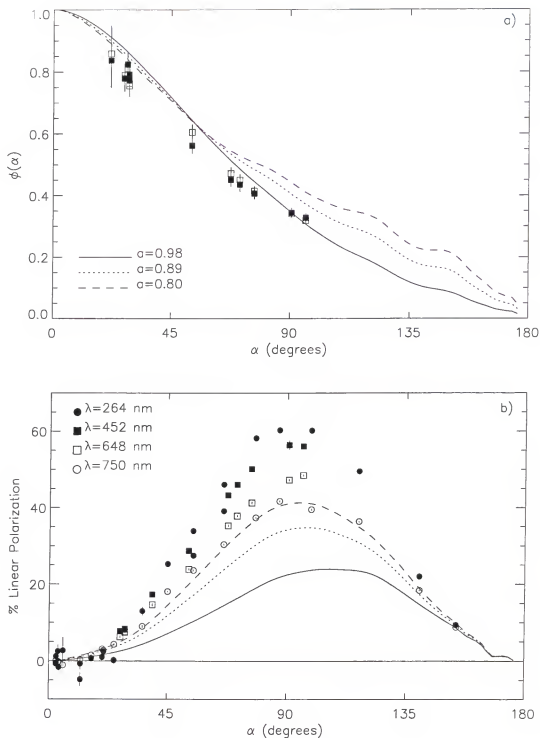


Figure 4.10 LSA red model compared to Pioneer 11 and Voyager 2 photopolarimetry. (a) phase law and (b) polarization versus phase angle for three single scattering albedos (lines) compared to photopolarimetry (symbols). Where no error bars are shown for the photopolarimetry, the error is smaller than the symbols.

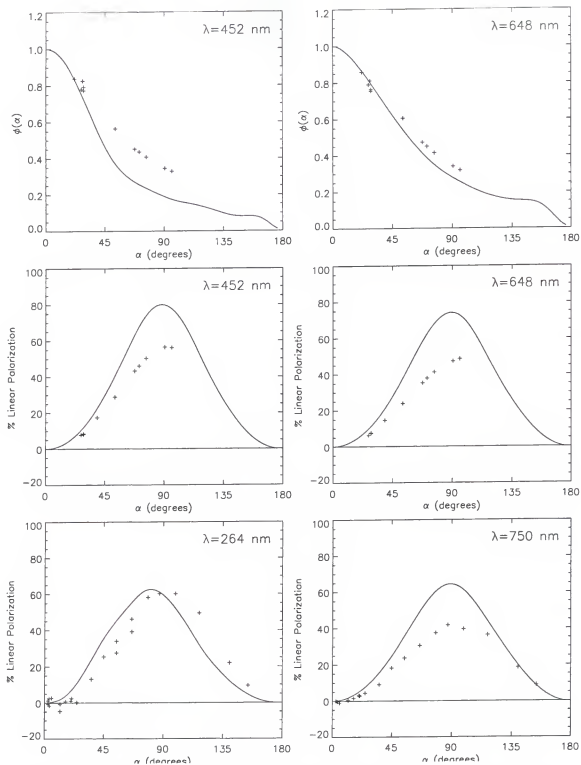


Figure 4.11 X1-X4 models compared to Pioneer 11 and Voyager 2 photopolarimetry. (solid lines) and Pioneer ($\lambda=452$ nm and 648 nm) and Voyager ($\lambda=264$ nm and 750 nm) photopolarimetry (+ symbols). Particle single scattering albedos are: 0.55, 0.60, 0.70, and 0.80 at 264 nm, 452 nm, 648 nm, and 750 nm, respectively.

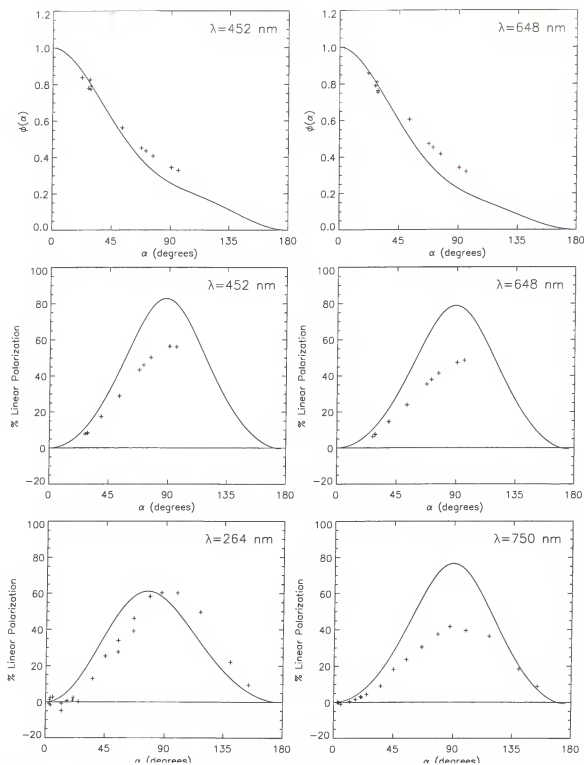


Figure 4.12 Single constituent spheres from the X1-X4 aggregates and photopolarimetry. Particle single scattering albedos are: 0.55, 0.55, 0.60, and 0.65 at 264 nm, 452 nm, 648 nm, and 750 nm, respectively. Lines and symbols are the same as in Figure 4.11.

More Complicated Models

Since we did not find a simple single layer model that is able to reproduce the observations, we can begin to consider additional parameters in our model. While the possible combinations to contemplate are infinite, I have attempted to choose models based on the positive results from the previous section and from which physical insight can be drawn. In this section we will consider models which combine two types of particles (the LSA and X1-4) in two different ways. First we consider a two layer atmosphere in which an optically thin layer of small aggregates (X2) overlies an optically thick layer of larger aggregates (LSA). This situation is appropriate if one considers that the aggregates might be growing as they fall through the atmosphere but is slightly unrealistic in that it does not maintain a continuous aggregate size increase with depth. Next we consider another type of single layer model in which the layer is populated with the same two types of particles in varying proportions. Physically, this represents an atmosphere with a bimodal distribution of aerosols that are not mixed as a function of height in the atmosphere.

The mechanics of creating a two layer model are quite simple. Since the lower layer is an optically thick layer of LSA, we can simply execute the simple single layer LSA model from above with an additional layer of X2 with variable optical depth. Several cases are calculated by varying two parameters, the single scattering albedo, as was done in the single layer models, and the optical depth of the top layer. These two models using the upper and lower limits for the single scattering albedo for the LSA and varying the optical depth of the overlying layer of X2 particles, display the same overall

trend for the smaller single scattering albedo (for the LSA) to fit the polarization (Figure 4.14) better. Beyond this, we can see that a range in optical depth for the X2 layer has a similar effect to a range in single scattering albedo. Increasing the optical depth of this layer increases the overall polarization of the combined model. This is an intuitive result if you consider the large polarization displayed in the optically thick model containing only X2 aggregates (c.f. Figure 4.11 for $\lambda=452$ nm). However, the trend in the phase law is opposite, in that decreasing the optical depth of the overlying layer of X2 aggregates seems to provide a better fit to the observations. This better fit is nevertheless considerably less ideal than that for the polarization.

Table 4.4 Geometric albedos for computed dual layer model atmospheres.

Target	Geometric albedo
LSA ($a=0.67$) + X2 ($\tau=0.1$)	0.26
LSA ($a=0.67$) + X2 ($\tau=0.2$)	0.28
LSA ($a=0.83$) + X2 ($\tau=0.2$)	0.43
LSA ($a=0.83$) + X2 ($\tau=0.4$)	0.43

Note: Comparing these values to those for the LSA single layer model in Table 4.3 we can see that adding a thin layer to the LSA model has a negligible effect on the geometric albedo.

The procedure involved in creating a single layer dual population model is slightly more complicated than that for the two layer case. First we must remember that the scattering matrix for a cloud of particles in random orientation is just the sum of the scattering matrices of the particles in the cloud. Thus, the scattering matrix for a cloud of two different types of particles each in random orientation is just the sum of the individual scattering matrices weighted by the percentage in which they exist in the

cloud. This new scattering matrix must then be fit with a new Legendre polynomial and then the model can be treated like the simple single layer models in the previous section.

An important detail to consider in this type of combination model is how to determine the relative fractions of each type of aggregate that exist in the cloud. Due to the large difference in the overall size of these two aggregates, combining equal numbers of these aggregates will result in the domination of the combined scattering matrix by the LSA. In fact, even a scattering matrix which is made up of 99% X2 and 1% LSA by number will in fact mostly resemble the scattering matrix of the LSA. Therefore, it is important that we start by considering equal volumes of these aggregates. It takes approximately 120 X1-4 aggregates to equal the volume of the LSA aggregate. Based on the results of the equal volume case, the relative population is then be adjusted. Figure 4. shows that a volume mixture of 75% X3 and 25% LSA red is able to match the Pioneer observations at 648 nm quite well. An equally good match to the observations at 452 nm using X2 and LSA blue could not be found. As shown in Figure 4., the polarization is too low if the intensity fits, and as the polarization increases, the intensity becomes too low.

A satisfactory fit to both the red and blue Pioneer photopolarimetry observations simultaneously is obtained by a combination of small spheres and the LSA. Due to the reasonable success discussed above with the X1-4 aggregate I chose to use the constituent spheres in this combination. The physical rationale motivating this model is that the production of aerosols in the atmosphere is a continuous (although possibly with a seasonally variable rate (Hutzell *et al.* 1996)) process. This means that at any given time, the aerosol population should consist of single constituents and aggregates of

varying numbers of these constituents. The single scattering from the LSA constituents is sufficiently similar to that of the constituents in the X1-4 aggregate that they produce an equally satisfactory fit.

As in the case above using two different aggregates, I started with equal volumes of constituents and aggregates and then varied the fractional volumes to find the best match to the observations. I found that a mixture containing 60% X2/3 constituents and 40% LSA provided the best fit at both wavelengths. It is apparent that the 648 nm fit might be improved by increasing the relative proportion of the constituents. However, while such a change may improve the polarization fit at 452 nm, it worsens the phase law fit. While the polarization fit at 648 nm is very good, it is not as good at 452 nm with maximum differences between the observations and the model at about the 3% level. In both cases, however, it appears that the observational polarization peaks lie to higher phase angles than those of the models.

Table 4.5 Geometric albedos for selected single layer combination models.

Target	Geometric albedo
40% LSA red + 60% X3 constituents	0.35
40% LSA blue + 60% X2 constituents	0.28
25% LSA red + 75% X3	0.38
85% LSA blue + 15% X2	0.25
94% LSA blue + 6% X2	0.21

As mentioned previously, it is not possible at this time to obtain the single scattering characteristics of the laboratory targets at both of the Voyager wavelengths due to fact that they are too widely separated to simultaneously fit within the laboratory waveband. It is, however, logical that the combination models discussed in this section

would also improve the fits to the Voyager polarization shown in Figure 4.11 and Figure 4.12 using the $X_{1/4}$ aggregates and constituents respectively. In the UV, such a combination would act to centralize the polarization peak although it may have the undesirable effect to decrease it as well. Since the imaginary part of the index of refraction of tholins decreases significantly at wavelengths larger than 700nm, the fit at 750 nm might be improved if one considers that at this wavelength the atmosphere might not be optically thick and the surface may serve to reduce the overall polarization seen at NIR wavelengths. The surface has in fact been seen at wavelengths longer than 890 nm (Smith *et al.* 1996). But the question remains as to the optical thickness of the atmosphere at 750 nm and thus whether the surface does in fact have effect on the polarization here.

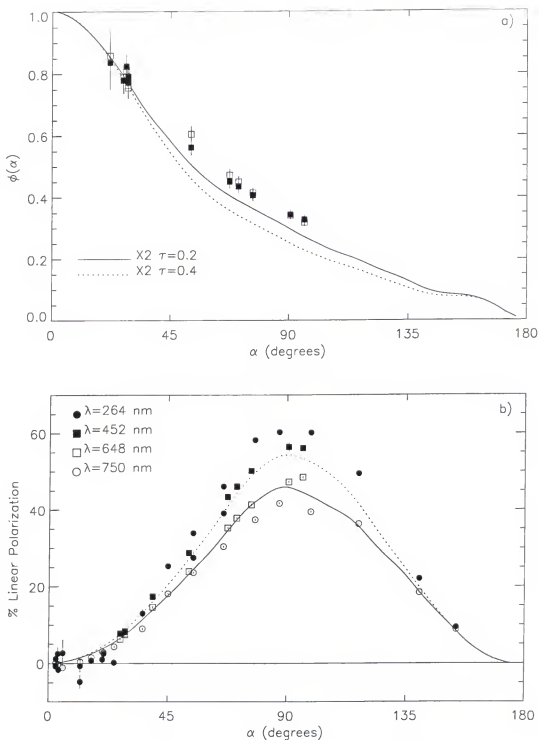


Figure 4.13 LSA and X2 combination model compared to photopolarimetry. (a) phase law and (b) polarization versus phase angle for two different optical depths of X2 overlying optically thick layer of LSA with single scattering albedo of 0.83 (lines) compared to photopolarimetry (symbols). Where no error bars are shown for the photopolarimetry, the error is smaller than the symbols.

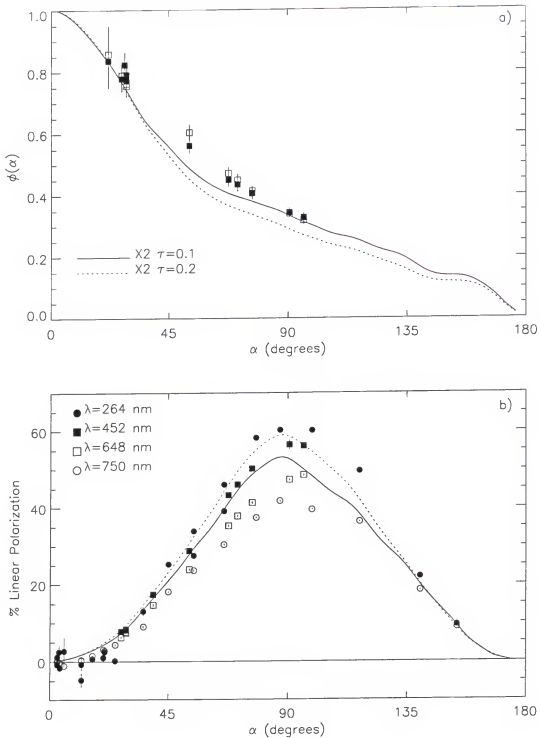


Figure 4.14 Another LSA and X2 combination model compared to photopolarimetry. (a) phase law and (b) polarization versus phase angle for two different optical depths of X2 overlying optically thick layer of LSA with single scattering albedo of 0.67 (lines) compared to photopolarimetry (symbols). Where no error bars are shown for the photopolarimetry, the error is smaller than the symbols.

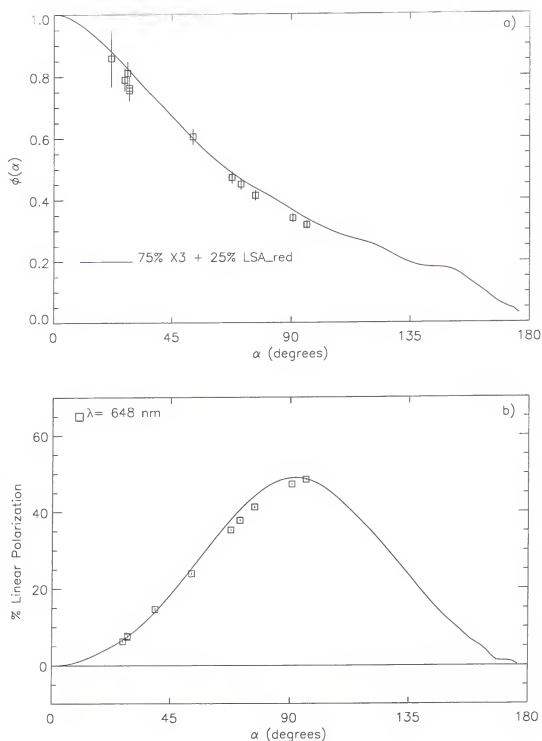


Figure 4.15 Single layer combination of LSA red and X3 compared to photopolarimetry. (a) phase law and (b) polarization versus phase angle for a mixture of 75% X3 and 25% LSA red (solid line) compared to photopolarimetry at 648 nm (boxes). Where no error bars are shown for the photopolarimetry, the error is smaller than the symbols.

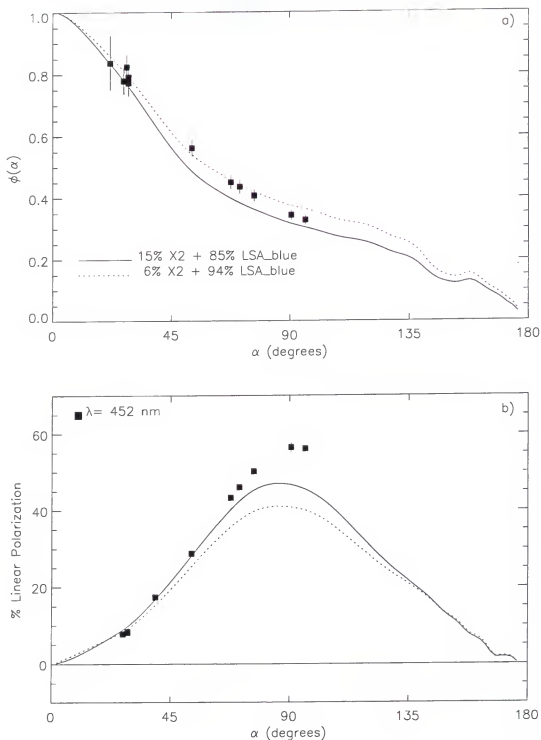


Figure 4.16 Single layer combination of LSA blue and X2 compared to photopolarimetry. (a) phase law and (b) polarization versus phase angle for a mixture of 15% X2 and 85% LSA blue (solid line) and a mixture of 6% X2 and 94% LSA blue (dotted line) compared to photopolarimetry at 452 nm (boxes). Where no error bars are shown for the photopolarimetry, the error is smaller than the symbols.

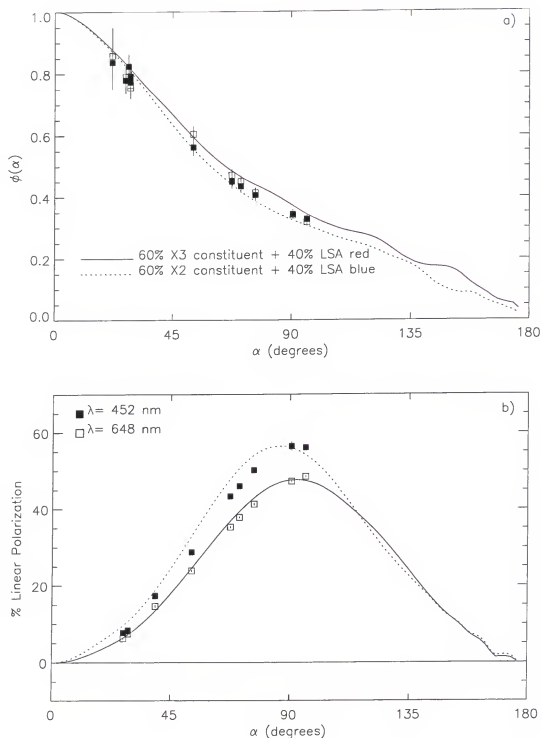


Figure 4.17 Best fit model atmosphere containing 60% X2/3 constituents and 40% LSA. (a) phase law and (b) polarization versus phase angle for single layer combination model at 648 nm and 452 nm (solid and dotted line respectively) compared to photopolarimetry at 648 nm and 452 nm (open and closed squares respectively). Where no error bars are shown for the photopolarimetry, the error is smaller than the symbols.

Possible Applications to Cassini

The Huygens probe, which will be released from the Cassini orbiter to plunge into Titan's atmosphere in November of 2004, contains an instrument called the Descent Imager/Spectral Radiometer (DISR). Among the DISR's scientific objectives, is the determination of the optical properties of the aerosols and cloud particles and their vertical distribution within the atmosphere. One of its detectors, the Solar Aureole camera, will measure the intensity and polarization in two colors (green, 500nm, and near IR, 935 nm) of the forward (zenith angles, $\theta=25-75^\circ$ in the sunward direction with azimuth, $\phi\sim 0^\circ$ representing scattering angles, $\Theta=0-25^\circ$) and side (zenith angles, $\theta=25-75^\circ$ in the anti-sunward direction with azimuth, $\phi\sim 180^\circ$ representing scattering angles, $\Theta=75-125^\circ$) scattered light from the atmosphere above the spacecraft. Differencing sequential measurements will isolate the radiation from just the 2 km layer above the probe in order to reduce the effect of multiple scattering and retrieve single scattering particle characteristics (Tomasko *et al.* 1997).

In that case, we can make the following prediction based on the best fit combination model in the previous section. The single scattering properties of the 60/40 case above have been recalculated at a wavelength that will be examined by DISR, 500 nm, and are shown below in Figure 4.18.

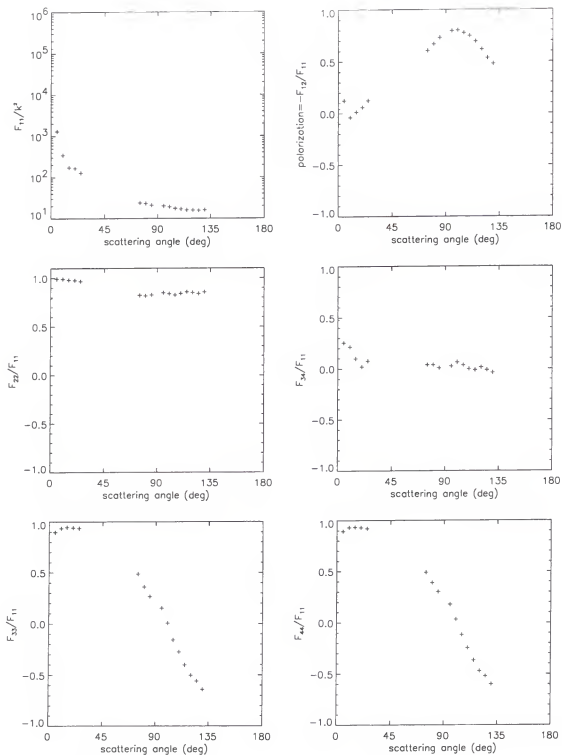


Figure 4.18 DISR prediction based on 60/40 combination model at 500 nm. Scattering matrix elements for a cloud with a 60/40 mix of small spheres and LSA's plotted at the scattering angles at which the DISR will make measurements.

Another application to Cassini comes out of the small discrepancy seen in Figure 4.17 for the polarization at the Pioneer blue wavelength. It raises the question of precisely at which phase angle the polarization peaks. Generally spheres and aggregates of spheres do not have their polarization peaks shifted to higher phase angles/lower scattering angles but rather as small spheres approach a size parameter of one their polarization peaks are shifted in the opposite direction to lower phase angles/higher scattering angles. Thus, if the very small shift to higher phase angles seen in the incomplete polarization curves of the Pioneer observations is in fact confirmed by Cassini, this could be indicative that another type of particle exists there. Examples of particles which have peaks shifted to lower phase angles include cubes (as shown by the 1.5'' cube), compact aggregates, and thin flakes (Waldemarsson and Gustafson 2000; Zakharova and Mishchenko 2001).

Conclusions

This is the only study to compare Titan's photopolarimetry to radiative transfer modeling using measured scattering properties. The models are done in a consistent manner so that the only parameter changed is the particles which make up the atmosphere. The result is meaningful comparisons between a variety of single particle atmospheres without non-physical assumptions.

Table 4.6 Summary of selected model results and Titan's observed characteristics.

Object	Intensity			Polarization	
	color ¹	Forward scattering, R_{90} ²	phase law slope ^{3,4}	PC	P_{\max} ⁴
Titan	red	7.2 ± 1 ⁵	$[-0.007, -0.008]$	blue	40-60%
LSA	red	6.0	$[-0.006, -0.008]$	red	25-45% ⁶
X1-X4	red	5.9	$[-0.008, -0.009]$	blue ⁷	60-80%
40/60 combo	red	3.4	$[-0.007, -0.008]$	blue	40-60%

Note: PC refers to polarimetric color and P_{\max} refers to the maximum in the polarization curve.

The LSA target provides the best fit to the photopolarimetry of all of the targets measured in the microwave analog laboratory. This being said it is certainly not an ideal fit and has the following problems: opposite trend with single scattering albedo for polarization and phase law which leads to diverging fits to both sets of data, polarimetric color due to scattering alone shows the wrong trend. The small aggregate model, X1-X4, which is most similar to that used in previous investigations while providing some of the characteristics needed to match the data is also not an ideal candidate. But both of these models show us that aggregates of small particles are necessary to produce the large positive polarization maximum near 90° phase angle. This confirms, not only earlier theoretical modeling efforts but also our predictions based on the single scattering information from these targets.

¹ Obtained from geometric albedo observations or model results

² Obtained from table 2.12 in Chapter 2 for blue laboratory wavelength which is the closest to the Voyager violet (420 nm) images.

³ Slope of phase law (which is by definition normalized to $\Theta=180$) between $\Theta=85$ -150° (or $\alpha=20$ -95°).

⁴ Range of values also due color as well as to uncertainty in single scattering albedo.

⁵ Obtained from H-G and Rayleigh combination model fits to Voyager high phase angle image observations at 420 nm (c.f. R_{90} the section entitled Single Scattering and Titan in Chapter 2).

⁶ Range of values also due to color as well as uncertainty in single scattering albedo.

⁷ Except polarization at 264 nm is 25% smaller than at 452 nm so blue trend is broken (c.f. Figure 4.11).

It thus appears that these two models may bracket the type of particle we could expect to find in the Titanian atmosphere. This bracketing occurs both in the physical description of the models, in the sense that the LSA is a larger version of the X1-X4 aggregate, and in the modeling results as the X1-X4 generally shows an excess of polarization and a paucity of intensity at intermediate phase angles whereas the LSA shows a dearth of polarization and a surplus of intensity at intermediate phase angles. Pure Rayleigh polarization (that from very small particles) is not depolarized enough by multiple scattering effects to produce the polarization maximums between 40 and 60% as seen in the in Titan polarimetry. Small aggregates of Rayleigh like (read small) particles show no significant difference from unaggregated small particles in polarization signature. When the aggregates are much larger (i.e. with many more constituents) the polarization maximum is decreased significantly. So it would seem that a happy medium needs to be approached.

Having achieved agreement between a combination model and observations, we are able to suggest a characterization of Titan's aerosols that is somewhat different from models previously proposed. This is important because the size of the aggregates in the previous models were limited to small aggregates and thus this is the first model using significantly larger aggregates to fit the observations. The caveat here is uniqueness. Due especially to the fact that the best fit is achieved with a combination model, one could argue that there may be other combinations that work equally well. Finding a single particle with scattering characteristics that match those of the combination is not necessarily the solution to this problem. First, there is no guarantee that there is only one such particle. Secondly, since we have narrowed down our search to aggregates, this

begs the question: is a single size aggregate really a plausible outcome in an atmosphere that is continually producing aerosols? This suggests that it may be necessary to measure or calculate the scattering from a cloud of a size distribution of aggregates (and possible constituents).

In previous works, very small aggregates (similar to X1-X4) were used with the non-physical assumption that the real and imaginary indices of refraction can be parameterized independently to fit the observations. Furthermore, additional atmospheric (as opposed to particulate) parameters were introduced in the modeling i.e. surface conditions or a bimodal particle population seen only at certain wavelengths. The goal of the present work, to directly constrain aerosol physical characteristics, is addressed by studying in a consistent manner how a variety of particle morphologies affect polarization and intensity measurements of Titan's atmosphere. This type of investigation yields results that help us understand the complicated problem of retrieving aerosol properties based on observations of multiple scattering by an atmosphere of non-spherical particles. In summary we suggest, based on the results for the ten particle models discussed, that the aerosols in Titan's atmosphere have characteristics between or in combination of those of the LSA and X1-X4 aggregate and constituents.

Future Work

The combination of experimental single scattering measurements with theoretical radiative transfer modeling efforts has been shown to be a fruitful endeavor. The power of this method will become evident with application to the higher quality data from the upcoming Cassini/Huygens encounter with Titan in 2004. In the following sections are

some of my ideas for improving this type of analyses as well as some suggestions for other types of particles that may be worth exploring and further ways to more accurately portray the Titanian atmosphere.

Single Scattering Issues

Extinction measurements require special procedures and are time consuming due to the large background signal in the forward direction and the necessity of phase calibration. In order to properly perform these type of measurements precise positioning of the target is necessary. Thus for many orientations this becomes time-consuming and therefore was not included in this investigation. But it may eventually be worthwhile to explore this as it may possible to achieve uncertainties smaller than 10% in the measured single scattering albedos (Gustafson 2000). This would allow better determinations of the single scattering albedo and reduce the uncertainty in the model calculations as well as allowing determination of the absorption efficiency and thus the study of atmospheric heating due to the aerosols.

While we are putting things on our wish list it would be interesting to consider chemical simulations (like those of Bar-Nun *et al.* (1988), Clarke and Ferris (1997), and Scattergood *et al.* (1992)) including light scattering instrumentation. This would provide a considerably more direct method of obtaining the single scattering characteristics of the types of particles produced in environments as close to those existing in the Titanian atmosphere as we can generate here on Earth. The problem of finding materials with indices of refraction in the microwave region corresponding to our desired visual indices of refraction (that are based on measurements of material created in these types of

chemical simulations) could be avoided. However, designing light scattering experiments which work at visible wavelengths is not without its own set of challenges.

Other Types of Models to Consider

Based on the concept that two of the targets considered in this study (the LSA and X1-X4) appear to bracket the particle we are looking for, I propose studying aggregates which are intermediate in size between these two models. Such aggregates have been studied and single scattering intensities and polarizations have been published (Zerull *et al.* 1993). Also, Dr. Y.-L. Xu's code for calculating the scattering by an aggregate of spheres has recently become publicly available and would handle aggregates at the smaller end of the bracket.

There are physical arguments (Rannou *et al.* 1995) for suggesting that the particles in the atmosphere of Titan have a size distribution and/or a number density that increases (or at least changes) with optical depth. Incorporating this in the modeling process is not at all an insignificant task. If each laboratory frequency were considered a size (as in our simulation of a size distribution in Chapter 3) then we could simulate up to 85 layers each populated with particles of increasing size. In order to do this, the scattering matrix for each of the 85 frequencies would need to be fit with its own set of Legendre polynomials as input to the radiative transfer modeling and of course adding additional layers to the radiative transfer calculations makes them take longer. Simulating an increasing number density of the same particles would not be as difficult, but being poorly constrained may require trying many different functional forms for the number density with altitude.

APPENDIX A RADIUS OF GYRATION

The radius of gyration is the distance between an object's center of mass and the point at which if all the mass in the object were concentrated, the moment of inertia (about a principle axis through the center of mass) for this point mass would be the same as the original object. It is a measure of the effective mass distribution and an indicator of an object's resistance to rotation. Given the same mass, an object with a small radius of gyration will have smaller moment of inertia than an object with a larger radius of gyration.

The radius of gyration for an aggregate, R_g , is given by

$$R_g = \sqrt{\frac{\sum_{i=1}^N m_i r_i^2}{\sum_{i=1}^N m_i}}, \quad (\text{A.1})$$

where m_i and r_i are the mass and distance from the center of mass (defined at the origin for convenience) of the i th constituent. If all of the constituents have the same mass, then equation (2.1) reduces to

$$R_g = \frac{1}{N} \sqrt{\sum_{i=1}^N r_i^2}. \quad (\text{A.2})$$

In order to determine the radius of gyration of an aggregate, a quantity which is dependent on the three-dimensional positions of the constituents, from an image of the aggregate, it is helpful to use the concept of area radius of gyration. Area moment of inertia and area radius of gyration are concepts used in structural analysis (of support

beans for example) in mechanical engineering. Their definitions are similar to those above except an objects area is replaced with a “line area” rather than an objects mass being replaced with a point mass. The equivalent definition to equation (2.19) for the area radius of gyration is

$$R_g = \sqrt{\frac{\sum_{i=1}^N G_i r_i^2}{\sum_{i=1}^N G_i}} \quad (\text{A.3})$$

where G_i and r_i are the cross sectional area and distance from the axis about which the radius of gyration is being determined for the i th constituent. Again, given identical constituents this reduces to equation (2.20).

In the case of an aggregate, the area radius of gyration around the axis pointing out of the image plane is equal to the mass radius of gyration for the same axis. First consider an aggregate with its center of mass at the origin of a Cartesian coordinate system. Its radius of gyration about the z axis, according to equation (2.11), is

$$R_{gz} = \frac{1}{N} \sqrt{\sum_{i=1}^N x_i^2 + y_i^2} \quad (\text{A.4})$$

where $r_i^2 = x_i^2 + y_i^2$ is the distance of the i th constituent from the z axis. Now consider a cross sectional view in the x-y plane of the same aggregate considered above.

Thus the radius of gyration (about the axis through the centroid of the aggregate out of the plane of the image) can be determined from an image of an aggregate by

$$R_g^2 = \frac{1}{G} \sum_{x', y' \in \text{target}} (x' - x_c)^2 + (y' - y_c)^2, \quad (\text{A.5})$$

where G is the cross sectional area of the image of the target and x_c and y_c are the x and y coordinates of the center of the area given by

$$x_c = \frac{1}{G} \sum_{x', y' \in \text{target}} x' \quad \text{and} \quad y_c = \frac{1}{G} \sum_{x', y' \in \text{target}} y' . \quad (\text{A.6})$$

The moment of inertia for a homogeneous sphere with mass M and radius R is $I = \frac{2}{5}MR^2$ and its radius of gyration is $R_g = \frac{2}{5}R^2$. The radius of a homogeneous sphere with a radius of gyration equal to that of an aggregate, termed effective radius, R_{eff} , is then defined as:

$$R_{\text{eff}} = \sqrt{\frac{5}{2}} R_g . \quad (\text{A.7})$$

APPENDIX B EXPANSION OF THE SCATTERING MATRIX

As discussed in Chapter 3, rt3 uses the Legendre series representation of the scattering matrix as input. The scattering matrix as a function of $\cos\Theta$ can be expanded as shown here:

$$F_{ij}(\Theta) = \sum_l \xi_{ij}^l P^l(\cos\Theta), \quad (\text{B.1})$$

where P^l are the Legendre Polynomials of degree l . The expansion coefficients ξ^l are found using

$$\xi_{ij}^l = (l + \frac{1}{2}) \int_{-1}^1 F_{ij}(\Theta) P^l(\cos\Theta) d(\cos\Theta). \quad (\text{B.2})$$

Comparison of Legendre Polynomials to Laboratory Data

The figures below show the scattering matrices calculated from the laboratory data integrated over the entire laboratory waveband compared to the sum of the Legendre Polynomial series used to represent it in the radiative transfer modeling.

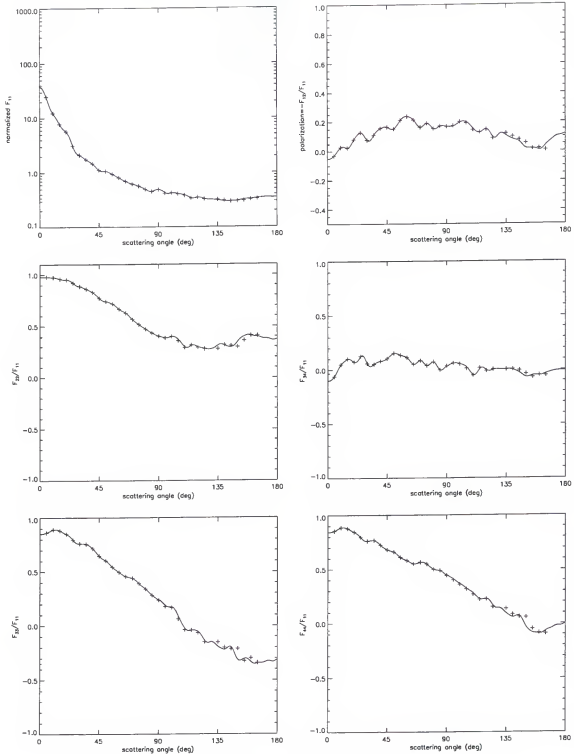


Figure B.1 Scattering matrix elements for the CYA and the Legendre Series fits. Measured values (represented with + symbols) are integrated over the entire laboratory waveband. The solid line represents the calculated sum of the series of Legendre polynomials.

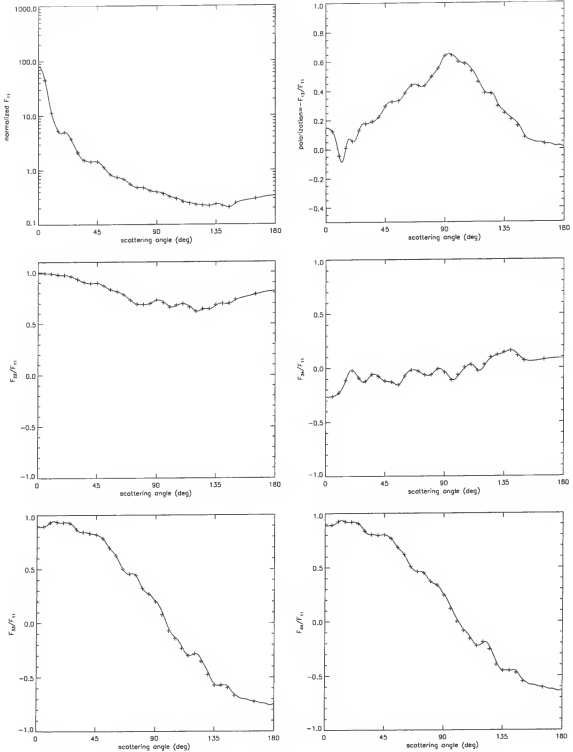


Figure B.2 Scattering matrix elements for the LSA and the Legendre Series fits. Measured values (represented with + symbols) are integrated over the entire laboratory waveband. The solid line represents the calculated sum of the series of Legendre polynomials.

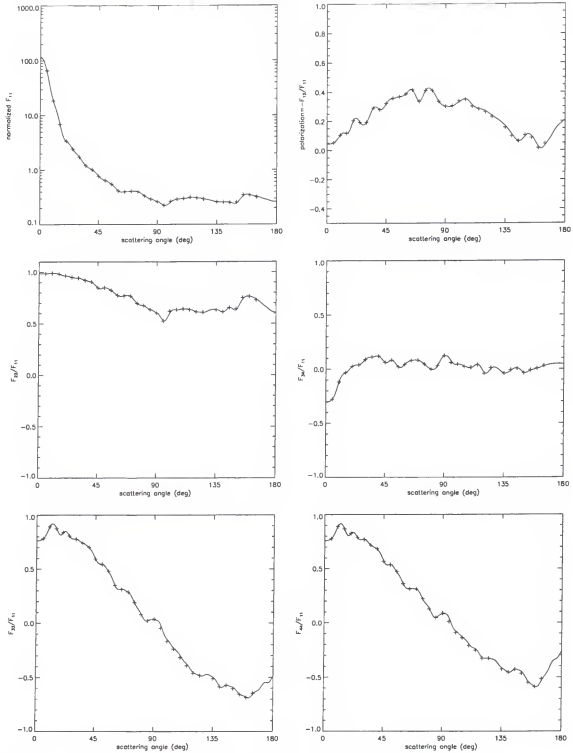


Figure B.3 Scattering matrix elements for the CA and the Legendre Series fits. Measured values (represented with + symbols) are integrated over the entire laboratory waveband. The solid line represents the calculated sum of the series of Legendre polynomials.

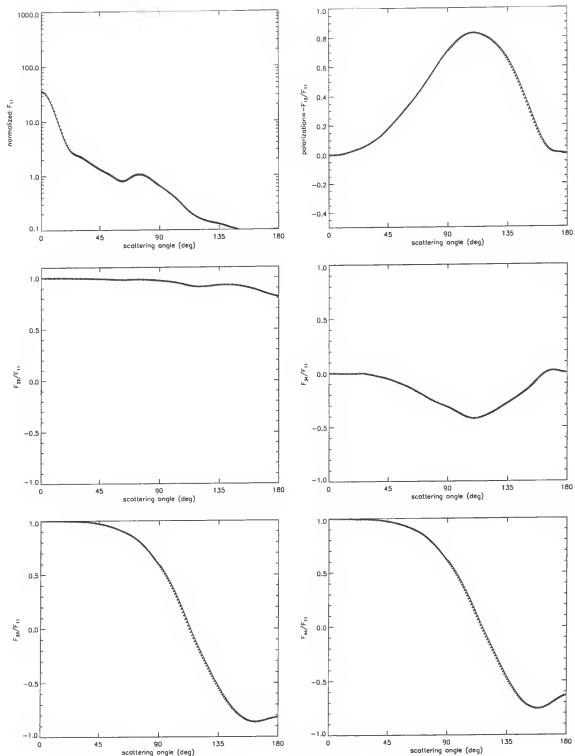


Figure B.4 Scattering matrix elements for the X1 and the Legendre Series fits. Measured values (represented with + symbols) are integrated over the entire laboratory waveband. The solid line represents the calculated sum of the series of Legendre polynomials.

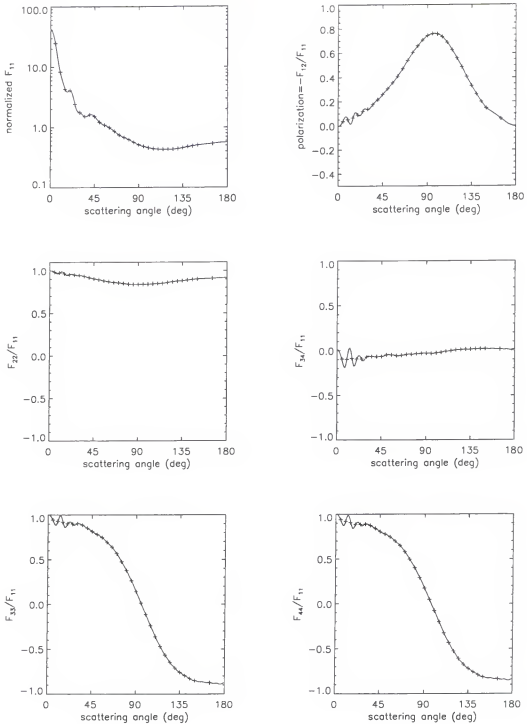


Figure B.5 Scattering matrix elements for the 60/40 mix of X2 constituents and LSA blue and the Legendre Series fits.

Measured values (represented with + symbols) are integrated over the entire laboratory waveband. The solid line represents the calculated sum of the series of Legendre polynomials.

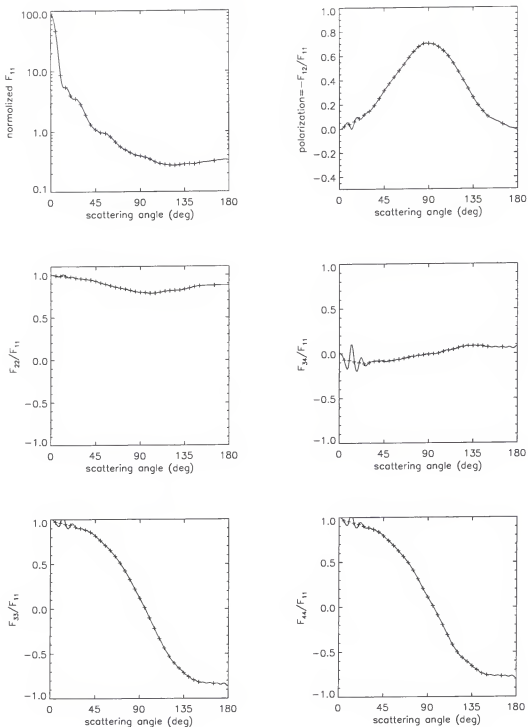


Figure B.6 Scattering matrix elements for the 60/40 mix of X3 constituents and LSA red and the Legendre Series fits.

Measured values (represented with + symbols) are integrated over the entire laboratory waveband. The solid line represents the calculated sum of the series of Legendre polynomials.

Comparison of Legendre Polynomials to Smoothed Laboratory Data

In some cases, the laboratory data give rise to Legendre Polynomials that are unrealistic in their extrapolated backscattering regions (c.f. Figure B.7). In order to correct the Legendre Polynomial fits for these targets, the laboratory scattering matrix data is smoothed (except at forward scattering angles where smoothing creates unrealistic profiles) before the Legendre coefficients are determined.

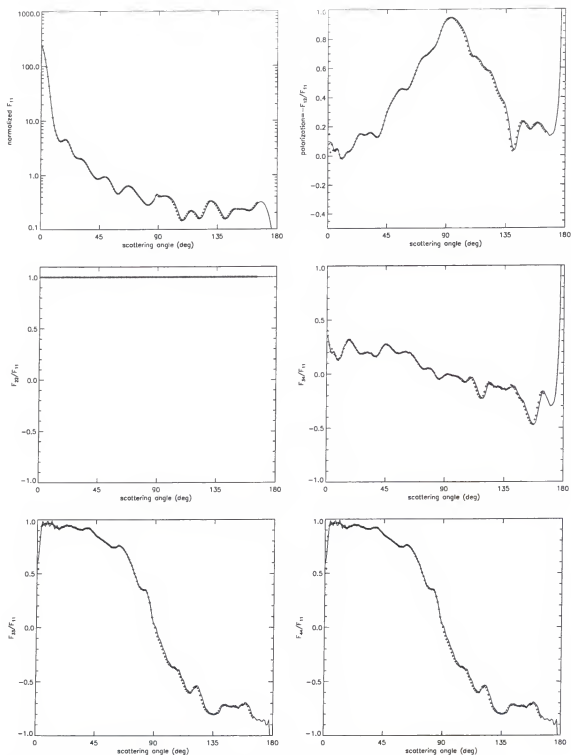


Figure B.7 Example of Legendre series fit for the unsmoothed LSA data in blue waveband. Measured values (represented with + symbols) are integrated over the entire laboratory waveband. The solid line represents the calculated sum of the series of Legendre polynomials.

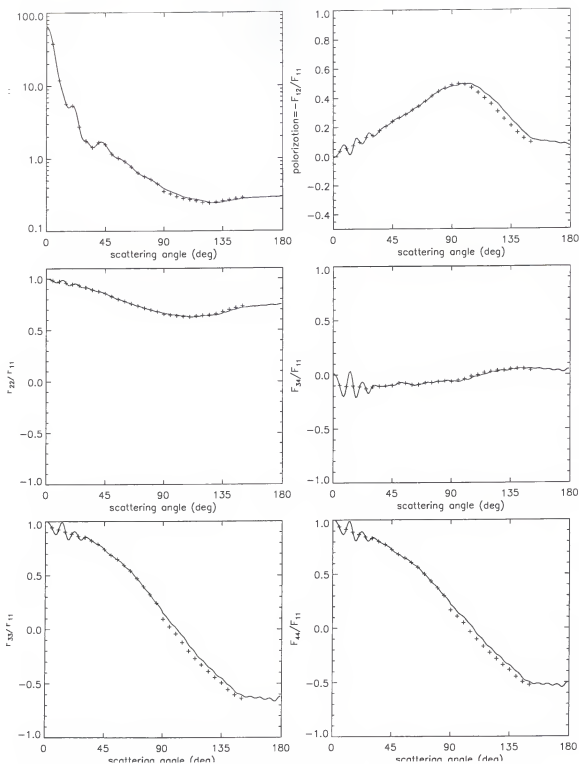


Figure B.8 Scattering matrix elements for the smoothed LSA data in blue waveband. Measured values (represented with + symbols) are integrated over the entire laboratory waveband. The solid line represents the calculated sum of the series of Legendre polynomials.

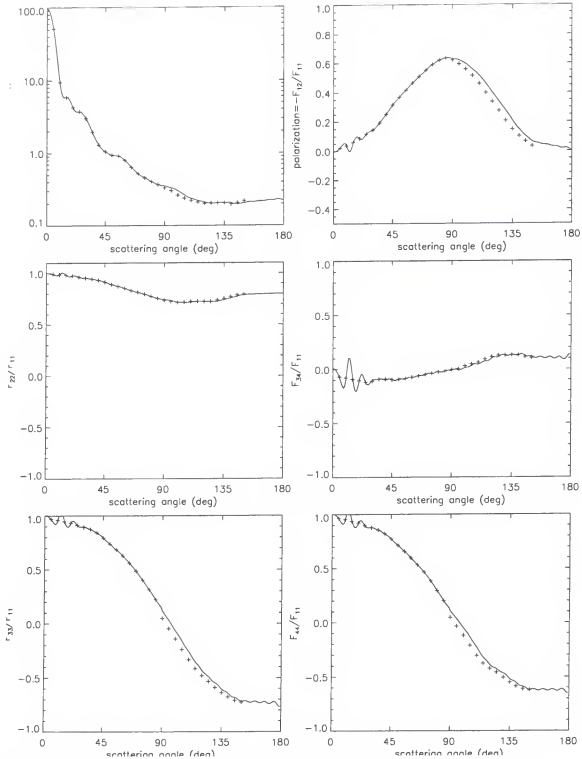


Figure B.9 Scattering matrix elements for the smoothed LSA data in red waveband. Measured values (represented with + symbols) are integrated over the entire laboratory waveband. The solid line represents the calculated sum of the series of Legendre polynomials.

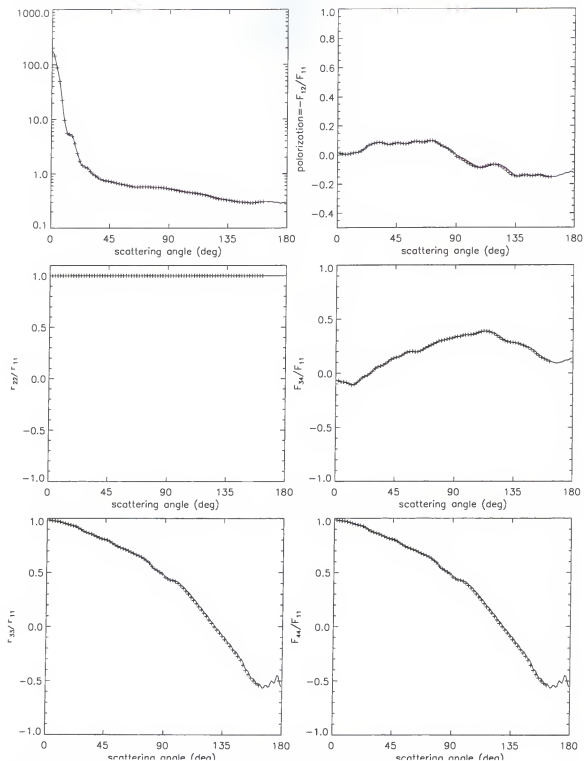


Figure B.10 Scattering matrix elements for the smoothed 0.5'' cube data.

Measured values (represented with + symbols) are integrated over the entire laboratory waveband. The solid line represents the calculated sum of the series of Legendre polynomials.

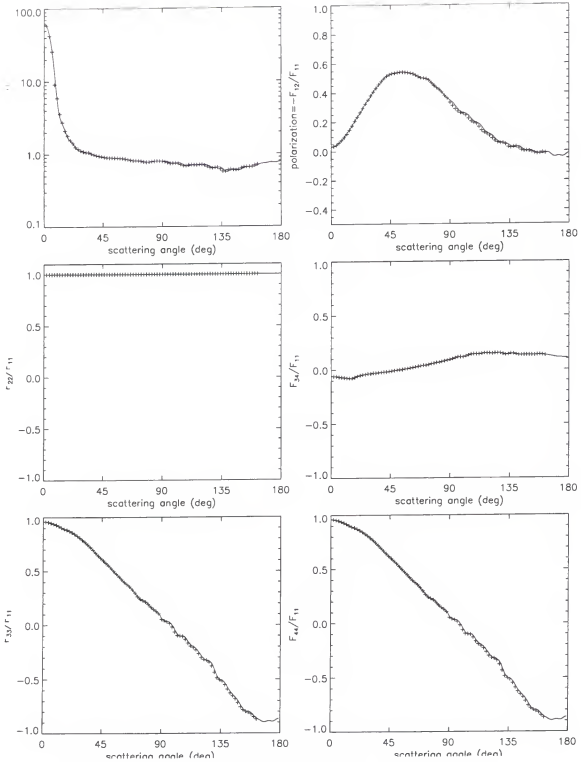


Figure B.11 Scattering matrix elements for the smoothed $1.5\mu\text{m}$ cube data. Measured values (represented with + symbols) are integrated over the entire laboratory waveband. The solid line represents the calculated sum of the series of Legendre polynomials.

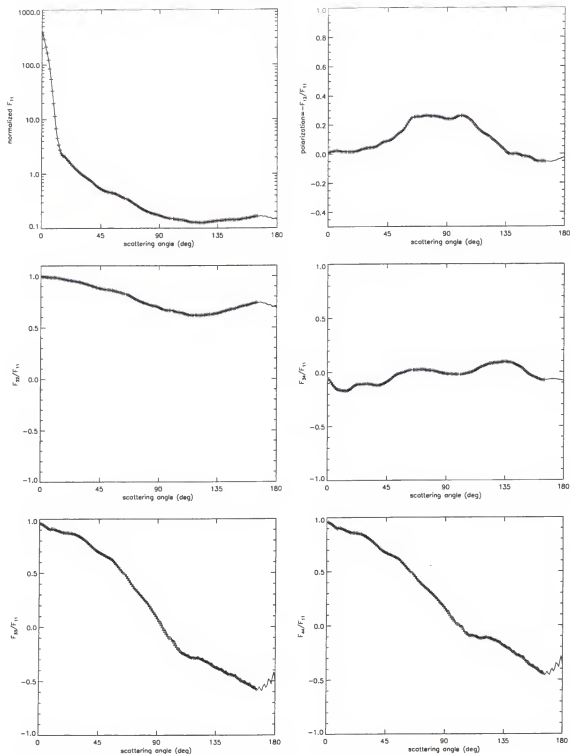


Figure B.12 Scattering matrix elements for the smoothed OA data. Measured values (represented with + symbols) are integrated over the entire laboratory waveband. The solid line represents the calculated sum of the series of Legendre polynomials.

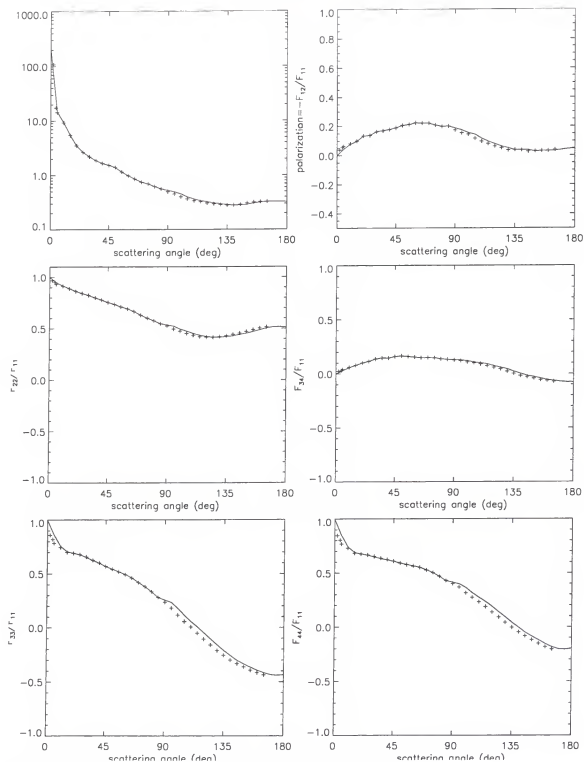


Figure B.13 Scattering matrix elements for the smoothed SA data.

Measured values (represented with + symbols) are integrated over the entire laboratory waveband. The solid line represents the calculated sum of the series of Legendre polynomials.

APPENDIX C

INCLUSION OF THE FULL SCATTERING MATRIX IN RADIATIVE TRANSFER CALCULATIONS

This appendix elucidates the necessity of using the entire scattering matrix in radiative transfer calculations due to the rotation of the Stokes vectors that occurs when many scattering planes must be considered. The four top, left corner elements of the scattering matrix, sufficient for single scattering of unpolarized incident radiation, are not sufficient for full radiative transfer applications. To see why this is true we consider a simple formulation of scattering events.

Given a scattering matrix in the form of equation (2.11) and incident stokes vector, $\mathbf{I}_o = [1 \ 0 \ 0 \ 0]^T$, the singly scattered Stokes vector (disregarding certain multiplicative factors) has the form

$$\mathbf{I}_1 \propto \mathbf{F} \cdot \mathbf{I}_o = \begin{pmatrix} a_1 & b_1 & 0 & 0 \\ b_1 & a_2 & 0 & 0 \\ 0 & 0 & a_3 & b_2 \\ 0 & 0 & -b_2 & a_4 \end{pmatrix} \cdot \begin{pmatrix} 1 \\ 0 \\ 0 \\ 0 \end{pmatrix} = \begin{pmatrix} a_1 \\ b_1 \\ 0 \\ 0 \end{pmatrix}. \quad (\text{C.1})$$

Considering this as the incident radiation on another particle in the scattering plane, we can write the doubly scattered Stokes vector as

$$\mathbf{I}_2 \propto \mathbf{F} \cdot \mathbf{I}_1 = \begin{pmatrix} a_1 & b_1 & 0 & 0 \\ b_1 & a_2 & 0 & 0 \\ 0 & 0 & a_3 & b_2 \\ 0 & 0 & -b_2 & a_4 \end{pmatrix} \cdot \begin{pmatrix} a_1 \\ b_1 \\ 0 \\ 0 \end{pmatrix} = \begin{pmatrix} a_1^2 + b_1^2 \\ a_1 b_1 + a_2 b_1 \\ 0 \\ 0 \end{pmatrix}. \quad (\text{C.2})$$

We can see from this type of analysis that successive scatterings will only lead to further complication of the top two elements of the resulting Stokes vector depending only on the four top left corner elements in the scattering matrix and thus in this case (one scattering plane) the rest of the scattering matrix can legitimately be neglected. If, however, we are interested in the more general case depicted in Figure 3.3 where radiation outside the scattering plane is important then a rotation matrix must be included in the above analysis.

The rotation matrix accounts for the fact that the reference plane for the scattering matrix, and thus the Stokes vectors calculated from it, is the scattering plane. As discussed in Chapter 3, the phase matrix used in radiative transfer calculations is simply a rotated version of the scattering matrix due to the fact that the Stokes vectors are referred to meridional planes (defined by zenith and azimuth angles) in the atmosphere. In this case, equation (C.1) becomes:

$$\mathbf{I}_1 \propto \mathbf{P} \cdot \mathbf{I}_0 = \begin{pmatrix} a_1 & b_1 C_1 & b_1 S_1 & 0 \\ b_1 C_2 & a_2 C_1 C_2 - a_3 S_1 S_2 & a_2 S_1 C_2 + a_3 C_1 S_2 & b_2 S_2 \\ -b_1 S_2 & -a_2 C_1 S_2 - a_3 S_1 C_2 & -a_2 S_1 S_2 + a_3 C_1 C_2 & b_2 C_2 \\ 0 & b_2 S_1 & -b_2 C_1 & a_4 \end{pmatrix} \cdot \begin{pmatrix} 1 \\ 0 \\ 0 \\ 0 \end{pmatrix} = \begin{pmatrix} a_1 \\ b_1 C_2 \\ -b_1 S_2 \\ 0 \end{pmatrix}, \quad (\text{C.3})$$

where \mathbf{P} is the phase matrix in equation (3.13). Considering even a second scattering event in this case demonstrates that all of scattering matrix elements except the lower right most element, a_4 , affect radiative transfer results.

$$\begin{aligned}
\mathbf{I}_2 \propto \mathbf{P} \bullet \mathbf{I}_1 &= \begin{pmatrix} a_1 & b_1 C_1 & b_1 S_1 & 0 \\ b_1 C_2 & a_2 C_1 C_2 - a_3 S_1 S_2 & a_2 S_1 C_2 + a_3 C_1 S_2 & b_2 S_2 \\ -b_1 S_2 & -a_2 C_1 S_2 - a_3 S_1 C_2 & -a_2 S_1 S_2 + a_3 C_1 C_2 & b_2 C_2 \\ 0 & b_2 S_1 & -b_2 C_1 & a_4 \end{pmatrix} \bullet \begin{pmatrix} a_1 \\ b_1 C_2 \\ -b_1 S_2 \\ 0 \end{pmatrix} \\
&= \begin{pmatrix} a_1^2 + b_1^2 C_1 C_2 - b_1^2 S_1 S_2 \\ a_1 b_1 C_2 + b_1 C_2 (a_2 C_1 C_2 - a_3 S_1 S_2) - b_1 S_2 (a_2 C_2 S_1 + a_3 C_1 S_2) \\ -a_1 b_1 S_2 - b_1 S_2 (a_3 C_1 C_2 - a_2 S_1 S_2) + b_1 C_2 (-a_3 C_2 S_1 - a_2 C_1 S_2) \\ b_1 b_2 C_2 S_1 + b_1 b_2 C_1 S_2 \end{pmatrix}
\end{aligned} \tag{C.4}$$

LIST OF REFERENCES

- Allen, D. A., and T. L. Murdock 1971. Infrared photometry of Saturn, Titan, and the rings. *Icarus* **14**, 1-2.
- Bar-Nun, A., I. Kleinfeld, and E. Ganor 1988. Shape And Optical Properties Of Aerosols Formed By Photolysis Of Acetylene, Ethylene, And Hydrogen Cyanide. *J. Geophys. Res.* **93**, 8383-8387.
- Bohren, C. F., and D. R. Huffman 1983. *Absorption and Scattering of Light by Small Particles*. John Wiley & Sons, Inc., New York.
- Botet, R., P. Rannou, and M. Cabane 1997. Mean-field approximation of Mie scattering by fractal aggregates of identical spheres. *Appl. Opt.* **36**, 8791.
- Cabane, M., P. Rannou, E. Chassefière, and G. Israel 1993. Fractal aggregates in Titan's atmosphere. *Planet. Space Sci.* **41**, 257-267.
- Caldwell, J. J., C. C. Cunningham, D. Anthony, H. P. White, E. J. Groth, H. H., K. Noll, P. H. Smith, M. G. Tomasko, and H. A. Weaver 1992. Titan: Evidence for seasonal changes--A comparison of Hubble Space Telescope and Voyager images. *Icarus* **97**, 1-9.
- Chandrasekhar, S. 1960. *Radiative Transfer*. Dover Publications, Inc., New York.
- Clarke, D. W., and J. P. Ferris 1997. Titan Haze: Structure and Properties of Cyanoacetylene and Cyanoacetylene-Acetylene Photopolymers. *Icarus* **127**, 158-172.
- Combes, M., L. Vapillon, E. Gendron, A. Coustenis, O. Lai, R. Wittemberg, and R. Sirdey 1997. Spatially resolved images of Titan by means of adaptive optics. *Icarus* **129**, 482-497.
- Coulson, K. L. 1960. *Tables related to radiation emerging from a planetary atmosphere with Rayleigh scattering*. University of California Press, Berkeley.
- Courtin, R., R. Wagener, C. P. McKay, J. J. Caldwell, K.-H. Fricke, F. Raulin, and P. Bruston 1991. UV Spectroscopy of Titan's Atmosphere, Planetary Organic Chemistry and Prebiological Synthesis. II Interpretation of New IUE Observations in the 220-335 nm Range. *Icarus* **90**, 43-56.

- Coustenis, A., E. Lellouch, J.-P. Maillard, and C. P. McKay 1995. Titan's surface: composition and variability from the near-infrared albedo. *Icarus* **118**, 87-104.
- Danielson, R. E., J. J. Caldwell, and D. R. Larach 1973. An inversion in the atmosphere of Titan. *Icarus* **20**, 437.
- de Haan, J. F., P. B. Bosma, and J. W. Hovenier 1987. The adding method for multiple scattering calculations of polarized light. *Astron. Astrophys.* **183**, 371-391.
- de Rooij, W. A. 1985. *Reflection and Transmission of Polarized Light by Planetary Atmospheres*. Ph. D. Thesis, Free University, Amsterdam.
- Deirmendjian, D. 1969. *Electromagnetic Scattering on Spherical Polydispersions*. American Elsevier Publishing Company, Inc., New York.
- Draine, B. T. 1988. The discrete-dipole approximation and its application to interstellar graphite grains. *Astrophys. J.* **333**, 848-872.
- Draine, B. T., and P. J. Flatau 1994. Discrete -dipole approximation for scattering calculations. *J. Opt. Soc. Am. A* **11**, 1491-1499.
- Draine, B. T., and P. J. Flatau 1997. *User Guide for the Discrete Dipole Approximation Code DDSCAT (Version 5a)*, Princeton Observatory Preprint. Princeton Observatory.
- Evans, K. F., and G. L. Stephens 1991. A New Polarized Atmospheric Radiative Transfer Model. *J. Quant. Spectrosc. Radiat. Transfer* **46**, 413-423.
- Garcia, R. D. M., and C. E. Siewert 1986. A generalized spherical harmonics solution for radiative transfer models that include polarization effects. *J. Quant. Spectrosc. Radiat. Transfer* **36**, 401-423.
- Garcia, R. D. M., and C. E. Siewert 1989. The F_N method for radiative transfer models that include polarization effects. *J. Quant. Spectrosc. Radiat. Transfer* **41**, 117-145.
- Gel'fand, I. M., R. A. Minlos, and Z. Y. Shapiro 1963. *Representations of the rotation and Lorentz groups and their applications*. Pergamon Press, London.
- Gibbard, S. E., B. Macintosh, D. Gavel, C. E. Max, I. de Pater, A. M. Ghez, E. F. Young, and C. P. McKay 1999. Titan: high resolution speckle images from the Keck telescope. *Icarus* **139**, 189-201.
- Greenberg, J. M., and B. Å. S. Gustafson 1981. A comet fragment model for Zodiacal light particles. *Astron. Astrophys.* **93**, 35-42.
- Griffith, C. A. 1993. Evidence for surface heterogeneity of Titan. *Nature* **364**, 511-513.

- Griffith, C. A., T. Owne, G. A. Miller, and T. Geballe 1998. Transient clouds in Titan's lower atmosphere. *Nature* **395**, 575-578.
- Gustafson, B. Å. S. 1996. Microwave Analog To Light Scattering Measurements: A Modern Implementation of A Proven Method to Achieve Precise Control. *J. Quant. Spectrosc. Radiat. Transfer* **55**, 663-672.
- Gustafson, B. Å. S. 2000. Microwave analog to light scattering measurements. In *Light Scattering by Nonspherical Particles: Theory, Measurements, and Geophysical Applications* (M. I. Mishchenko, J. W. Hovenier and L. D. Travis, Ed.), pp. 367-390. Academic Press, New York.
- Gustafson, B. Å. S., and L. Kolokolova 1999. A systematic study of light scattering by aggregate particles using the microwave analog technique: Angular and wavelength dependence of intensity and polarization. *J. Geophys. Res.* **104**, 31711-31720.
- Gustafson, B. Å. S., L. Kolokolova, J. E. Thomas-Osip, K. W. T. Waldemarsson, J. Loesel, and Y. L. Xu 1998. Scattering By Complex Systems II: Results from Microwave Measurements. In *Formation and Evolution of Solids in Space* (J. M. Greenberg, Ed.), pp. 549. Kluwer Academic Publishers, Dordrecht.
- Haferman, J. L. 1995. *A Polarized Multi-Dimensional Discrete-Ordinates Radiative Transfer Model for Remote Sensing Applications*. Ph. D. Thesis, Mechanical Engineering, University of Iowa, Iowa City, Iowa.
- Hansen, J. E. 1971. *J. Atmos. Sci.* **28**, 120-125.
- Hansen, J. E., and L. D. Travis 1974. Light Scattering in Planetary Atmospheres. *Space Sci. Rev.* **16**, 527-610.
- Horak, H. G. 1950. Diffuse Reflection by Planetary Atmospheres. *Astrophys. J.* **112**, 445-463.
- Hovenier, J. W. 1969. Symmetry Relationships for Scattering of Polarized Light in a Slab of Randomly Oriented Particles. *J. Atmos. Sci.* **26**, 488-499.
- Hovenier, J. W. 1971. Multiple Scattering of Polarized Light in Planetary Atmospheres. *Astron. Astrophys.* **13**, 7-29.
- Hovenier, J. W., and C. V. M. van der Mee 1983. Fundamental relationships relevant to the transfer of polarized light in a scattering atmosphere. *Astron. Astrophys.* **128**, 1-16.
- Hutzel, W. T., C. P. McKay, O. B. Toon, and F. Hourdin 1996. Simulations of Titan's Brightness by a Two-Dimensional Haze Model. *Icarus* **119**, 112-129.

- Illuminating Engineering Society of North America 1996. *Nomenclature and Definitions for Illuminating Engineering*, . American National Standards Institute.
- Irvine, W. M. 1975. Multiple Scattering in Planetary Atmospheres. *Icarus* **25**, 175-204.
- Jackson, J. D. 1975. *Classical Electrodynamics*. John Wiley & Sons, New York, NY.
- Kattawar, G. W., and C. N. Adams 1971. Flux and polarization from a Rayleigh-scattering planetary atmosphere. *Astrophys. J.* **167**, 183-192.
- Kattawar, G. W., G. N. Plass, and C. N. Adams 1971. Flux and polarization calculations of the radiation reflected from the clouds of Venus. *Astrophys. J.* **170**, 371-386.
- Khare, B. N., and C. Sagan 1973. Red clouds in a reducing atmosphere. *Icarus* **20**, 311-21.
- Khare, B. N., C. Sagan, E. T. Arakawa, F. Suits, T. A. Callcott, and M. W. Williams 1984. Optical Constants of Organic Tholins Produced in Simulated Titanian Atmosphere: From Soft X-Ray to Microwave Frequencies. *Icarus* **60**, 127-137.
- Khare, B. N., W. R. Thompson, L. Cheng, C. Chyba, C. Sagan, E. T. Arakawa, C. Meisse, and P. S. Tuminello 1993. Production and Optical Constants of Ice Tholin from Charged Particle Irradiation of (1:6) C₂H₆/H₂O at 77 K. *Icarus* **103**, 290-300.
- Kolokolova, L., and B. Å. S. Gustafson 2000. Scattering by inhomogeneous particles: Microwave analog experiment comparison to effective medium theories. *in preparation*
- Kolokolova, L., and A. L. Zaitsev 1999. Ground-based Radar Experiments for the Study of Radiation Scattering by Atmosphereless Celestial Bodies. *Astronomical and Astrophysical Transactions* **13**, 245-53.
- Kuik, F., J. F. de Haan, and J. W. Hovenier 1992. Benchmark Results for Single Scattering by Spheroids. *J. Quant. Spectrosc. Radiat. Transfer* **47**, 477-489.
- Kuiper, G. P. 1944. Titan: A satellite with an atmosphere. *Astrophys. J.* **100**, 378-83.
- Kuscer, I., and M. Ribaric 1959. Matrix formalism in the theory of diffusion of light. *Optica Acta* **6**, 42-51.
- Lemmon, M. T. 1994. *Properties of Titan's Haze and Surface*. Ph. D. Thesis, Department of Planetary Sciences, University of Arizona, Tucson.
- Lemmon, M. T., E. Karkoschka, and M. G. Tomasko 1993. Titan's Rotation: Surface Feature Observed. *Icarus* **103**, 329-332.
- Lemmon, M. T., E. Karkoschka, and M. G. Tomasko 1995. Titan's Rotational Light Curve. *Icarus* **113**, 27-38.

- Lenoble, J. 1985. *Radiative Transfer in Scattering and Absorbing Atmospheres: Standard Computational Procedures*. A. Deepak Publishing, Hampton, VA.
- Lindal, G. F., G. E. Wood, H. B. Hotz, D. N. Sweetnam, V. R. Eshleman, and G. L. Tyler 1983. The Atmosphere of Titan: An Analysis of the Voyager 1 Radio Occultation Measurements. *Icarus* **53**, 348-363.
- Liou, K. N. 1980. *An Introduction to Atmospheric Radiation*. Academic Press, New York.
- Liou, K. N. 1992. *Radiation and Cloud Processes in the Atmosphere: theory, observation and modeling*. Oxford University Press, New York, NY.
- Lockwood, G. W., B. L. Lutz, D. T. Thompson, and E. S. Bus 1986. The Albedo of Titan. *Astrophys. J.* **303**, 511-520.
- McCord, T. B., T. V. Johnson, and J. H. Elias 1971. Saturn and its satellites: Narrow-band spectrophotometry (0.3-1.1 μ). *Astrophys. J.* **165**, 413-24.
- McKay, C. P., J. B. Pollack, and R. Courtin 1989. The Thermal Structure of Titan's Atmosphere. *Icarus* **80**, 23-53.
- McKay, C. P., J. B. Pollack, and R. Courtin 1991. The Greenhouse and Antighreenhouse Effects of Titan. *Science* **253**, 1118-1121.
- Mishchenko, M. I. 1993. On the nature of the polarization opposition effect exhibited by Saturn's rings. *Astrophys. J.* **411**, 351-361.
- Mishchenko, M. I., J. W. Hovenier, and L. D. Travis 2000. *Light Scattering by Nonspherical Particles: Theory, Measurements, and Applications*.
- Neff, J. S., D. C. Humm, J. T. Bergstralh, A. L. Cochran, W. D. Cochran, E. S. Barker, and R. G. Tull 1984. Absolute Spectrophotometry of Titan, Uranus, and Neptune: 3500-10,500 Å. *Icarus* **60**, 221-235.
- Noland, M., J. Veverka, D. Morrison, D. P. Cruikshank, A. R. Lazarewicz, N. D. Morrison, J. L. Elliot, J. Goguen, and J. A. Burns 1974. Six color photometry of Iapetus, Titan, Rhea, Dione, and Tethys. *Icarus* **23**, 334-54.
- Pollack, J. B. 1973. Greenhouse models of the atmosphere of Titan. *Icarus* **19**, 43-58.
- Purcell, E. M., and C. R. Pennypacker 1973. Scattering and Absorption of Light by Nonspherical Dielectric Grains. *Astrophys. J.* **186**, 705-714.
- Rages, K., J. B. Pollack, and P. H. Smith 1983. Size Estimates of Titan's Aerosols Based on Voyager High-Phase-Angle Images. *J. Geophys. Res.* **88**, 8721-8728.

- Rannou, P., M. Cabane, R. Botet, and E. Chassefière 1997. A new interpretation of scattered light measurements at Titan's limb. *J. Geophys. Res.* **102**, 10997-11013.
- Rannou, P., M. Cabane, E. Chassefière, R. Botet, C. P. McKay, and R. Courtin 1995. Titan's Geometric Albedo: Role of the Fractal Structure of the Aerosols. *Icarus* **118**, 355-372.
- Reitz, J. R., F. J. Milford, and R. W. Christy 1980. *Foundations of Electromagnetic Theory*. Addison-Wesley Publishing Company, Reading, MA.
- Sagan, C. 1973. The greenhouse of Titan. *Icarus* **18**, 649-56.
- Scattergood, T. W., E. Y. Lau, and B. M. Stone 1992. Titan's Aerosols I. Laboratory Investigations of Shapes, Size Distributions, and Aggregation of Particles Produced by UV Photolysis of Model Titan Atmospheres. *Icarus* **99**, 98-105.
- Schoenberg, E. 1929. *Theoretische Photometrie*. Julius Springer, Berlin.
- Siewert, C. E., and P. Benoist 1979. The FN method in Neutron-Transport theory. Part I: Theory and applications. *Nucl. Sci. Engng* **69**, 156-160.
- Smith, P. H., M. T. Lemmon, L. V. Lorenz, L. A. Sromovsky, J. J. Caldwell, and M. D. Allison 1996. Titan's Surface, Revealed by HST Imaging. *Icarus* **119**, 336-349.
- Smith, R. J., and R. D. Wolstencroft 1983. High Precision Spectropolarimetry of Stars and Planets - II. Spectropolarimetry of Jupiter and Saturn. *Monthly Notices of the Royal Astronomical Society* **205**, 39-55.
- Sobolev, V. V. 1975. *Light scattering in planetary atmospheres*. Pergamon Press, Oxford, New York.
- Sromovsky, L. A., V. E. Suomi, J. B. Pollack, R. J. Krauss, S. S. Limaye, T. Owen, H. E. Revercomb, and C. Sagan 1981. Implications of Titan's north-south brightness asymmetry. *Nature* **292**,
- Stokes, G. G. 1862. On the intensity of the light reflected from or transmitted through a pile of plates. *Philos. Trans. R. Soc. London Ser. A* **11**, 545-556.
- Tomasko, M. G. 1976. Photometry and Polarimetry of Jupiter. In *Jupiter, Studies of the interior, atmosphere, magnetosphere and satellites* (T. Gehrels, Ed.), pp. 486-515. University of Arizona Press, Tucson, AZ.
- Tomasko, M. G., L. R. Doose, P. H. Smith, R. A. West, L. A. Soderblom, M. Combes, B. Bezard, A. Coustenis, C. de Bergh, E. Lellouch, J. Rosenqvist, O. Saint-Pe, B. Schmitt, H. U. Keller, N. Thomas, and F. Gliem 1997. The Descent Imager/Spectral Radiometer (DISR) Aboard Huygens. In *Huygens. Science, Payload, and Mission* (J.-P. Lebreton, Ed.), pp. 109-138. ESA, The Netherlands.

- Tomasko, M. G., and P. H. Smith 1982. Photometry and Polarimetry of Titan: Pioneer 11 Observations and Their Implications for Aerosol Properties. *Icarus* **51**, 65-95.
- Toon, O. B., C. P. McKay, C. A. Griffith, and R. P. Turco 1992. A Physical Model of Titan's Aerosols. *Icarus* **95**, 24-53.
- Trafton, L. 1972a. The bulk composition of Titan's atmosphere. *Astrophys. J.* **175**, 295-306.
- Trafton, L. 1972b. On the possible detection of H_2 in Titan's atmosphere. *Astrophys. J.* **175**, 285-93.
- van de Hulst, H. C. 1957. *Light Scattering by Small Particles*. Dover Publications, Inc., New York.
- van de Hulst, H. C. 1980. *Multiple Light Scattering Tables, Formulas, and Applications*. Academic Press, Inc, New York, NY.
- Waldemarsson, K. W. T., and B. Å. S. Gustafson 2000. *Light Scattering by Thin Flakes*. Fifth International Conference on Light Scattering by Nonspherical Particles, Halifax, Canada, pp 34-37.
- Wauben, W. M. F., J. F. de Haan, and J. W. Hovenier 1994. A method for computing visible and infrared polarized monochromatic radiation in planetary atmospheres. *Astron. Astrophys.* **282**, 277-290.
- Wauben, W. M. F., and J. W. Hovenier 1992. Polarized Radiation of an Atmosphere Containing Randomly-Oriented Spheroids. *J. Quant. Spectrosc. Radiat. Transfer* **47**, 491-504.
- West, R. A., A. L. Lane, H. Hart, K. E. Simmons, C. W. Hord, D. L. Coffeen, L. W. Esposito, M. Sato, and R. B. Pomphrey 1983. Voyager 2 Photopolarimeter Observations of Titan. *J. Geophys. Res.* **88**,
- West, R. A., and P. H. Smith 1991. Evidence for Aggregate Particles in the Atmospheres of Titan and Jupiter. *Icarus* **90**, 330-333.
- Xu, Y. L. 1995. Electromagnetic scattering by an aggregate of spheres. *Appl. Opt.* **34**, 4573-4588.
- Xu, Y. L. 1997. Electromagnetic scattering by an aggregate of spheres: far field. *Appl. Opt.* **36**, 9496-9508.
- Xu, Y. L., and B. Å. S. Gustafson 1999. Comparison between multisphere light-scattering calculations: (I) Rigorous solution and (II) DDA. *Astrophys. J.* **513**, 894-909.

- Xu, Y. L., and R. T. Wang 1998. Electromagnetic scattering by an aggregate of spheres: Theoretical and experimental study of the amplitude scattering matrix. *Phys. Rev. E* **58**, 3931-3948.
- Zakharova, N. T., and M. I. Mishchenko 2001. Scattering by randomly oriented thin ice disks with moderate equivalent-sphere size parameters. *J. Quant. Spectrosc. Radiat. Transfer* **in press**,
- Zellner, B. 1973. The Polarization of Titan. *Icarus* **18**, 661-664.
- Zerull, R. H., B. Å. S. Gustafson, K. Schulz, and E. Thiele-Corbach 1993. Scattering by aggregates with and without an absorbing mantle: microwave analog experiments. *Appl. Opt.* **32**, 4088-4100.

BIOGRAPHICAL SKETCH

Joanna Elizabeth Thomas-Osip was born May 27, 1971, in Seattle, Washington. Her father, John R. Thomas, is a retired electrical engineer. Her mother, Maralyn Thomas-Schier, teaches early childhood education at Seattle Central Community College. Joanna graduated from Franklin High School, also in Seattle, in 1989 and went on to attend Whitman College in Walla Walla, Washington.

She received a Bachelor of Arts degree in physics and astronomy with honors in major field of study from Whitman College in May of 1993 completing an honor's thesis involving photoelectric photometry of open star clusters. She also completed several research projects as a part of her program of study at Whitman. As part of a course in planetary astrophysics, she did a research project on the organic chemistry of the atmosphere of Jupiter. This was further expanded to be an independent study project dealing more specifically with chromophores in the Jovian atmosphere. She also researched the formation of molecules in the interstellar medium.


During the summer of 1992 Joanna worked with K. S. Balasubramaniam and Stephen L. Kiel at the National Solar Observatory as a research assistant in their REU program. The objective of their project was to model the solar photosphere and chromosphere as well as work towards the prediction of solar flares. Joanna utilized data taken with the Vacuum Tower Telescope at Sacramento Peak in New Mexico to

determine velocity fields during flares. This summer research opportunity confirmed her desire to pursue a career in astronomy.

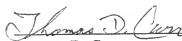
In the fall of 1993, she enrolled at the University of Florida to pursue a doctorate in astronomy. Here she served as a teaching assistant in her first year. In her second year she received a Florida Space Grant Consortium fellowship and the next three years she was supported by a NASA graduate student researchers fellowship. During this time she began her studies of light scattering, radiative transfer, and Titan's atmosphere with Dr. Bo Å. S. Gustafson.

In 1995, Joanna married fellow astronomer and University of Florida Astronomy alumni Dr. David J. Osip. In 1998 they moved to Boston so David could accept a research scientist position in the Department of Earth, Atmospheric, and Planetary Science at the Massachusetts Institute of Technology. After graduation in May 2001, Joanna will also join the Massachusetts Institute of Technology. She will work in a post-doctoral research position with Dr. James L. Elliot on projects including planetary occultation observation and data analysis.


I certify that I have read this study and that in my opinion it conforms to acceptable standards of scholarly presentation and is fully adequate, in scope and quality, as a dissertation for the degree of Doctor of Philosophy.


Bo Å. S. Gustafson, Chairman
Professor of Astronomy

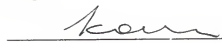
I certify that I have read this study and that in my opinion it conforms to acceptable standards of scholarly presentation and is fully adequate, in scope and quality, as a dissertation for the degree of Doctor of Philosophy.


Thomas D. Carr
Professor Emeritus of Astronomy


I certify that I have read this study and that in my opinion it conforms to acceptable standards of scholarly presentation and is fully adequate, in scope and quality, as a dissertation for the degree of Doctor of Philosophy.


Stanley F. Dermott
Professor of Astronomy

I certify that I have read this study and that in my opinion it conforms to acceptable standards of scholarly presentation and is fully adequate, in scope and quality, as a dissertation for the degree of Doctor of Philosophy.


Ludmilla Kolokolova
Assistant Scientist in Astronomy

I certify that I have read this study and that in my opinion it conforms to acceptable standards of scholarly presentation and is fully adequate, in scope and quality, as a dissertation for the degree of Doctor of Philosophy.


Martin T. Vala, Jr.
Professor of Chemistry

I certify that I have read this study and that in my opinion it conforms to acceptable standards of scholarly presentation and is fully adequate, in scope and quality, as a dissertation for the degree of Doctor of Philosophy.



Yu-Lin Xu

Associate Scientist in Astronomy

This dissertation was submitted to the Graduate Faculty of the Department of Astronomy in the College of Liberal Arts and Sciences and to the Graduate School and was accepted as partial fulfillment of the requirements for the degree of Doctor of Philosophy.

May 2001

Dean, Graduate School

LD
1780
20 01

.T459

